Unfolding the top

Measuring the quantum interference between singly and doubly resonant top-quark production at $\sqrt{s} = 13\,\mathrm{TeV}$ with the ATLAS detector

DISSERTATION

zur Erlangung des akademischen Grades
Doctor rerum naturalium (Dr. rer. nat.)
im Fach Physik, Spezialisierung Experimentalphysik

eingereicht an der
Mathematisch-Naturwissenschaftlichen Fakultät
Humboldt-Universität zu Berlin

von
MSc. Eleonora Loiacono

Präsidentin der Humboldt-Universität zu Berlin
Prof. Dr. Julia von Blumenthal

Dekanin der Mathematisch-Naturwissenschaftlichen
Prof. Dr. Caren Tischendorf

Gutachter/innen:
1. Dr. Priscilla Pani
2. Prof. Dr. Thomas Lohse
3. Prof. Dr. Gianluca Cavoto

Tag der mündlichen Prüfung: 17/10/2024

To Nicola, Elvira and Diana.

"I hope I can inspire other young women into the field.
It's a field that has so many pleasures,
and if you are passionate about the science,
there's so much that can be done."

A. Ghez

Erklärung

I declare that I have completed the thesis independently using only the aids and tools specified. I have not applied for a doctor's degree in the doctoral subject elsewhere and do not hold a corresponding doctor's degree. I have taken due note of the Faculty of Mathematics and Natural Sciences PhD Regulations, published in the Official Gazette of Humboldt-Universität zu Berlin no. 42/2018 on 11/07/2018.

Berlin, 11 July 2024

Abstract

The top-quark is the heaviest known particle of the Standard Model (SM) and it is extensively studied at the Large Hadron Collider (LHC) due to its importance in probing fundamental parameters of the Standard Model (SM) and its role as a background in various searches for physics Beyond the Standard Model (BSM). The top-quark can be produced in pairs ($t\bar{t}$), which is the most abundant production mode at the LHC, or singularly in association with other particles. In particular, the single-top is important because less studied and more challenging to treat theoretically. The analysis presented in this thesis fills this gap, by measuring the cross-section of $WbWb$, which is a final state of both $t\bar{t}$ and single-top processes. While the $t\bar{t}$ and tW are commonly treated as independent processes, the presented thesis addresses the interference effects between them, which become particularly relevant at higher orders in perturbative QCD, providing a more consistent theoretical treatment. The analysis uses semileptonic $WbWb$ decays and thereby is complementary to the result in the dilepton channel. To improve the modelling in a broad phase-space, two phase spaces are defined: one encompassing the majority of events to have the largest accessible cross-section, and another targeting the tails of distributions to explore phase spaces relevant to BSM searches. The differential cross-section measurements are valuable for assessing and tuning Monte Carlo generators, determining SM parameters, and constraining uncertainties in BSM searches. Using the full dataset from the ATLAS detector at the LHC at $\sqrt{s} = 13\,\text{TeV}$ with $\mathcal{L} = 140\,\text{fb}^{-1}$ collected in Run-2, this study contributes to a more comprehensive understanding of top-quark pair production and its implications for future physics searches. The result of this thesis can be further used by the scientific community without the limitation of needing a detector simulation to tune and validate the theoretical predictions.

Zusammenfassung

Das Top-Quark ist das schwerste bekannte Teilchen des Standardmodells (SM) und wird am Large Hadron Collider (LHC) aufgrund seiner Bedeutung für die Untersuchung fundamentaler Parameter des Standardmodells (SM) und seiner Rolle als Hintergrund für die Suche nach Physik jenseits des Standardmodells (BSM) eingehend untersucht. Das Top-Quark kann in Paaren ($t\bar{t}$) produziert werden, was die häufigste Produktionsart am LHC ist, oder einzeln in Verbindung mit anderen Teilchen. Insbesondere die Einzelproduktion ist wichtig, da sie weniger untersucht und theoretisch schwieriger zu behandeln ist. Die in dieser Arbeit vorgestellte Analyse füllt diese Lücke, indem sie den Querschnitt von $WbWb$ misst, der ein Endzustand sowohl von $t\bar{t}$ als auch von Single-Top-Prozessen ist. Während $t\bar{t}$ und tW üblicherweise als unabhängige Prozesse behandelt werden, befasst sich die vorliegende Arbeit mit den Interferenzeffekten zwischen ihnen, die bei höheren Ordnungen in der störungsbehafteten QCD besonders relevant werden und eine konsistentere theoretische Behandlung ermöglichen. Die Analyse verwendet semileptonische $WbWb$-Zerfälle und ist damit komplementär zu den Ergebnissen im Dileptonkanal. Um die Modellierung in einem breiten Phasenraum zu verbessern, werden zwei Phasenräume definiert: einer umfasst die Mehrheit der Ereignisse, um den größten zugänglichen Wirkungsquerschnitt zu erhalten, und ein anderer zielt auf die Schwänze der Verteilungen ab, um die für die BSM-Suche relevanten Phasenräume zu erforschen. Die Messungen des differentiellen Wirkungsquerschnitts sind wertvoll für die Bewertung und Abstimmung von Monte-Carlo-Generatoren, die Bestimmung von SM-Parametern und die Eingrenzung von Unsicherheiten bei der BSM-Suche. Unter Verwendung des gesamten Datensatzes des ATLAS-Detektors am LHC bei $\sqrt{s} = 13\,\mathrm{TeV}$ mit $\mathcal{L} = 140\,\mathrm{fb}^{-1}$, der in Run-2 gesammelt wurde, trägt diese Studie zu einem umfassenderen Verständnis der Top-Quark-Paarproduktion und deren Auswirkungen auf die zukünftige Physiksuche bei. Die Ergebnisse dieser Arbeit können von der wissenschaftlichen Gemeinschaft weiter genutzt werden, ohne dass eine Detektorsimulation zur Abstimmung und Validierung der theoretischen Vorhersagen erforderlich ist.

Contents

1
Introduction

Particle physicists aim to comprehend the basic building blocks of matter and the fundamental forces that govern their interactions. Central to this endeavour is the Standard Model (SM), a well-established theory which describes the electromagnetic, weak and strong interactions [1, 2]. These interactions are studied at the world's largest and most powerful particle accelerator: the Large Hadron Collider (LHC) [3] at the European Organization for Nuclear Research (CERN).

The heaviest of all known elementary particles of the Standard Model is the top-quark (t), with a mass of 172.69 GeV [4]. Since its discovery at Fermilab, the top quark has been the subject of ongoing research and analysis.

At the LHC, almost 90% of top quarks are produced in pairs ($t\bar{t}$) via gluon-gluon fusion ($gg \rightarrow t\bar{t}$). The other relevant production mechanism is through quark-antiquark annihilation ($q\bar{q} \rightarrow t\bar{t}$). The total cross-section for the top-pair production is $\sigma_{t\bar{t}}\,(m_t = 172.5\text{GeV}, \sqrt{s} = 13\,\text{TeV}) = 831.8^{+19.8+35.1}_{-29.2-35.1}\,\text{pb}$ [4].

In addition to pair production, single top quarks can also be produced in association with other particles. At the lowest order in α_S, single top-quark production occurs via quark-antiquark annihilation in the s-channel ($q\bar{q}' \rightarrow t\bar{b}$), quark-b-quark interaction in the t-channel ($qb \rightarrow tq'$), or gluon-b-quark interaction ($gb \rightarrow tW^-$). The latter is referred to as W-associated top-quark production (tW) [5].

At the next higher order in α_S [6], top-quark production in association with a W-boson and a b-quark (tWb) has to be considered. Since the top quark decays to a W-boson and a b-quark in over 99% of cases, the top-quark production in association with a W-boson and a b-quark tWb and top pair production $t\bar{t}$ have the same final state which is ($WbWb$) [4]. Therefore, these production modes interfere, and this interference has to be accounted for when calculating the cross-sections of top-quark processes.

The theoretical treatment of the interference between these two processes is quite complicated. The correct description of the interference involves the full calculation of the all $WbWb$ contributions. However, the available parton showers do not accurately reflect the time evolution at the matrix element level. This includes the fact that the top and W bosons have a width, and the underlying event (UE) and non-resonant b-quarks can start the parton shower before the W/top decays. Consequently, it is unclear what belongs together in the parton shower. For the description of $WbWb$ final state, significant theoretical development is required to control the parton shower. It may be less effective for phase spaces where the description of tW is adequate (in the bulk of tW) but beneficial in search regions where the interference between $t\bar{t}$ and tW processes is poorly described, making parton shower issues less significant. Several definitions of the tW channel have been given in the literature, each with the aim of recovering a well-behaved expansion in α_S. In fact, the interference problem affects any computation that considers contributions beyond the leading order. Consequently, to address these interference-related issues, methods such as Diagram Removal (DR) [7] and Diagram Subtraction (DS) [7] are employed.

As more data is collected at the LHC and top processes are measured with higher accuracy and in extreme phase spaces, it became apparent that these schemes do not adequately describe the data as they factorize the interference process without fully accounting for it. The complexity of modelling the interference process poses a challenge to theorists and requires the inclusion of higher-order corrections. For this reason a comprehensive measurement of this process is essential to compare with theoretical predictions and improve their accuracy. In addition, the interference between top-quark pair production and single-top production in higher-order perturbative QCD introduces significant uncertainty in the search for new physics phenomena at high masses [8, 9].

The interference between $t\bar{t}$ and tW processes has been studied in the past by the ATLAS [10] and CMS [11] experiments at the LHC in the dilepton channel, and discrepancies between Monte Carlo modelling for the interference and data have been observed.

The motivation for this thesis is to provide a detailed measurement of the process in phase spaces sensitive to the tW and $t\bar{t}$ interference, offering insights into top-quark physics and contributing to the ongoing efforts to refine theoretical predictions and reduce uncertainties in high-mass searches for new physics.

This thesis presents the first measurement of the differential production cross-sections of the process $pp \to WbWb$ in the $l+$jets (or *single lepton*) decay channel, using data collected with the ATLAS detector [12] at the LHC during LHC Run-2 (between 2015 and 2018) at a center-of-mass energy of $\sqrt{s} = 13\,\text{TeV}$. The decay channel refers to the decay of the two W bosons, where one W boson decays leptonically into a charged lepton (muon or electron, $\mu^{\pm}$ or $e^{\pm}$) and a neutrino ν, while the other decays hadronically and can be identified using jets. The semileptonic decay channel provides the opportunity to measure the W-boson kinematics directly, since the hadronically decaying W-boson can be fully reconstructed. In addition, the cross-section in the l+*jets* channel is higher with respect to the dilepton channel. On the other hand the l+jets channel presents a challenge due to the presence of missing transverse energy in the final state.

Two different phase spaces are defined in this analysis. The first one, similar to the phase spaces often used in the Standard Model measurements, is denoted as the measurement-like phase space. This phase space allows to probe the phase space where the cross section is the highest. The second phase space is based on the phase space targeted by Beyond Standard Model (BSM) physics, defined as the search-like phase space. This phase space represents a novelty as it is the first time in ATLAS that a measurement has been designed specifically for a search.

Variables particularly sensitive to the interference are identified, and the measurement of the differential cross-section is performed using an unfolding procedure to correct for the limited geometric acceptance and the limited efficiency of the detector. The unfolded result is then compared to the different theoretical predictions for the interference. Unfolded data can be further used by the scientific community without the limitation of needing a detector simulation to tune and validate the theoretical predictions.

The thesis is organised as follows. Chapter 2 gives a brief summary of the Standard Model. Chapter 3 describes the Large Hadron Collider and the ATLAS experiment. Chapter 4 details how the proton-proton collisions are simulated in this thesis. Chapter 5 describes how the identification of physics objects is performed. The differential cross-section measurement is presented in detail in Chapters 6, 7 and 8. Finally, the results are presented in Chapter 9.

2
Theoretical Framework

2.1 The Standard Model of Particle Physics

The Standard Model (SM) of particle physics was proposed by S. Glashow, S. Weinberg and A. Salam in the 1960s and 1970s and represents the current understanding of the building blocks of matter [1, 2].

It describes three of the four fundamental interactions: the strong, weak and electromagnetic forces. At present, the SM does not describe the gravitational force.

2.1.1 Theoretical formulation of the SM

The theoretical formulation of the Standard Model is based on the Lagrangian formalism and the notion of symmetries [13], and it is based on four-dimensional quantum fields [1]. The SM is described by the Lagrangian density

$$\mathcal{L}_{SM} = \mathcal{L}_{QCD} + \mathcal{L}_{EWK} \tag{2.1}$$

which is invariant under the local gauge symmetry

$$SU(3)_C \otimes SU(2)_L \otimes U(1)_Y \tag{2.2}$$

where $SU(3)_C$ is the colour symmetry, $SU(2)_L$ is the weak isospin symmetry and $U(1)_Y$ is the hypercharge symmetry. Together, $SU(2)_L$ and $U(1)_Y$ describe the electroweak interactions, while $SU(3)_C$ characterises the strong interactions.

[1] three spatial dimensions and one time dimension.

Strong Interactions

The strong interaction is described by Quantum Chromodynamics (QCD). QCD involves quarks, which are spin 1/2 fermions, and gluons, which are spin 1 bosons (*vector bosons*). The conserved quantity in QCD is colour. There are three colours: red, blue and green, and the three corresponding anti-colours. Particles combine in such a way that they are colourless, this can happen by summing up all three colours or by combining colour/anti-colour, this phenomenon is known as *colour confinement*. The strong interactions are invariant under the symmetry group $SU(3)$ as

$$q(x) \to U(x)q(x) = e^{-ig_S\alpha_a(x)T_a}q(x) \tag{2.3}$$

where $g_S = 4\pi\alpha_S$ is the coupling constant of strong interactions coupling while α_a are an arbitrary functions. T_a represents the 8 generators of $SU(3)$ [2], these generators require the introduction of 8 fields, the gluons, denoted by G^a. G^a transforms as

$$G^a_\mu \to G^a_\mu - \frac{1}{g_S}\partial_\mu\alpha_a - f_{abc}\alpha_b G^c_\mu \tag{2.4}$$

The QCD lagrangian density can be written as

$$\mathcal{L}_{QCD} = -\frac{1}{4}\sum_a F^a_{\mu\nu}F^{\mu\nu,a} + \bar{q}(i\gamma^\mu D_\mu - m)q \tag{2.5}$$

with

$$D_\mu = \partial_\mu + igT_aG^a_\mu \tag{2.6}$$

$$F^a_{\mu\nu} = \partial_\mu G^a_\nu - \partial_\nu G^a_\mu + g_S f_{abc}G^b_\mu G^c_\nu \tag{2.7}$$

QCD is a non-abelian theory, meaning the gluon can self-interact and the result of this is the third term of the equation. A fundamental feature of QCD is *asymptotic freedom*: quarks interact weakly at high energies, hence allowing for perturbative calculations, but strongly at low energies, preventing the unbinding of baryons and mesons.

Colour confinement and asymptotic freedom are related to the running of the strong coupling constant α_S. α_S is not constant, but is expressed as a function of the energy scale of the interaction, Q^2 [6], as shown by Figure 2.1.

The evolution of α_S as a function of Q^2 is expressed as

$$\alpha_S(Q^2) = \frac{\alpha_S(\Lambda^2_{QCD})}{1 + B\alpha_S(\Lambda^2_{QCD})\ln\left(\dfrac{Q^2}{\Lambda_{QCD}}\right)} \tag{2.8}$$

[2] T_a is a 3×3 matrix such that $[T_a, T_b] = if_{abc}T_c$.

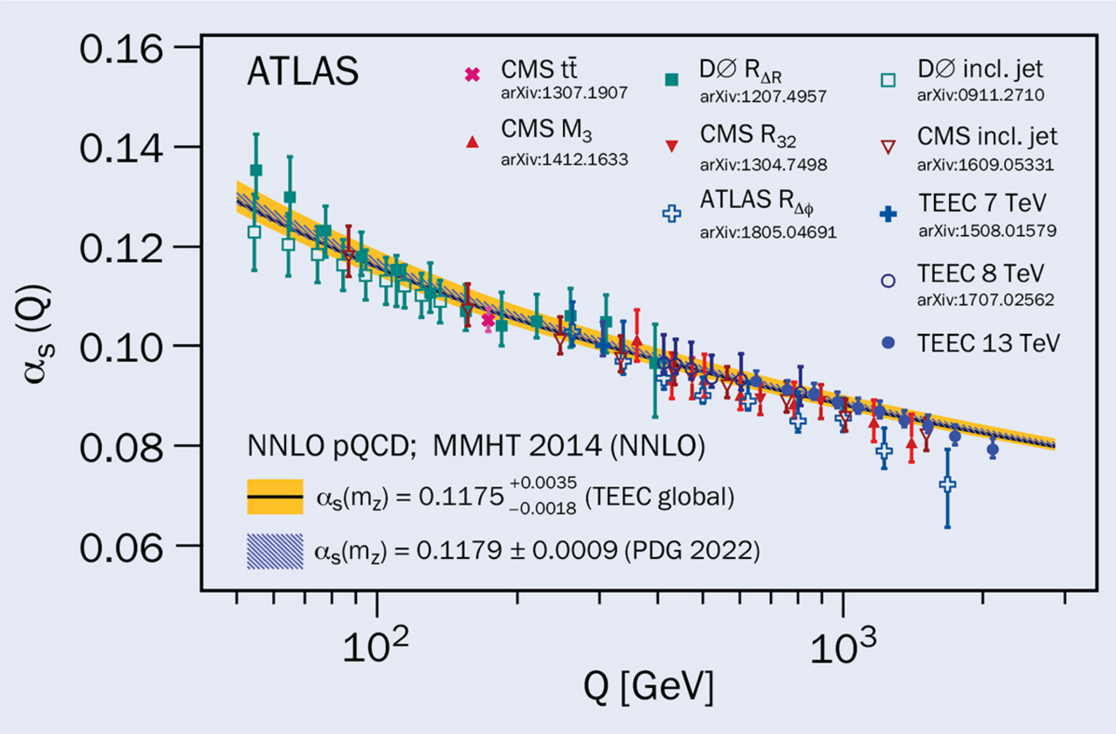

Figure 2.1: Comparison of the values of $\alpha_S(Q)$, determined from fits, with the QCD prediction using the world average (blue band) as input and the value obtained from the global fit (yellow band) [14].

with

$$B = \frac{12N_C - 2N_f}{12\pi} \tag{2.9}$$

where $N_C = 3$ is the number of possible colours and $N_f \leq 6$ is the number of active flavour quarks. Λ_{QCD} is an infrared cut-off scale beyond which the perturbative approximation doesn't hold, its value is ≈ 200MeV.

In the framework of perturbative QCD (pQCD), predictions for observables are expressed in terms of the renormalized coupling $\alpha_S(\mu_R^2)$, a function of an (unphysical) re-normalization scale μ_R. When taking μ_R close to the scale of the momentum transfer Q in a given process, then $\alpha_S(\mu_R^2 \simeq Q)$ is indicative of the effective strength of the strong interaction in that process [4].

Electroweak Interactions

Electroweak theory aims to unify the weak and electromagnetic interactions. It is invariant under the transformation of the symmetry group

$$SU(2)_L \otimes U(1)_Y \tag{2.10}$$

Where L stands for left-handed particles and Y is the hypercharge. The symmetry group $SU(2)_L \otimes U(1)_Y$ is described by four generators corresponding to four gauge bosons.

Fermions are coupled according to their chirality state

$$\text{Left-handed fermions: } \psi_L = P_L\psi = \frac{1}{2}(1-\gamma^5)\psi \tag{2.11}$$

$$\text{Right-handed fermions: } \psi_R = P_R\psi = \frac{1}{2}(1+\gamma^5)\psi \tag{2.12}$$

$P_{L,R}$ are the left/right handed projection operators, while $\gamma^5 = i\gamma^0\gamma^1\gamma^2\gamma^3$. The generators consist in a triplet for $SU(2)_L$, W_i^μ, $(i = 1, 2, 3)$, which couples with left-handed fermion fields, and a singlet for $U(1)_Y$, B^μ, which couples with fermions of both chiralities. Left-handed fermions are paired in doublets with isospin $I = 1/2$, while right-handed fermions are isospin singlets with $I = 0$. The fermions are further divided into quarks and leptons.

There are three families of quarks

$$\begin{pmatrix} u \\ d \end{pmatrix}_L, \begin{pmatrix} c \\ s \end{pmatrix}_L, \begin{pmatrix} t \\ b \end{pmatrix}_L, \ (u)_R, (d)_R, (c)_R, (s)_R, (t)_R, (b)_R$$

and three families of leptons

$$\begin{pmatrix} \nu_e \\ e \end{pmatrix}_L, \begin{pmatrix} \nu_\mu \\ \mu \end{pmatrix}_L, \begin{pmatrix} \nu_\tau \\ \tau \end{pmatrix}_L, \ (e)_R, (\mu)_R, (\tau)_R, (\nu_e)_R, (\nu_\mu)_R, (\nu_\tau)_R$$

The weak hypercharge and the third component of the isospin are related to the electromagnetic charge Q as follows

$$Q = I_3 + \frac{Y}{2} \tag{2.13}$$

The hypercharge involves right- and left-handed particles, therefore the lagrangian density is invariant under $U(1)$. In this case the field transforms as

$$\psi_{L,R} \to U(1)\psi_{L,R} = e^{i\alpha(x)Y/2}\psi_{L,R} \tag{2.14}$$

On the other hand, isospin symmetry only applies to left-handed particles, therefore the lagrangian is invariant under $SU(2)$ transformations. The field transforms as

$$\psi_L \to SU(2)\psi_L = e^{i\beta_a(x)\tau^a/2}\psi_L \tag{2.15}$$

with $\tau^a/2$ being the $SU(2)$ generators, with $a = 1, 2, 3$ [3].

[3] The $SU(2)$ generators, τ^a, are the Pauli matrices.

Four physical fields corresponding to the four vector bosons can be obtained with the following linear combinations

$$A^\mu = \sin(\theta_W) W_3^\mu + \cos(\theta_W) B^\mu \tag{2.16}$$

$$Z^\mu = \cos(\theta_W) W_3^\mu - \sin(\theta_W) B^\mu \tag{2.17}$$

$$W_{12}^\pm = \frac{1}{\sqrt{2}}(W_\mu^1 \mp i W_\mu^2) \tag{2.18}$$

where A^μ corresponds to the photon, Z^μ to the neutral Z boson and $W_{12}^\pm$ to the charged $W^\pm$ bosons. The angle θ_W represents the weak mixing angle.

For a fermionic field ψ, the lagrangian density is constructed as

$$\mathcal{L}_{\mathcal{EWK}} = -\frac{1}{4} W_{\mu\nu}^a W^{a,\mu\nu} - \frac{1}{4} B_{\mu\nu} B^{\mu\nu} + i\bar{\psi}\gamma^\mu D_\mu \psi \tag{2.19}$$

where the index a runs over the three gauge bosons. The field strength tensor terms, which define the the field dynamics, are defined as

$$B_{\mu\nu} = \partial_\mu B_\nu - \partial_\nu B_\mu \tag{2.20}$$

$$W_{\mu\nu}^a = \partial_\mu W_\nu^a - \partial_\nu W_\mu^a - i g_W \epsilon^{abc} \{W_\nu^b, W_\mu^c\} \tag{2.21}$$

and D_μ is the covariant derivative

$$D_\mu = \partial_\mu + i g W_\mu^a I_a + i \frac{g'}{2} B_\mu Y \tag{2.22}$$

with g, g' being the coupling constants of $SU(2)$ and $U(1)$ respectively. The couplings are such that the mixing angle, θ_W, can be written as a function of the two

$$\sin(\theta_W) = \frac{g'}{\sqrt{g^2 + g'^2}} \tag{2.23}$$

$$\cos(\theta_W) = \frac{g}{\sqrt{g^2 + g'^2}} \tag{2.24}$$

It has to be noted that the gauge symmetry of the $SU(2)_L \otimes U(1)_Y$ group does not allow mass terms for the $W^\pm$ and Z bosons. However, these bosons are known to be massive, suggesting that the current theory of electroweak interactions is incomplete. The solution to this problem lies in the phenomenon of spontaneous breaking of electroweak symmetry, which will be discussed in the following section.

The Brout-Englert-Higgs Mechanism

The Brout-Englert-Higgs mechanism [15, 16] introduces a complex scalar field,ϕ, which transforms as a doublet under $SU(2)$ gauge transformations. This allows to give a mass to all the particles with non-zero weak hypercharge. The scalar field spontaneously break the $SU(2)_L \otimes U(1)_Y$ symmetry and at the same time preserve the gauge symmetry of electromagnetism, according to

$$SU(2)_L \otimes U(1)_Y \to U(1)_{EM} \tag{2.25}$$

Introducing a $SU(2)_L$ doublet with $I = 1/2$, $I_3 = -1/2$ and $Y = 1$:

$$\phi(x) = \begin{pmatrix} \phi^+(x) \\ \phi^0(x) \end{pmatrix}_{Y=1} \tag{2.26}$$

where $\phi^{+,0}$ are complex fields.

The associated lagrangian is

$$\mathcal{L}_{\mathcal{H}} = (D_\mu\phi)^\dagger(D^\mu\phi) + V(\phi) \tag{2.27}$$

Where the potential, illustrated in Figure 2.2, is

$$V(\phi) = -\mu^2(\phi^\dagger\phi) + \lambda(\phi^\dagger\phi)^2 = -\mu^2\phi^2 + \lambda\phi^4 \tag{2.28}$$

The value of the field at the minimum of the potential is given by

$$\phi(x) = -\frac{1}{2}\frac{\mu^2}{\lambda} = \frac{v^2}{2} \tag{2.29}$$

In order to have a physical solution it must be $\lambda > 0$, otherwise the potential is not bounded from below. This choice defines a ground state, also known as *vacuum expectation value* (*vev*). Depending on the sign of μ^2, the ground state can be unique with a minimum in $\phi = 0$, for $\mu^2 > 0$, or degenerate for $\mu^2 < 0$. In the latter case, the minimum of the potential is obtained for a non-zero field value. The Lagrangian is still gauge invariant, but the vacuum expectation value v is not null. The value of the field in the minimum of the potential is given by $\phi^2 = \mu^2/2\lambda = v/2$.

The vacuum expectation value v can be evaluated using the relation

$$\frac{G_F}{\sqrt{2}} = \frac{g^2}{8m_W^2} \to v = \frac{2m_W}{g} = (\sqrt{2}G_F)^{-1/2} \tag{2.30}$$

Precision measurements of the Fermi constant G_F, from muon lifetime measurements, give $v = 246.22\,\mathrm{GeV}$ [18].

As a result of a gauge transformation, three out of the four components of the ϕ field can be set at 0, thus Equation 2.26 becomes

$$\phi(x) = \frac{1}{\sqrt{2}}\begin{pmatrix} 0 \\ v + h(x) \end{pmatrix} \tag{2.31}$$

where $h(x)$ is the scalar Higgs field.

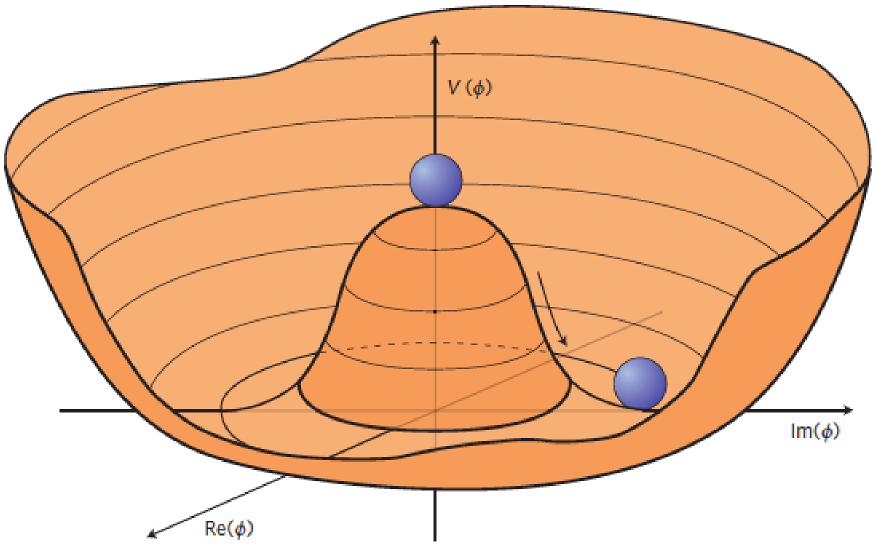

Figure 2.2: The *Mexican hat* potential that leads to spontaneous symmetry breaking. The vacuum, the lowest energy state, is described by a randomly chosen point at the bottom of the brim of the hat. The Higgs boson is a massive spin-zero particle corresponding to quantum fluctuations in the radial direction, oscillating between the centre and the sides of the hat [17].

Gauge Bosons Substituting the field $\phi(x)$ (Eq. 2.31), and the expressions for $W^{\pm}_{\mu}$ and B_{μ} (Eq. 2.16) in the kinetic part of the lagrangian density (Eq. 2.27), it is possible to obtain the masses for the vector bosons as

$$m_W = \frac{gv}{2} \tag{2.32}$$

$$m_Z = \frac{\sqrt{g^2 + g'^2}v}{2} \tag{2.33}$$

$$m_\gamma = 0 \tag{2.34}$$

From the definitions of m_W and m_Z one gets

$$\frac{m_W}{m_Z} = \cos(\theta_W) \tag{2.35}$$

Fermions For the fermions, it is necessary to introduce a Yukawa term, which represents the interaction between the Higgs field and the fermionic field.

For the electrons, for example, it holds

$$\mathcal{L}_{e\phi} = g_e \left((\bar{\nu}_e, \bar{e})_L \begin{pmatrix} \phi^\dagger \\ \phi^0 \end{pmatrix} e_R + e_R \left(\phi^{\dagger *}, \phi^{0*}\right) \begin{pmatrix} \nu_e \\ e \end{pmatrix}_R \right) \tag{2.36}$$

After the symmetry breaking, the choice of the unitary gauge, the following terms are generated

$$\mathcal{L}_{e\phi} = -\frac{g_e}{\sqrt{2}}v(\bar{e}_L\bar{e}_R + \bar{e}_R\bar{e}_L) - \frac{g_e}{\sqrt{2}}h(\bar{e}_L\bar{e}_R + \bar{e}_R\bar{e}_L) \tag{2.37}$$

The first term, $\frac{g_e}{\sqrt{2}}v(\bar{e}_L\bar{e}_R + \bar{e}_R\bar{e}_L)$ represents the mass of the electron, given by its coupling to the Higgs g_e and the vacuum expectation value v:

$$m_e = g_e\eta = \frac{g_e}{\sqrt{2}}v \tag{2.38}$$

The second term, $\frac{g_e}{\sqrt{2}}h(\bar{e}_L\bar{e}_R + \bar{e}_R\bar{e}_L)$ gives rise to an interaction between the Higgs boson and the electron. The same procedure applies to the other leptons and the down-type quarks. The masses for the up-type quarks are generated in a similar way when considering the hermitian conjugate of the Higgs doublet. In any case, the mass of all Dirac fermions is dynamically generated after the symmetry breaking and is defined by the coupling of the fermion to the Higgs field, as

$$m_f = g_f\eta = \frac{g_f}{\sqrt{2}}v \tag{2.39}$$

The coupling of the fermions to the Higgs boson results to be

$$g_f = \frac{m_f}{v} \tag{2.40}$$

Neutrinos are an exception, as right-handed neutrinos have zero weak hypercharge, they do not couple to the Higgs boson.

Higgs Boson The mass of the Higgs boson itself depends on two parameters of the potential $V(\phi)$: the vacuum expectation value v and the coupling parameter λ. The mass of the Higgs boson is a free parameter of the theory and its value m_H depends on the parameters of the potential. The Higgs boson was discovered in 2012 by the ATLAS and CMS collaborations at the Large Hadron Collider at CERN [19], [20].

Since then, the Higgs boson has been used to probe the Standard Model, but also to search for properties that would allow the existence of new physics. At the LHC, the main production mechanisms for the Higgs boson are: gluon-gluon fusion (ggF), vector-boson fusion (VBF), Higgs-strahlung (associated production with a gauge boson, VH) and an associated production with a pair ($t\bar{t}$) of top quarks (ttH) [21]. Various measurements have fixed the mass of the Higgs boson at $m_H = 125.25 \pm 0.17\,\text{GeV}$ [4].

All the particles discussed in the previous sections, as well as their properties are summarised in Figure 2.3.

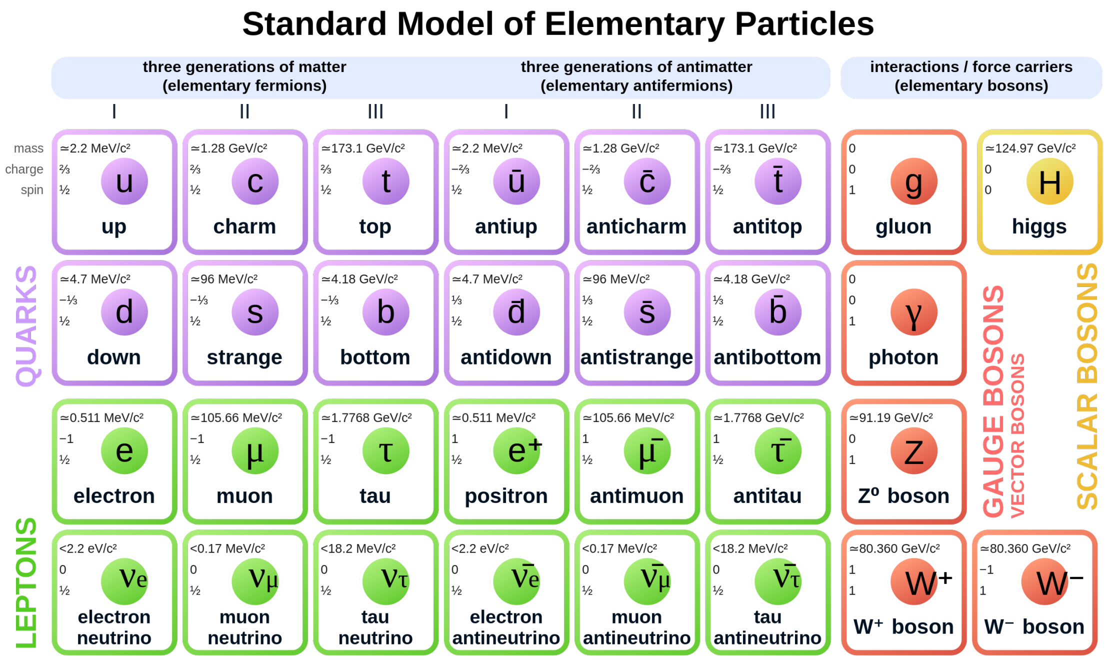

Figure 2.3: Scheme of the Standard Model of particle physics. On the left-hand side the three generation of fermions, in the centre the three generation of anti-fermions, on the right-hand side the force carriers and the Higgs boson.

2.2 Phenomenology of particle collisions

The proton-proton (pp) collisions that take place at the LHC (described in detail in Chapter 3) involve interactions among different constituents of the protons. The proton structure is explained at high energies by Richard Feynman's parton model [22]. The protons are made by three *valence quarks (u u d)*, by gluons and by *sea quarks*, which are fluctuation of gluon to a quark anti-quark pair called gluon-splitting. These constituents are called *partons*, any of these partons can interact in the collisions. The probability of a parton i carrying a momentum fraction x in a collision with a momentum transfer Q^2 is given by the Parton Distribution Functions $f_i(x, Q^2)$ [23] 2.4.

The pp collisions occur at a partonic centre-of-mass energy defined by $\sqrt{\hat{s}} = \sqrt{s x_1 x_2}$, where $\sqrt{s}$ is the centre-of-mass energy of the pp collisions and the indices represent the two incoming partons which participate in the reaction. Partons not taking part in the hard interactions are called spectator quarks and contribute to very soft additional processes called *underlying event*.

During the collisions, the quarks and gluons produced in the process emit QCD radiation in what is known as the *parton-showering* process. The parton showers (PS) can be initiated by a parton emission either from the two incoming partons

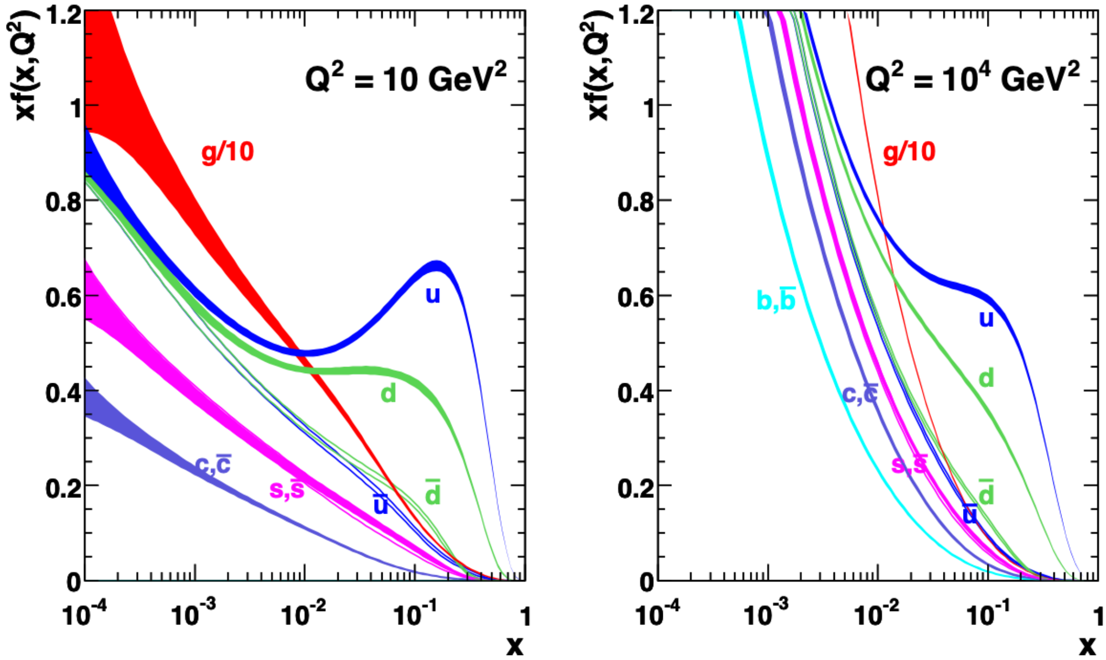

Figure 2.4: Proton distribution functions of gluons, valence and sea quarks inside the proton depending on two different values of Q^2 [23].

(initial state radiation (ISR)) or from the partons produced by the hard-scatter vertex (final state radiation (FSR)). The energy of the quarks and gluons in the shower decreases with time, and the strong interaction property of colour confinement prevents the observation of free coloured particles in nature. Consequently, it leads to the formation of collimated sprays of charged and neutral hadrons, known as *jets*, in a process called *hadronisation*. This process cannot be described using perturbative QCD, but relies instead on phenomenological models adapted to the experimental data. All the steps of the collisions are shown in Figure 2.5.

The factorisation theorem [25] states that the different sub-processes in the deep inelastic scattering can be factorised because they occur at different energy scales, therefore it is necessary to introduce an ad hoc energy scale, known as *factorisation scale* μ_F. The interaction cross-section can be divided into two parts: a non-perturbative long distance part (due to color confinement), given by Parton Density Functions (PDFs) f, and one perturbative short distance part (due to asymptotic freedom), given by $\hat{\sigma}_{ij\to X}$. The cross-section, for a process X, can then be written as

$$\sigma_{pp\to X} = \sum_{ij}\int_0^1 dx_i \int_0^1 dx_j \int f_i(x_i,\mu_F^2)f_j(x_j,\mu_F^2)\hat{\sigma}_{ij\to X}(x_ip_i, x_jp_j, \mu_R^2, \mu_F^2) \quad (2.41)$$

The subscripts i and j refer to the participating partons, and the sum is performed over all the possible partons combinations. The function f are the

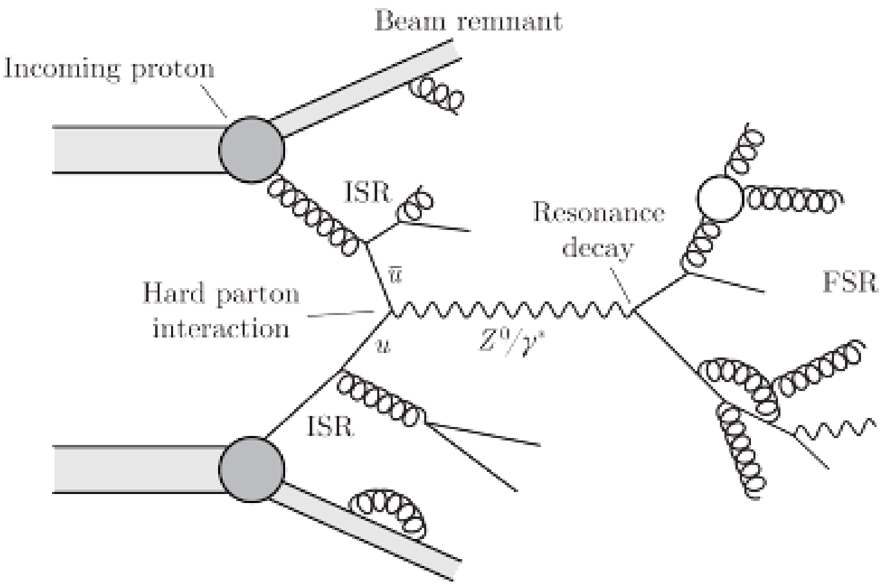

Figure 2.5: Illustration of an LHC proton-proton collision [24].

PDFs, μ_R is the renormalisation scale and μ_F is the factorisation scale, all these parameters will be described in detail in the following.

The functions f_i and f_j, indicate the proportion of momentum denoted as x_i carried by the parton i when the protons are probed at an energy scale μ_F. The scale for the perturbative regime is of the order $1\text{GeV}^2 \leq \mu_F < Q^2$.

The evolution of the PDFs with respect to the energy scale μ_F is described by the Dokshitzer-Gribov-Lipatov-Altarelli-Parisi (DGLAP) equations [26]. The shape of the PDF is determined experimentally in events such as lepton-proton scattering, jet production, and Drell-Yan events [27], [28].

The partonic cross-section $\hat{\sigma}_{ij\to X}$, is affected by both the factorisation scale and the renormalisation scale. In particular μ_R controls the divergent contributions appearing in the calculations beyond Leading Order (LO). The renormalisation scale can be varied when modelling these calculations in Monte Carlo (MC) simulations to derive an uncertainty on the predicted cross-section, because the choice of the scale is arbitrary.

$\hat{\sigma}_{ij\to X}$ can be calculated perturbatively as a function of the strong coupling α_S [4], therefore it also depends on the scale at which α_S is evaluated:

$$\sigma_{pp\to X} = \alpha_S\sigma_0 + \alpha_S\sigma_1 + \alpha_S^2\sigma_2 + ... \qquad (2.42)$$

The first term, σ_0, is the leading order, the second term corresponds to the next-to-leading order (NLO) correction and so on. These higher order terms in α_S are associated with radiative corrections as a result of gluon or quark emission.

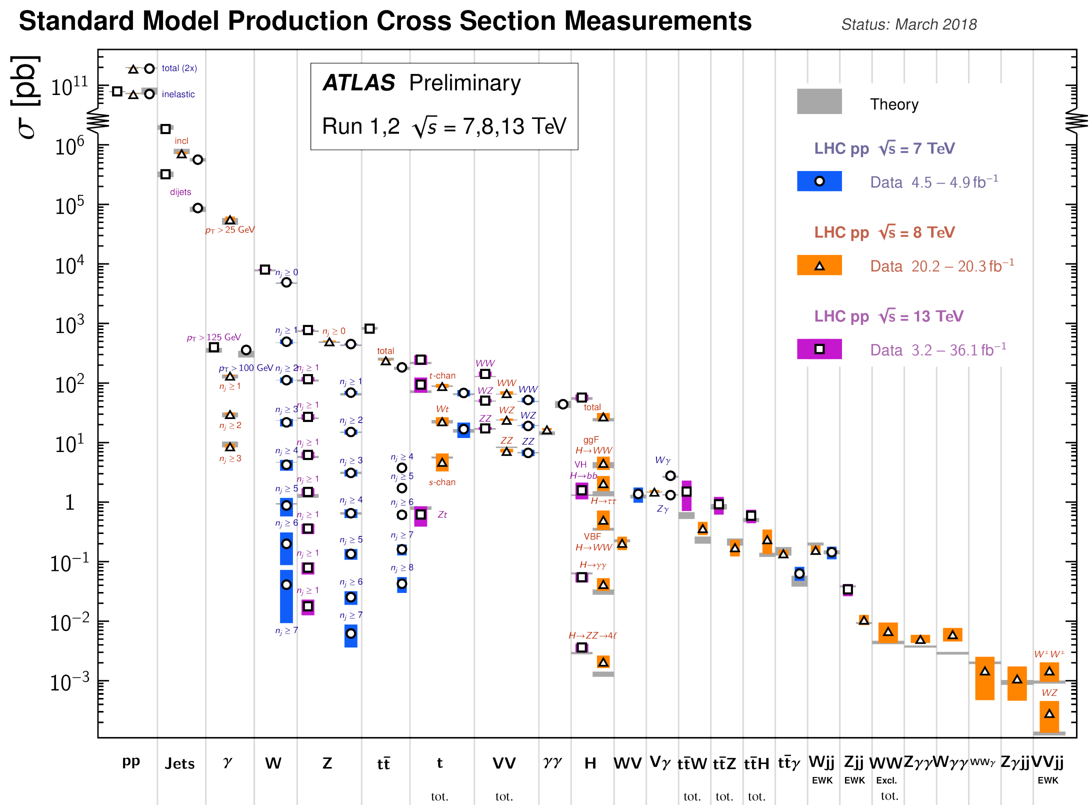

Figure 2.6: Cross sections as a function of different final states. The theoretical predictions are shown in grey, while the blue, orange and violet points represent the LHC measurements at $\sqrt{s} = 7, 8, 13$ TeV respectively [29].

The scale parameters are chosen arbitrarily and they are not intrinsic to QCD. The standard value is taken as $\mu_F = \mu_R = Q^2$. Ideally, a physical observable should not depend on these scales and cross-section calculated for any values of the parameters should remain invariant. But this is only true if all the perturbative orders are included in the calculation which is theoretically as well as practically impossible. One can reduce the scale dependency by including more and more terms in the calculation. The scale dependence is usually assigned as an uncertainty in the theoretical calculations due to missing higher orders terms.

Over the course of several years, a good agreement has been observed between the experimental observations and the theoretical predictions derived from simulations implementing the above calculations. Figure 2.6 presents a comprehensive overview of the production cross-section in proton-proton collisions for diverse Standard Model processes, revealing that the agreement persists across a vast range of 14 orders of magnitude [29].

2.3 Physics of the top quark

This thesis will address a specific measurement regarding the top-quark properties and production mechanism, hence this section will give an overview of the physics of the top quark, exploiting its properties and its importance in current studies.

The existence of the top quark was postulated by M. Kobayashi and T. Maskawa in 1973 [30],[31] and finally discovered by the CDF and D0 collaborations at the Tevatron (Fermilab) in 1995 [32]. Its mass is currently measured as 173.34±0.98 GeV, which is an average of the Tevatron and LHC measurements [33]. The top quark has short lifetime, $\tau_t = 0.5 \cdot 10^{-24}$ s, which is an order of magnitude shorter than the average time required for a parton to hadronise, meaning that the top quark is the only quark that can be observed in the free state.

Another important property of the top quark is its Yukawa coupling with the Higgs mass. The coupling has a value of

$$g_t = \frac{\sqrt{2}m_t}{v} \sim 1 \tag{2.43}$$

Possible deviation of g_t from the expected value may indicate new physics effects that come into play to modify the effective coupling between the top-quark and the Higgs field.

2.3.1 Top quark production

In proton-proton collisions, top quarks can be produced in pairs or singly, either via the strong or the electroweak interaction. Both production modes are described in the following paragraphs.

$t\bar{t}$ production

The dominant top quark production mechanism at hadron colliders is via strong interactions. At the LHC, gluon-gluon fusion ($gg \to t\bar{t}$) is responsible for 90% of $t\bar{t}$ production, while quark-antiquark annihilation ($q\bar{q} \to t\bar{t}$) accounts for the remaining 10% [4].

The leading order Feynman diagrams for both processes are shown in Figure 2.7.

Predictions for the total top-quark production cross sections are available at next-to-next-to-leading-order (NNLO) in perturbation theory, including the next-to-next-to-leading-log (NNLL) soft gluon resummation. The cross section is

$$\sigma_{t\bar{t}}\,(m_t = 172.5\text{GeV}, \sqrt{s} = 13\,\text{TeV}) = 831.8^{+19.8+35.1}_{-29.2-35.1}\,\text{pb} \tag{2.44}$$

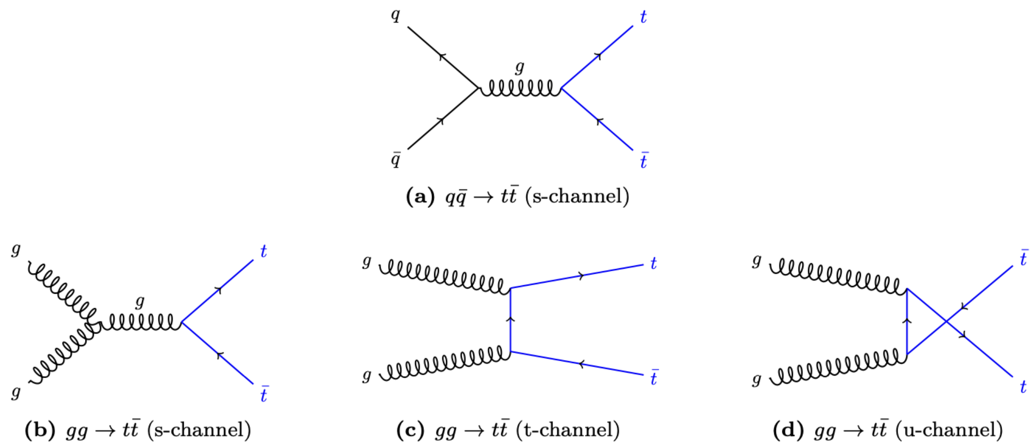

Figure 2.7: Leading-order (LO) Feynman diagrams for top-quark pair production.

where the first uncertainty comes from the scale dependence and the second from the parton distribution functions [4]. Figure 2.10 shows the evolution of the $t\bar{t}$ cross section from theoretical calculations and experimental measurements as a function of the centre-of-mass energy and luminosity for different experiments at the LHC. The experimental measurements are in good agreement with the prediction, indicated by different markers. In this thesis, the relevant centre-of-mass energy is $\sqrt{s} = 13\,\text{TeV}$ with an integrated luminosity of $L = 140\,\text{fb}^{-1}$.

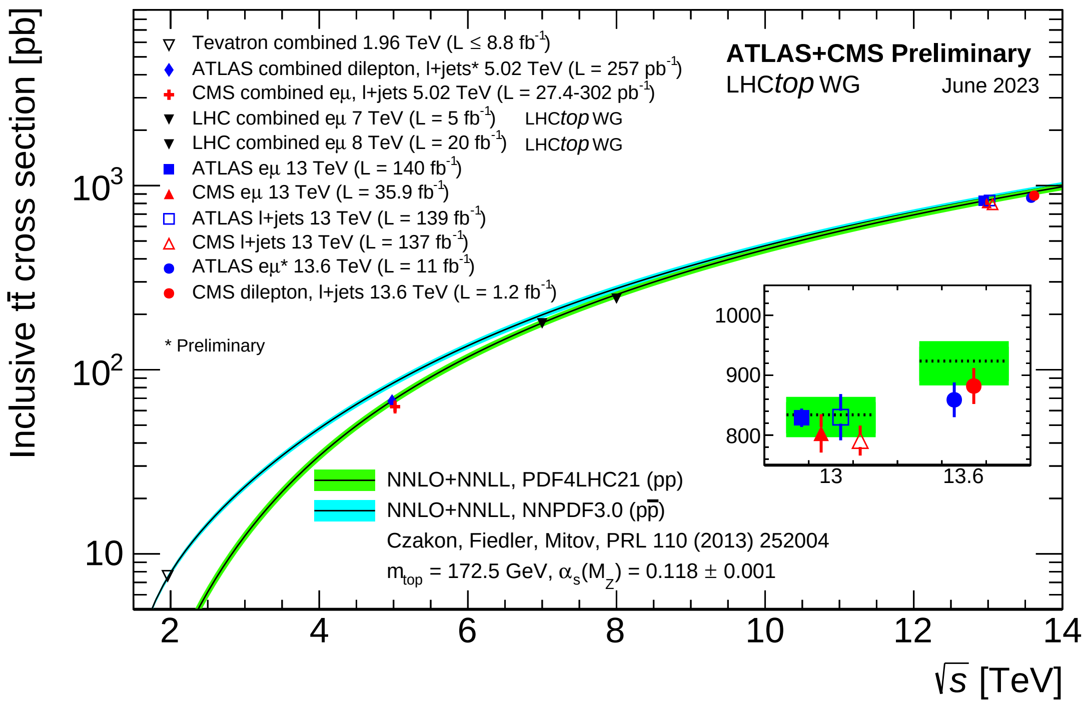

Figure 2.8: Summary of LHC and Tevatron measurements for the $t\bar{t}$ production cross-section as a function of the centre-of-mass energy compared to the NNLO QCD calculation complemented with NNLL resummation (Nov. 2023) [34]. In this thesis, the relevant centre-of-mass energy is $\sqrt{s} = 13\,\text{TeV}$ with an integrated luminosity of $L = 140\,\text{fb}^{-1}$.

Single top quark production

Single top quarks can be produced via electroweak interactions, which allows the creation of a quark flavour via the exchange of a W boson. The leading order Feynman diagrams for single top production are shown in Figure 2.9.

t-channel In this channel, a bottom quark turns into a top quark by exchanging a virtual W-boson with the emission of an up-type quark q (or anti-quark $\bar{q}$). This process is the dominant mechanism for single-top production at the LHC ($\sqrt{s} = 13\,\text{TeV}$). The NNLO cross section for t-channel single top quark production ($t + \bar{t}$) is calculated for $m_t = 173.2\,\text{GeV}$:

$$\sigma_{t+\bar{t}}\,(\sqrt{s} = 13\,\text{TeV}) = 215^{+2.1}_{-1.3}\,\text{pb} \tag{2.45}$$

The uncertainty results from a variation of the renormalisation scale between $\mu = 1/2m_t$ and $\mu = 2m_t$ [4].

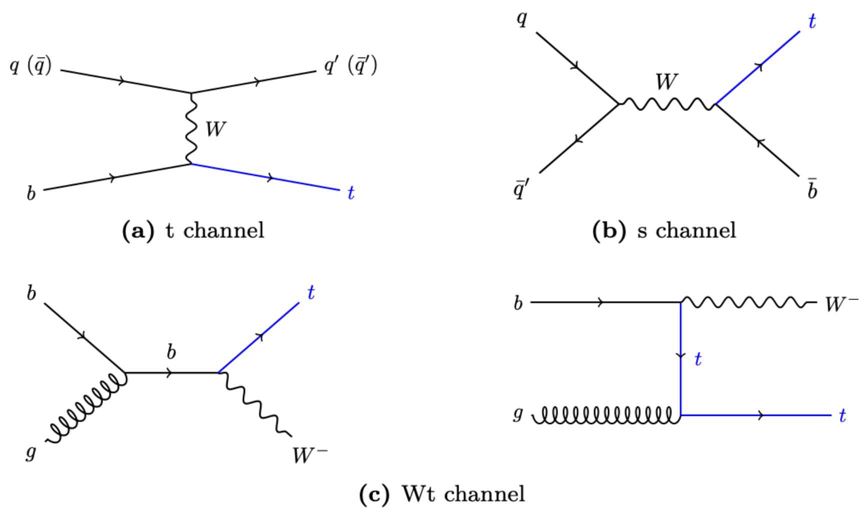

Figure 2.9: Leading-order (LO) Feynman diagrams for single-top production: a) t-channel , b) s-channel and c) Wt-channel.

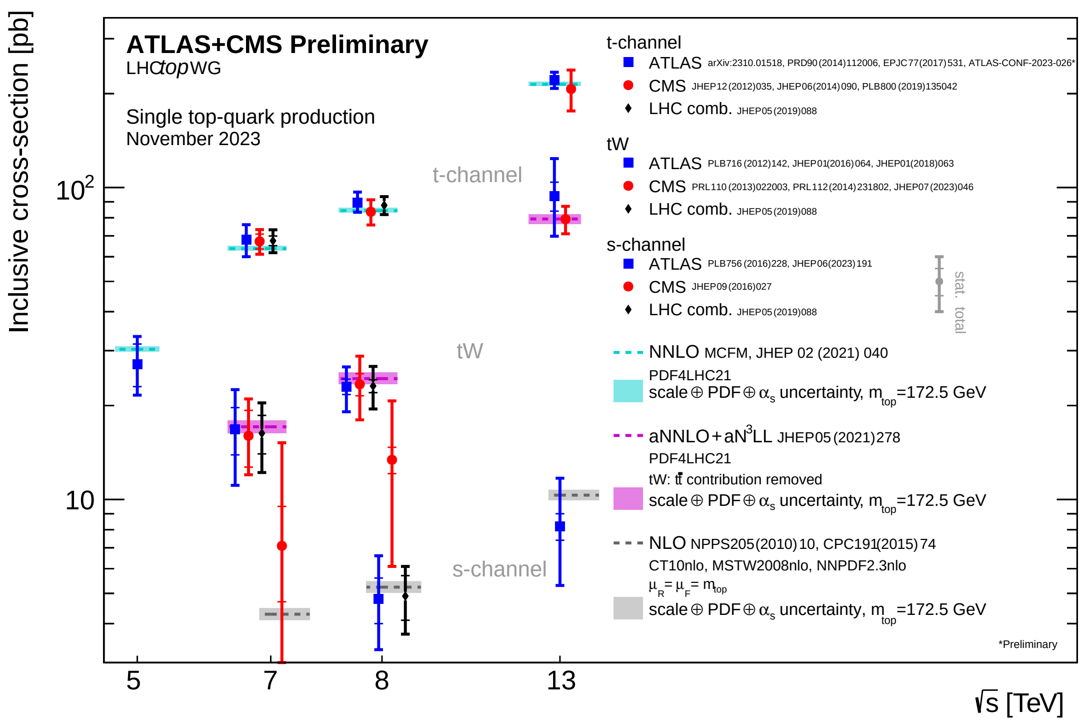

Figure 2.10: Summary of ATLAS and CMS measurements of the single top production cross-sections in various channels as a function of the center of mass energy. The measurements are compared to theoretical calculations based on: NLO QCD, aNNLO QCD complemented with aN3LL resummation and NNLO QCD. (Nov. 2023) [34]. In this thesis, the relevant centre-of-mass energy is $\sqrt{s} = 13\,\mathrm{TeV}$ with an integrated luminosity of $L = 140\,\mathrm{fb}^{-1}$.

s-channel In the s-channel, a pair of quark and anti-quark combines to form a W-boson, which subsequently decays into a top (anti-top) and anti-bottom (bottom) quark. This channel has the smallest non-negligible contribution to single top production. The cross section at NNLO for the LHC is [4]

$$\sigma_{t+\bar{t}}\,(\sqrt{s} = 13\,\mathrm{TeV}) = 10.03^{+0.29+0.27}_{-0.24-0.27}\,\mathrm{pb} \tag{2.46}$$

Wt-channel Single top quarks can be also produced in association with W-bosons. At NNLO, for the LHC, the production cross section is [4]

$$\sigma_{t+\bar{t}}\,(\sqrt{s} = 13\,\mathrm{TeV}) = 71.7^{+1.8+3.40}_{-1.8-3.40}\,\mathrm{pb} \tag{2.47}$$

Any analysis carried out in the tW channel must face the same challenge: the close similarity of this process to $t\bar{t}$ production. Experimentally, it is a challenge to separate collisions where this process has occurred from those where pair production has occurred. Thus, measurements of tW depend crucially on this separation and on estimating the effects that $t\bar{t}$ has on the extraction of tW. This challenge is the focus of this thesis.

Others

The remaining top quark production processes with smaller cross sections in proton-proton collisions are not always classified in the same group. The processes in which the top-quarks in the final state are accompanied by other vector bosons are called *associated production* modes. Most of them have a top-antitop quark pair in their final state with a boson: ttZ, ttW, $tt\gamma$ and ttH. There are also *single-top associated production* processes: tZq, $t\gamma$, tWZ, tH or tHW. There are other processes which cannot be considered as associated production or which have a very small production cross section. Within this category is the $tttt$ process, which has recently been studied by both ATLAS and CMS collaborations at CERN [4].

2.3.2 Top-quark decay

The top quark decays almost exclusively via

$$t \to W^+ b \tag{2.48}$$

with a probability of $|V_{tb}|^2 \sim 99.8\%$ [4].

The W^+ boson then decays either leptonically into a charged lepton and its corresponding neutrino according to

$$W^+ \to l^+ \nu_l \tag{2.49}$$

where l can be either e, μ or τ.

Or it can decay hadronically into a pair of quark and anti-quark

$$W^+ \to q\bar{q} \tag{2.50}$$

where q and $\bar{q}$ are up- and down-type quark respectively. Since quarks exist in three colours and there are three possible leptonic decays, this gives a total of 6 possible W boson decays. The W boson decays 33.5% of the times in leptons and 66.5% of the times in hadrons [4]. Figure 2.11 shows, in a pie chart, the decay channels of the the W boson.

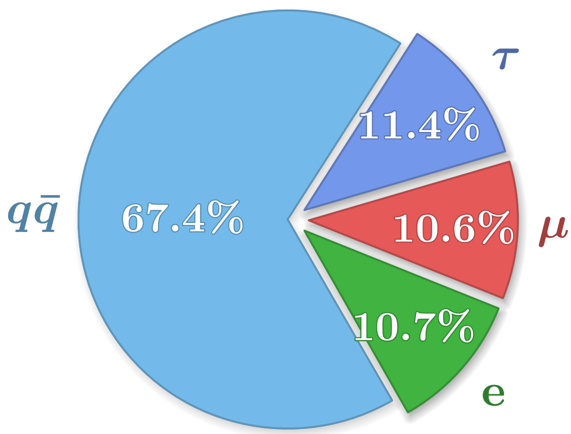

Figure 2.11: Pie chart of the W decay channels. The hadronic decay is shown in blue, while the three different leptonic decays are shown in purple, red and green [35].

$t\bar{t}$ and single top events can then be classified into three broad categories according to the decays of the W bosons resulting from the decays of the top and anti-top quarks, respectively.

It should be noted that the τ lepton has a lifetime of less than 10^{-14} s [4] and therefore it decays before reaching the first layer of the detector. Like the top quark, τ leptons decay through a W boson or into a e/μ and $\bar{\nu}_{e/\mu}$. Additionally, in both cases, a τ neutrino is present. Therefore, in the $t\bar{t}$ final states, often only stable charged leptons (e and μ) are considered, including those coming from τ lepton decays.

Hadronic decay channel A $t\bar{t}$ event is conventionally referred to in LHC analyses as all-hadronic if both the W^+ and W^- bosons decay into quarks, according to

$$t\bar{t} \to W^+ b W^- \bar{b} \to q\bar{q}' b q'' \bar{q}''' \bar{b} \tag{2.51}$$

All-hadronic events are characterised by six jets in the final state: four light- jets and two b-jets. The frequency of this process is 45.7%, which makes this channel the dominant $t\bar{t}$ decay channel. Despite the high abundance of this decay, it is very difficult to reconstruct the top quarks due to the large jet multiplicity [4].

Di-leptonic decay channel In this channel both W-bosons decay leptonically, according to

$$t\bar{t} \to W^+ b W^- \bar{b} \to l^+ \nu_l b l^- \bar{\nu}_l \bar{b} \tag{2.52}$$

where $l = e, \mu, \tau$. This process occurs with a probability of 10.5%, the small branching fraction for this channel results in low statistics. The detector signature is characterised by two b-quark jets, two oppositely charged leptons and the absence of transverse energy from the two neutrinos [4].

Semi-leptonic decay channel A $t\bar{t}$ event in which one W-boson decays into leptons and the other into quarks is classified as semileptonic, according to

$$t\bar{t} \to W^+ b W^- \bar{b} \to q\bar{q}' b l^- \bar{\nu}_l \bar{b} \tag{2.53}$$

The occurrence of this process is 43.8%, therefore comparable to that of the all-hadronic channel. The detector signature includes four jets, one charged lepton and missing transverse energy from the neutrino [4].

2.3.3 Study of $t\bar{t}$ and tW interference

When the tW process is studied experimentally at NLO in QCD, it is found to have final states that it shares with $t\bar{t}$, namely the $WbWb$ final state.

Given the theoretical framework for simulating these processes, it is not possible to use tW and $t\bar{t}$ as completely separate processes, since the processes are characterised by their final states.

Historically, most analyses use separate tW and $t\bar{t}$ Monte Carlo (MC) simulations at NLO in QCD. However, this separation poses a number of challenges.

First, there will be events corresponding to Feynman diagrams that can be in both tW and $t\bar{t}$, leading to double counting of events if both samples are used simultaneously. Secondly, the effect of interference between the Feynman diagrams is ignored when calculating the squared amplitude of the matrix element. In tW and $t\bar{t}$ at NLO in QCD, Feynman diagrams that can have a top-antitop pair on-shell are called *doubly resonant* diagrams (and come from the $t\bar{t}$ process), while those where only one can be on-shell are called *singly resonant* diagrams (and come from tW).

To describe the interference let's introduce the notation $A_{\alpha\beta}$ as the $O(g_W\alpha_s)$ amplitude of the process:

$$\alpha + \beta \rightarrow t + W + \delta \tag{2.54}$$

where δ is the parton (identified as the b-quark), that can be omitted in the notation.

The total amplitude of $tW + t\bar{t}$ process is therefore:

$$\mathcal{A}_{\alpha\beta} = \mathcal{A}^{(tW)}_{\alpha\beta} + \mathcal{A}^{(t\bar{t})}_{\alpha\beta} \tag{2.55}$$

where the two terms are respectively the singly and doubly resonant contributions diagrams to the tWb cross-section.

At NLO, the amplitude of the process becomes:

$$|\mathcal{A}_{\alpha\beta}|^2 = |\mathcal{A}^{(tW)}_{\alpha\beta}|^2 + 2Re\mathcal{A}^{(tW)}_{\alpha\beta}\mathcal{A}^{(t\bar{t})}_{\alpha\beta}| + \mathcal{A}^{(t\bar{t})}_{\alpha\beta}|^2 \tag{2.56}$$

$$\equiv \mathcal{S}_{\alpha\beta} + \mathcal{I}_{\alpha\beta} + \mathcal{D}_{\alpha\beta} \tag{2.57}$$

the first term, $\mathcal{S}_{\alpha\beta}$, is associated to the single-top production diagrams, the second, $\mathcal{I}_{\alpha\beta}$, is the interference term and the third, $\mathcal{D}_{\alpha\beta}$, is the contribution from $t\bar{t}$.

There are several approaches to deal with the interference between tW and $t\bar{t}$, i.e. to remove the $\mathcal{I}_{\alpha\beta}$ term from the amplitude calculation.

The NLO real-emission contribution to the subtracted short-distance partonic cross-section including the flux factor and phase space is:

$$d\hat{\sigma} = \frac{1}{2s}\left(\hat{\mathcal{S}}_{\alpha\beta} + \mathcal{I}_{\alpha\beta} + \mathcal{D}_{\alpha\beta}\right) d\phi_3 \tag{2.58}$$

where $d\phi_3$ is the three-body final state phase-space, while the hat on $\mathcal{S}$ denotes that the infrared singularities have been subtracted.

The hadron production cross-section can be written as

$$d\sigma = d\sigma^{(2)} + \sum_{\alpha\beta}\int dx_1 dx_2 \mathcal{L}_{\alpha\beta} d\hat{\sigma}_{\alpha\beta} \tag{2.59}$$

$d\sigma^{(2)}$ indicates the contribution to the cross-sections that are not already included (Born, soft-virtual,..), and $\mathcal{L}_{\alpha\beta}$ is the parton-level luminosity. The Diagram

Removal (DR) and Diagram Subtraction (DS) cross-sections, become (Ref. [36] for detailed calculation)

$$d\sigma^{DR} = d\sigma^{(2)} + \sum_{\alpha\beta} \int \frac{dx_1 dx_2}{2x_1 x_2 s} \mathcal{L}_{\alpha\beta} \hat{\mathcal{S}}_{\alpha\beta} d\phi_3 \tag{2.60}$$

$$d\sigma^{DS} = d\sigma^{(2)} - d\sigma^{subt} \tag{2.61}$$

where $d\sigma^{subt}$ is designed to remove numerically the doubly-resonant contribution and $\tilde{\mathcal{D}}_{\alpha\beta}$ is defined such that $\mathcal{D}_{\alpha\beta} - \tilde{\mathcal{D}}_{\alpha\beta}$ will vanish when $m^2_{\bar{b}W} \to m^2_t$.

The DR cross section is not gauge-invariant. However, this is not a problem in practice, as it can be made gauge-invariant by repeating the DR calculation in a number of alternative gauges. The difference between the two equations in 2.60 is as follows:

$$d\sigma^{DR} - d\sigma^{DS} = \sum_{\alpha\beta} \int \frac{dx_1 dx_2}{2x_1 x_2 s} \mathcal{L}_{\alpha\beta} (\hat{\mathcal{S}}_{\alpha\beta} + \mathcal{I}_{\alpha\beta} + \mathcal{D}_{\alpha\beta} - \tilde{\mathcal{D}}_{\alpha\beta}) d\phi_3 \tag{2.62}$$

that depends on the interference term and the $\mathcal{D}_{\alpha\beta} - \tilde{\mathcal{D}}_{\alpha\beta}$ difference.

A gauge invariant subtraction term can be found by choosing an appropriate value of the $\tilde{D}_{\alpha\beta}$.

Writing all this calculations in amplitudes notation one gets:

$$|\mathcal{A}_{\alpha\beta}|^2_{DR} = |\mathcal{A}^{tW}_{\alpha\beta}|^2 \qquad |\mathcal{A}_{\alpha\beta}|^2_{DS} = |\mathcal{A}^{tW}_{\alpha\beta}|^2 - \left[|\mathcal{A}^{tW}_{\alpha\beta} + \mathcal{A}^{t\bar{t}}_{\alpha\beta}|^2 - C^{SUB} \right] \tag{2.63}$$

with C^{SUB} cross-section level subtraction term. From these equations one gets:

$$|\mathcal{A}_{\alpha\beta}|^2_{DR} - |\mathcal{A}_{\alpha\beta}|^2_{DS} = 2\mathrm{Re}\{\mathcal{A}^{tW}_{\alpha\beta} \mathcal{A}^{t\bar{t}}_{\alpha\beta}\} \tag{2.64}$$

The use of these separate and combined samples requires, as mentioned, the modification of the tW sample. This modification requires the addition of an additional source of uncertainty consisting of the difference between the Monte Carlo simulations for DR and DS approaches.

Another possibility is to work directly with the $WbWb$ final state, including all interference terms between tW and $t\bar{t}$ by construction, defined as $bb4l$. The ATLAS collaboration has published extensive studies at the generator level [37, 38].

The interference between $t\bar{t}$ and tW has already been studied by the ATLAS experiment at the LHC (see Chapter 3 for details on the experimental setup) in the dileptonic channel [10]. The result of the paper is shown in Figure 2.12, which shows the normalised cross section as a function of a variable sensitive to the interference. The black dots represent the data with its associated statistical uncertainty, the colored dots represent the different theoretical predictions. Diagram Removal is shown in red, Diagram Subtraction in green and the *bb4l* prediction is shown in purple. The lower panel shows the ratio of the theoretical predictions to the data and DR and DS predictions show tension with respect to the data.

The $t\bar{t}$ and tW interference in the single lepton channel has never been exploited and is the focus of this thesis.

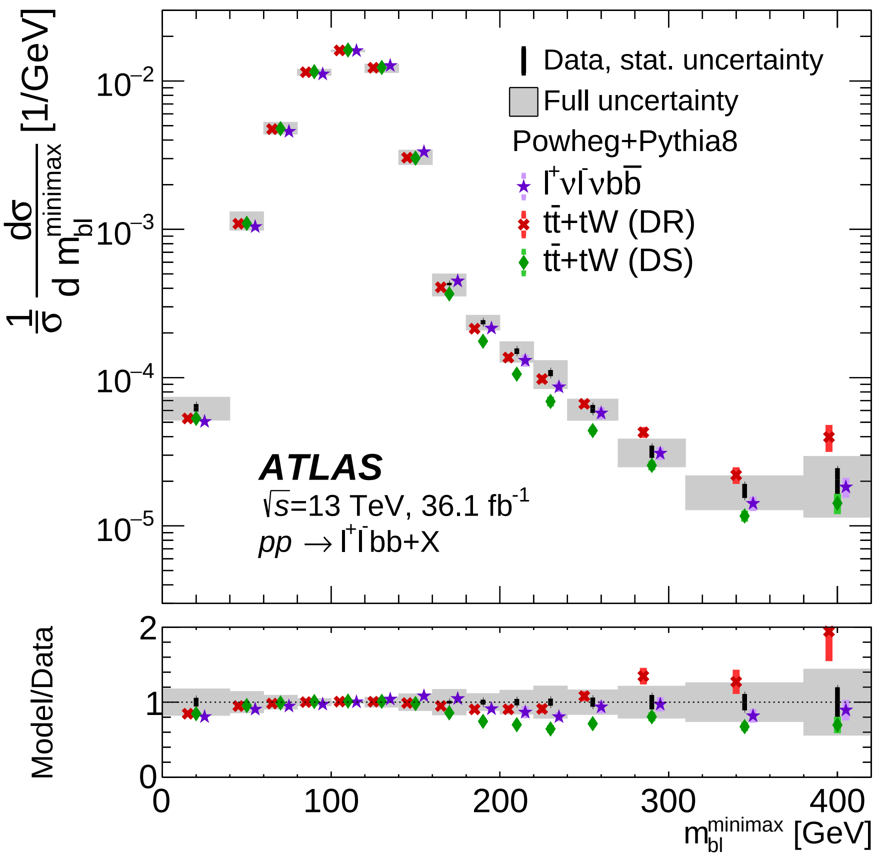

Figure 2.12: The unfolded normalized $m_{bl}^{minimax}$ distribution along with various Monte Carlo (MC) predictions of the $t\bar{t}+tW$ signal. The uncertainty on the data includes all statistical and systematic sources, while uncertainties for each of the MC predictions correspond to variations of the PDF set and renormalization and factorization scales. The data are compared to predictions using the Diagram Removal (red), Diagram Subtraction (green) and the *bb4l* (purple) scheme [10].

2.4 Shortcomings of the Standard Model

The Standard Model has been tested several times throughout the years and and while there is ample evidence supporting its validity, there are also valid reasons to believe that the SM may not be complete.

- **Matter Anti-matter Asymmetry** The observable universe primarily consists of matter rather than antimatter, despite the expectation that equal amounts of both should have been generated following the Big Bang through CP-conserving processes, while the SM CP-violating processes are insufficient to account for the observed imbalance between matter and antimatter [39].

- **Neutrino Oscillations** The Standard Model assumes that neutrinos are massless, but experiments have shown that neutrinos do have mass. An extension of the Standard Model is required to incorporate neutrino masses and oscillations [40] [41] [42].

- **Gravitational Force** The gravitational interactions between fundamental particles are not described in the Standard Model, that appears to be valid only until the Planck scale ($\theta(10^{(19)}\mathrm{GeV})$ [43].

- **Higgs-boson Mass** The coupling of the Higgs boson to the other particles is directly proportional to their respective masses. In consequence, any (so far unobserved) new particle would yield a significant contribution to the Higgs-boson mass through loop diagrams. If these quantum corrections are not canceled or finely adjusted, they would result in a substantial mass for the Higgs boson, creating a significant disparity between the electroweak scale (which pertains to the masses of W and Z bosons) and the Planck scale. Based on the quantum corrections, it is expect the mass of the Higgs boson to be much larger than what is actually observed. The fact that the Higgs boson has a relatively light mass, raises inquiries as to why quantum corrections do not drive it towards significantly higher values. To explain this problem, known as the *hierarchy problem*, an extension of the SM is needed [44].

- **Dark Matter** There are astrophysical evidences for the existence of the DM, such as: rotational velocities of galaxies, measurements of the cosmic microwave background and gravitational lensing. This matter, not accounted for by the Standard Model, constitutes 24% of our universe.

- **New Physics** There is evidence of inconsistencies between the predictions of the Standard Model (SM) and the empirical observations, as lepton flavour universality in B meson decays [45] and the anomalous magnetic dipole moment of muons [46].

3
The ATLAS experiment at the LHC

3.1 The Large Hadron Collider

The Large Hadron Collider (LHC) [3] is a circular accelerator located at Conseil Européen pour la Recherche Nucléaire (CERN), at the Swiss-French border near Geneva. It is situated approximately 100 m underground and it has a circumference of about 27 km. It is placed in the tunnel that was initially constructed, between 1984 and 1989, for the Large Electron Positron (LEP) collider [47].

The LHC accelerates two beams consisting of bunches of protons (or heavy ions) in opposite directions around its ring. To keep the particles on a circular trajectory LHC uses 1232 dipole magnets capable of generating a magnetic field of 8.33 T and 858 additional quadrupoles are located along the ring to focus the beam. Eight Radio Frequency (RF) cavities are placed along the ring to accelerate the particles as they pass. If the particle with the target energy passes when the electric field is zero, it will not be accelerated, while more (less) energetic particles will be accelerated (decelerated). This means that the particles get clumped in the so-called *bunches*. Particle bunches are formed in an earlier acceleration stage involving several accelerators from the CERN complex, the procedure of which is explained below. There are 2808 bunches per beam and each bunch, in Run 2, can contain up to $1.15 \cdot 10^{11}$ protons. The bunches collide at four Interaction Points (IP), where the main experiments of the LHC are placed: ATLAS [12], CMS [48], ALICE [49] and LHCb [50]. ATLAS and CMS are multi-purpose experiments, ALICE is specialised in heavy ion collisions, while LHCb focuses on B-meson decays. Figure 3.1 shows the accelerator complex.

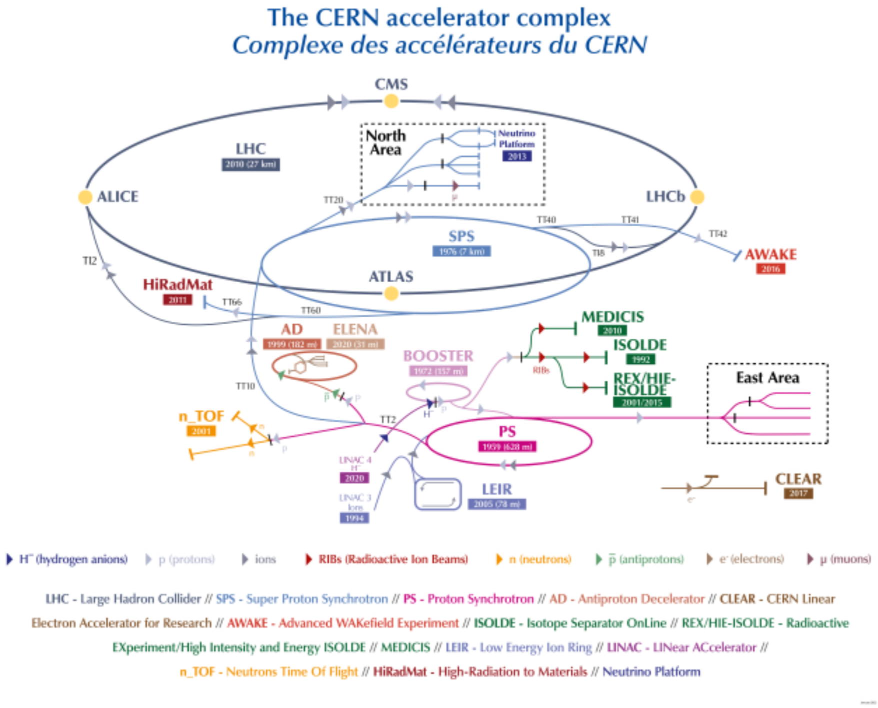

Figure 3.1: The CERN accelerator complex, in 2022 [51].

The proton source is where it all starts at the LHC. Hydrogen gas is injected into the Linac2 (Linac4 in Run3), which returns protons accelerated to 50 MeV. The protons are subsequently accelerated to higher energies by the Proton Synchrotron Booster (PBS), the Proton Synchrotron (PS), and the Super Proton Synchrotron (SPS). Finally, the protons are transferred to the LHC rings, where they reach the final energy. After reaching the final centre-of-mass energy, the bunches are circulated for $\sim$ 10 hours, with a frequency of 25 ns.

The LHC operation is divided into distinct periods: Run (when data is collected) and Long Shutdown (LS). Run 1 and Run 2 took place between 2009 and 2013 and between 2015 and 2018, respectively. Run 3 began in the summer of 2022 and it will extend up to 2025. Throughout the LS, the LHC underwent several upgrades: during LS1 the centre-of-mass energy was increased from 8 to 13 TeV, and during LS2, significant upgrades were made to the LHC accelerator complex, and the centre-of-mass energy was increased again from 13 to 13.6 TeV. During the next Long Shutdown (LS3) the LHC will be upgraded to the High-Luminosity LHC (HL-LHC) [52], resulting in a collision rate that is five times higher than in the original design of the LHC.

3.1.1 Luminosity and pile-up

At LHC, the rate of *pp* collisions per second leading to a process X is given by:

$$\frac{dN_X}{dt} = \mathcal{L} \cdot \sigma_X \tag{3.1}$$

where σ_X is the cross section of the process under study and $\mathcal{L}$ is the instantaneous luminosity. The luminosity is measured in $\mathrm{cm^{-2}\,s^{-1}}$, or alternatively in *barn* ($1\,\mathrm{b} = 10^{24}\,\mathrm{cm^{-2}\,s^{-1}}$).

The machine luminosity depends on the beam parameters and can be written as:

$$\mathcal{L} = \frac{N_1 N_2 f_{rev} N_b}{4\pi\sigma_x\sigma_y} \cdot F \tag{3.2}$$

where N_1, N_2 are the number of protons per bunch in the beams, f_{rev} is the revolution frequency and N_b the number of bunches crossing at the interaction point. Therefore the total factor $f_{rev}N_b$ represents the number of bunch crossings per time unit. The term F is the so-called luminosity reduction factor, which accounts for non-zero collision angles, while the terms σ_x, σ_y are the transverse sizes of the bunches in the x, y directions.

When the beams are accelerated, the particles are forced into a circular orbit by the magnets and tend to oscillate around the direction of propagation.

The integral of the instantaneous luminosity over a period of time is called the integrated luminosity and it is a measure of the number of events. It is expressed as the inverse of a cross-section, in barns. Figure 3.2 shows the luminosity reached, year by year, by the ATLAS experiment during Run 2.

The luminosity in the LHC is not constant over a physics run but can decay due to intensity degradation, or the so-called *lumi levelling.*

The detectors collect data during an LHC *fill*, a period during which the beams circulate and collide in the LHC machine. Data acquisition is possible as soon as the LHC declares *stable beams*, a condition indicating that stable particle collisions have been achieved. Each of the data sets taken during the continuous recording of the detector is referred to as a *run.* Each run in subdivided into Luminosity Blocks (LB), typically corresponding to 1-2 minutes of data taking. Sometimes the detector is prone to problems that can prevent the sub-detector systems to perform correctly, therefore not all the data collected is usable. The data that can be used for physics analyses is named *Good for Physics.*

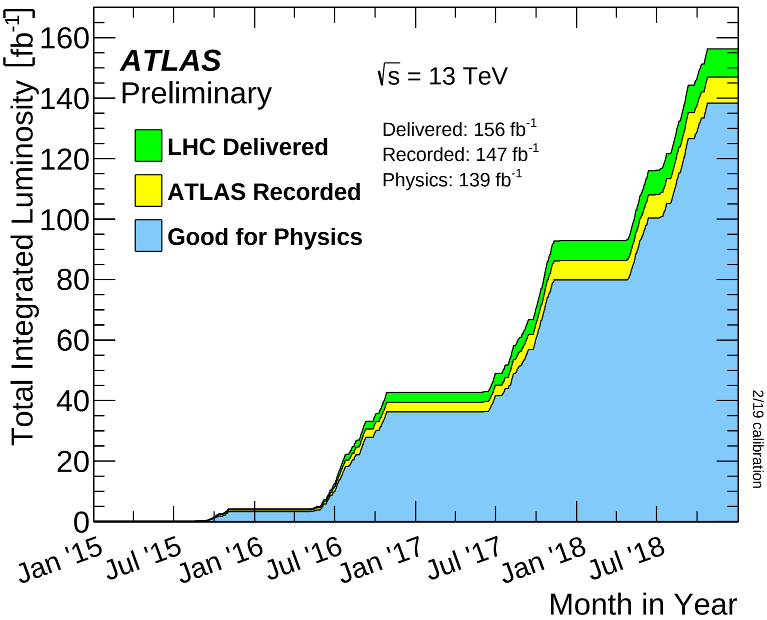

Figure 3.2: Cumulative integrated luminosity delivered to and recorded by ATLAS between 2015 and 2018 during stable beams pp collision data-taking at $\sqrt{s} = 13\,\text{TeV}$. The total luminosity delivered by the LHC is shown in green, the luminosity recorded by ATLAS is shown in yellow and the luminosity good for physics is shown in blue [53].

As mentioned in the previous section, the number of protons produced per bunch is high, therefore more than one collision can happen per bunch crossing. This number is indicated by the *Pile-Up* (PU) μ:

$$\langle\mu\rangle \approx \mathcal{L}\tau_{bc}\sigma \tag{3.3}$$

σ is the cross section for the collisions, while τ_{bc} is the time between bunch crossing. Figure 3.3 shows the average number of overlapping events in a bunch crossing. The number is Poisson distributed with average $<\mu>$, the average value for the full Run 2 is $<\mu>= 33.7$.

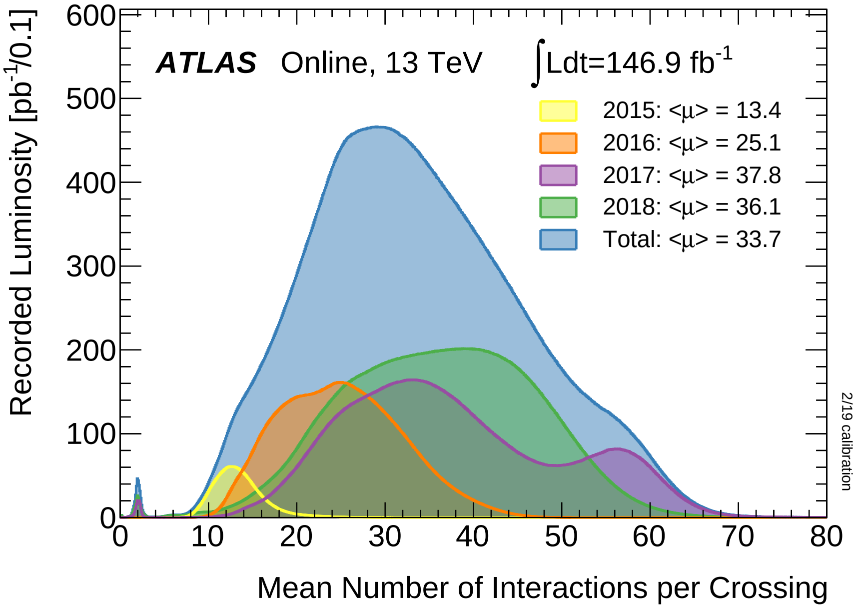

Figure 3.3: Luminosity weighted distribution of the mean number of interactions per bunch crossing, μ, for the full Run 2 pp collision data set at $\sqrt{s} = 13\,\text{TeV}$. The values of integrated luminosity and the mean μ are shown for each year of data-taking [53].

3.2 The ATLAS Detector

The ATLAS (A Toroidal LHC ApparatuS) detector is a multi-purpose experiment whose primary goal is to identify and measure the properties of the particles produced in the pp collisions at the LHC [54].

It is the largest of the four detectors at the LHC: its dimensions are 25 m in height and 44 m in length, while overall weight of the detector is approximately 7000 t. Figure 3.4 shows a sectional view of the ATLAS detector.

The ATLAS geometry, and therefore the coordinates of the particles produced in the pp collisions, can be described by a cylindrical coordinate system, as shown in Figure 3.5.

ATLAS uses a right-handed coordinate system with the origin at the interaction point, in the centre of the detector. The x-axis points from the IP to the centre of the LHC ring, the y-axis points upwards while the z-axis runs along the beam pipe. The azimuthal angle ϕ is measured around the beam axis and the polar angle, θ, is the angle from the beam axis.

The *rapidity* y of a particle with energy E and momentum p_z, in the z-direction, is defined as

$$y = \frac{1}{2} \ln \frac{E + p_z}{E - p_z} \tag{3.4}$$

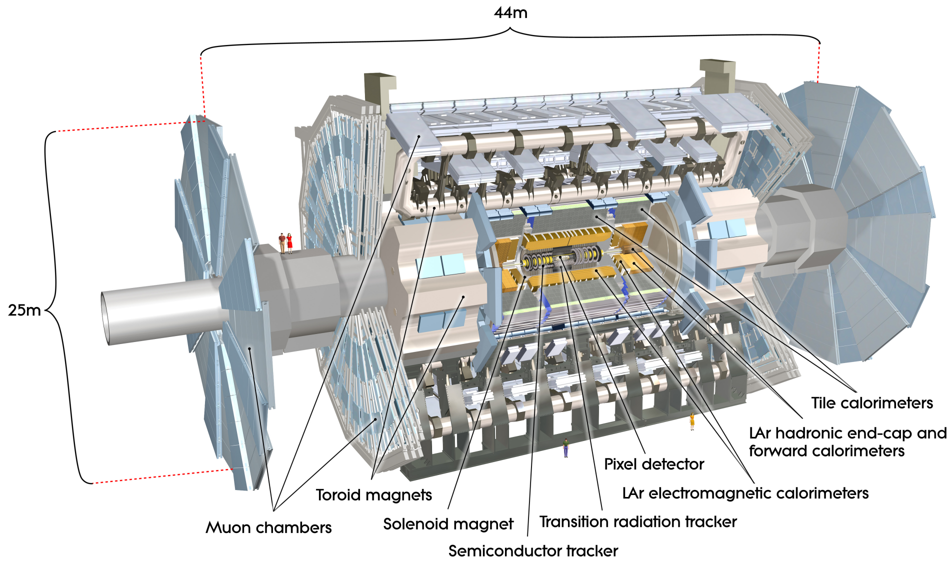

Figure 3.4: Cut-view of the ATLAS detector [55]

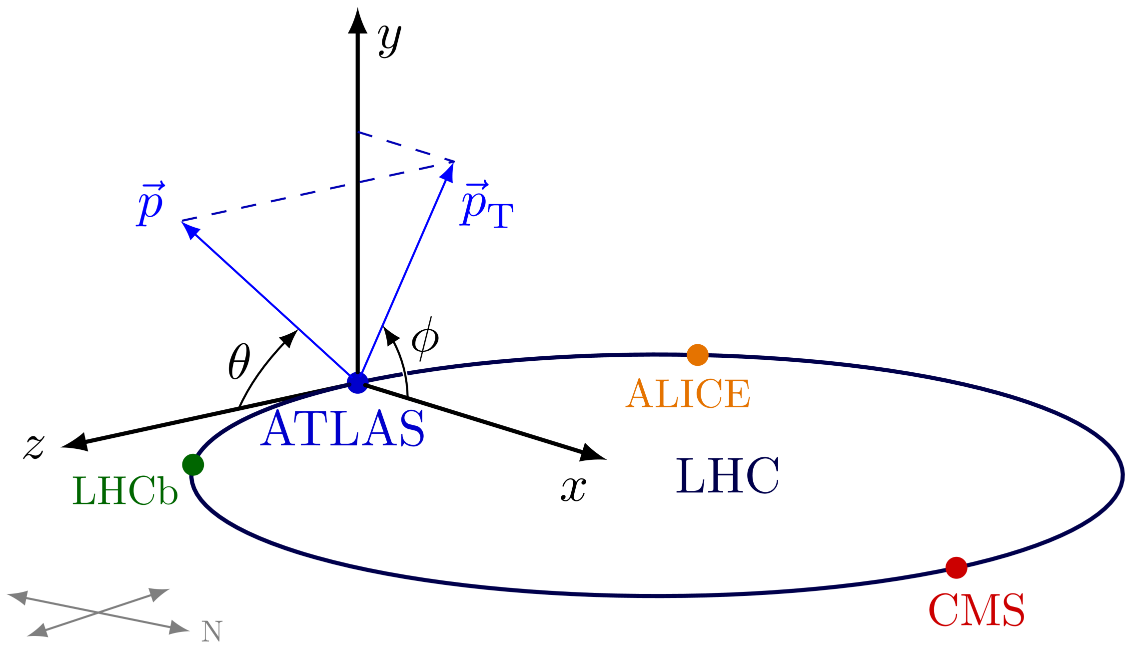

Figure 3.5: LHC ring coordinate system [56].

This is an useful observable since the differential of y, dy, is invariant under Lorentz transformation along the z-axis [54].

In case of massless particles, or in the limit of large momentum, the rapidity approximated by the *pseudorapidity*

$$\eta = -\ln\tan\left(\frac{\theta}{2}\right) = \frac{1}{2}\ln\left(\frac{\vec{p} + p_z}{\vec{p} - p_z}\right) \tag{3.5}$$

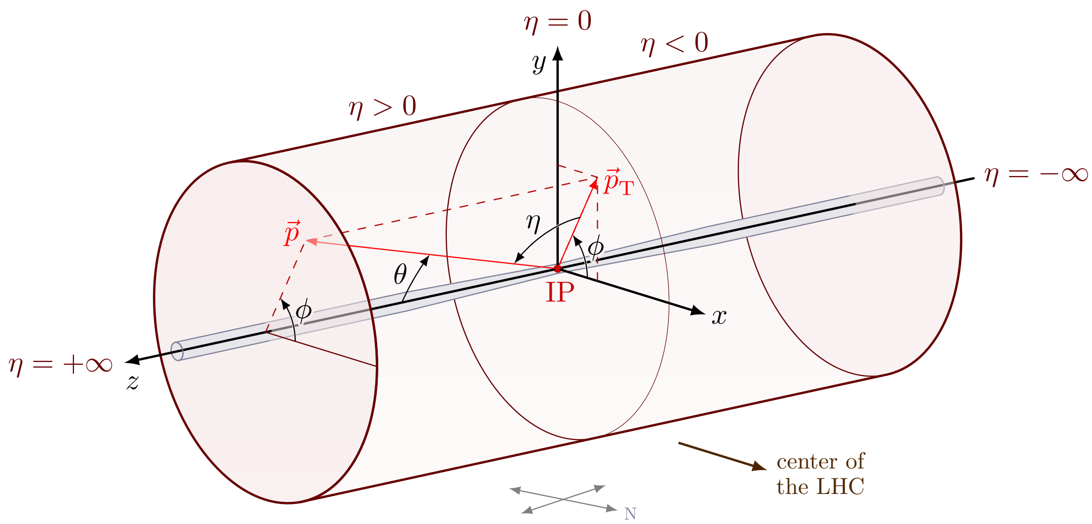

Figure 3.6: Schematic of the coordinate system and common observables used in the ATLAS Experiment. Figure adapted from Ref. [56]

.

where $\overrightarrow{p}$ is the total momentum of the particle.

The distance ΔR in the pseudorapidity-azimuthal angle plane is defined as

$$\Delta R = \sqrt{\Delta\eta^2 + \Delta\phi^2} \tag{3.6}$$

The ATLAS detector is hermetic around ϕ but not completely along θ, this is the reason why in the $x - y$ plane both the *transverse momentum* p_T and the *transverse energy* E_T are defined.

All the coordinates and the observables used in the ATLAS experiment are shown in Figure 3.6.

3.2.1 Inner Detector

The Inner Detector (ID) [57] is the closest detector to the IP. Its purpose is to measure the tracks left by charged particles produced in the collisions. The bending of the tracks, due to the presence of the magnetic field, allows for the measurement of the momentum of the particles. Figure 3.7 shows the cut-view of the ID, along with its dimensions. The inner detector is composed by four sub-detectors which are, from the innermost to the outermost: Insertable B-Layer (IBL), Pixel (PIX), Semi-Conductor Tracker (SCT) and Transition Radiation Tracker (TRT). A complete overview of the performance of the inner tracking system is given in Ref [58].

Insertable B-layer The IBL [60] is the innermost sub-detector of the ID. It was installed between Run 1 and Run 2, with the aim of maintaining and improving the

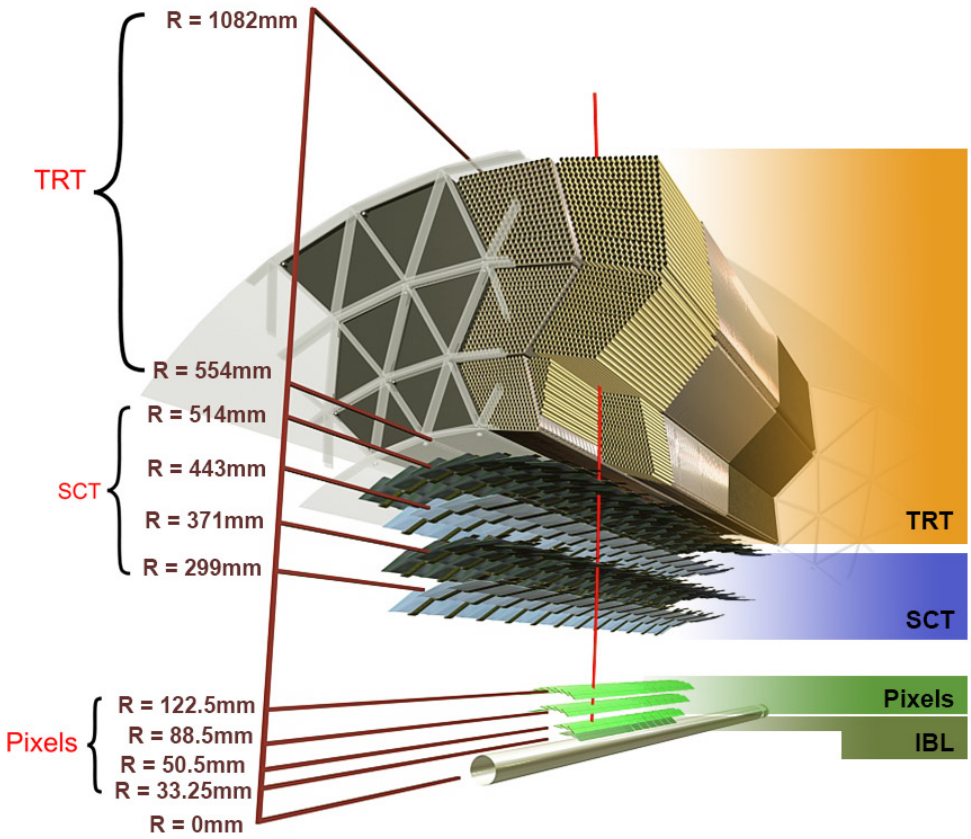

Figure 3.7: Cut-away view of the ATLAS inner detector, along with its dimensions. Figure from Ref. [59].

performance of the ATLAS detector. It can mitigate the radiation damages in the pixel detector and also improve the tracking precision in high pile-up environments. The IBL covers a pseudorapidity region of $|\eta| \leq 3$ and its spatial resolution is 10 µm in the $R-\phi$ plane and 66.5 µm in the z plane.

Pixel detector The Pixel detector [61] is composed by three layers of sensors located between $50.5 < R < 123$ mm. The sensors inside the barrel ($|\eta < 1.4$) are arranged approximately parallel to the magnetic field and the beam axis, while the sensors in each end-cap ($1.1 < |\eta| < 2.5$) are organized radially with constant azimuthal angle. In both structures, the sensors are placed such that the readout area of one module is covered by the active area of the following one. The pixel detector covers an angular range of $|\eta| \leq 2.5$ and the measured spatial resolution is between 5 and 12 mm.

Semi-Conductor Tracker The SCT [62], as the pixel detector, is organised in layers and disks. It uses silicon strips that are distributed across four layers in the barrel, located between $30 < R < 51$ mm, and nine layers in the end-caps. The SCT covers $|\eta| \leq 2.5$ and it can measure particle tracks with a precision of up to 25 µrad.

Transition Radiation Tracker The TRT [63] is located in the outermost part of the ID. It consists of a gas-filled straw tubes with a diameter of 44 mm, these tubes are the active part of the TRT and contain a mixture of different gases. The straw tubes are then immersed in a matrix of polypropylene fibres (foils in the end-cap), which is the radiator material that causes the transition radiation. In the barrel, the tubes are parallel to the beam pipe, while in the end-caps they are organised in a disk structure. The barrel region covers the range $|\eta| \leq 1$ and provides a spatial resolution of $\phi \geq 130$ µm. TRT purpose is to to provide positioning information as well as identifying charged particles. Tracks within $|\eta| \leq 2.5$ and with a $p_T > 0.4$ GeV can be reconstructed by the ID.

3.2.2 Calorimeters

Figure 3.8 shows the ATLAS calorimeter system. Its purpose is to measure the energy of the particles by reconstructing the electromagnetic and hadronic showers. Electromagnetic showers are produced by a particle that interacts primarily or exclusively via the electromagnetic force, usually a photon or electron. Hadronic showers are produced by hadrons (i.e. nucleons and other particles made of quarks), and proceed mostly via the strong nuclear force. The system is composed of two sub-detectors: the electromagnetic (ECAL) and the hadronic (HCAL) calorimeters [64]. These detectors cover a range $|\eta| < 4.9$ using a sampling technique, consisting of alternating layers of passive and active materials.

A critical point for the calorimeters is the containment of the shower, this is achieved using small radiation (X_0) and interaction (λ) length.

Electromagnetic Calorimeter The ECAL is shaped as an accordion: it uses lead absorber plates as passive material and liquid Argon (LAr) as the active material. The ionisation produced by particles in the active material is read by the electronics in the lead absorber. The ECAL is divided into a barrel part and two end-cap components, each housed in their own cryostat. The barrel calorimeter consists of two half-barrels, separated by a gap at $z = 0$, while each end-cap is divided into two coaxial wheels. The barrel region covers a pseudorapidity range of $|\eta| < 1.475$ and the end-caps cover the region $1.37 < |\eta| < 3.2$. The gap region between $1.35 < |\eta| < 1.52$ is called *crack-region* because it contains a large amount of inactive material. The barrel is radially segmented into three longitudinal layers for $|\eta| < 2.5$. The first layer, around 4-5 X_0 thick, is finely segmented in the η direction, the second layer collects most of the shower energy and the last layer is used to correct

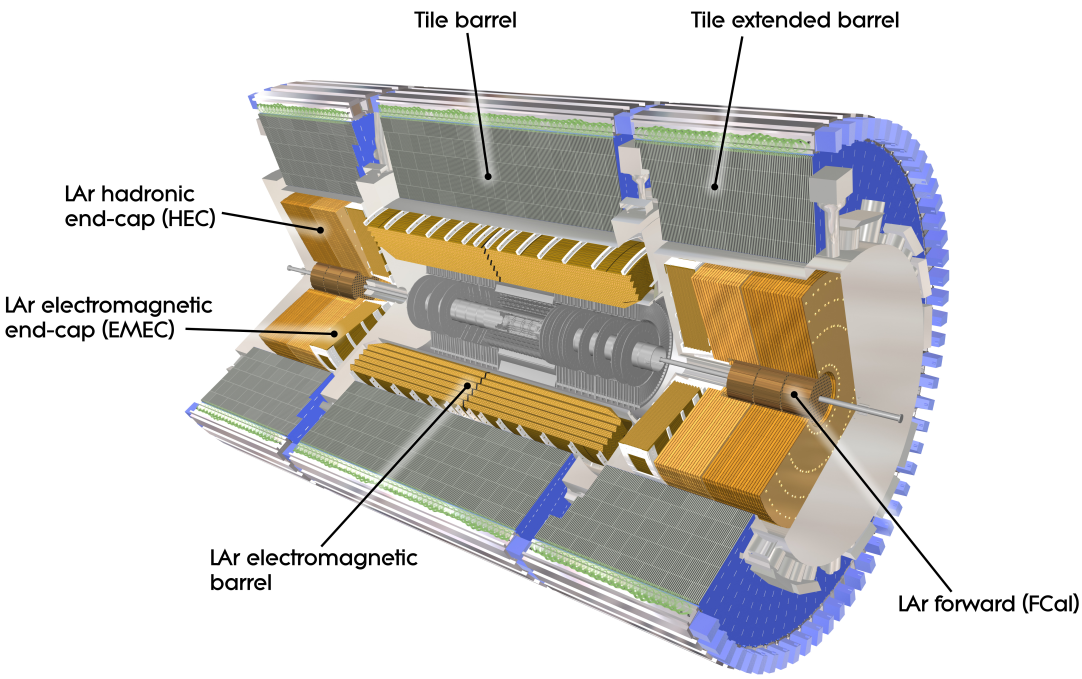

Figure 3.8: Cut-away view of the ATLAS calorimeter system [65].

for leakage behind the electromagnetic calorimeter. All layers together correspond to more than $22X_0$. To enhance the energy resolution, a thin presampler layer is placed between the cryostat and the calorimeter, covering the region $|\eta| < 1.8$. It provides the first sampling of the shower just before the electromagnetic calorimeter. The shower evolution is controlled by the radiation length X_0 [1]. This is the mean distance travelled by the incident electron before it looses $1/e$ of its initial energy via radiation and, at the same time, it is also the 7/9 of the mean free path for pair production by a high energy photon before converting into an e^+/e^- pair. For this reason it is necessary to have the ECAL as thick as possible: the total depth of the ATLAS ECAL is between $22 < X_0 < 33$ depending on the $|\eta|$ value.

The energy resolution of the ECAL was measured in test beams (with electrons) before the installation in the ATLAS cavern. The energy resolution was measured as a function of the beam energy, and it is parameterised as

$$\frac{\sigma(E)}{E} = \frac{10.1\%}{\sqrt{E(\mathrm{GeV})}} \oplus \frac{1}{E} \oplus 0.17 \tag{3.7}$$

where the first term is stochastic, the second one is related to the non-uniformity of the detector response and the third accounts for noise effects.

[1]A useful approximation is $X_0 \sim 180A/Z^2$, where A is the mass number and Z is the atomic number.

Hadronic Calorimeter The HCAL is used to detect the energy deposited by the hadronic showers initiated by the hadronic charged particles ($p, \pi^{\pm}, K^{\pm}$, etc..). It is divided into three parts: the tile calorimeter, the Hadronic End-Cap Calorimeter (HEC) and the Forward Calorimeter (FCal). The tile calorimeter is a sampling calorimeter made of steel as passive material and scintillating tiles as active material, placed around the EM calorimeter. Two sides of the scintillating tiles are read out in two separate photomultiplier tubes by wavelength-shifting fibres that allow the signal to be converted into visible light. The tile calorimeter covers a pseudorapidity region of $|\eta| < 1.7$. The HEC consists of two independent wheels located directly behind the end-cap of the ECAL and sharing the same LAr cryostats. The wheels are made of copper plates interleaved with LAr gaps. It covers a pseudorapidity region of $1.5 < |\eta| < 3.2$. The FCal is integrated into the HEC cryostats and it consists of three modules in each end-cap, it cover a pseudorapidity region of $3 < |\eta| < 4.9$. The first, made of copper, is optimised for electromagnetic measurements, while the other two, made of tungsten, mainly measure the energy of hadronic interactions. The energy resolution of the HCAL is given by

$$\frac{\sigma(E)}{E} = \frac{52\%}{\sqrt{E(\mathrm{GeV})}} \oplus \frac{1.6\mathrm{GeV}}{E} \oplus 3\% \tag{3.8}$$

The first term is related to the stochastic nature of the development of the hadronic showers, the second one is due to noise from the read-out electronics and the last one is a constant term to account for unknown effects. In the HCAL the shower evolution is dominated by the interaction length λ, which describes the travel distance of a high energy hadron before it interacts with a nucleus. To prevent a particle that is not a muon to provide signals in the muon spectrometer (phenomenon known as *punch-through*), the thickness of the HCAL should be sufficient to contain the entire hadronic shower. At $\eta = 0$ the depth of the ATLAS HCAL is 9.7λ.

3.2.3 Muon System

The Muon Spectrometer (MS) [66] is the outermost of the ATLAS sub-detectors, its structure is shown in Figure 3.9. It is based on the magnetic deflection of muon tracks in the toroidal magnets and it is instrumented with trigger and tracking chambers. The magnetic field, almost orthogonal to the muon trajectories, is generated by a system of three large air-core toroids. Each toroid consists of eight coils arranged radially and symmetrically around the beam axis. The MS is designed to provide independent measurements of the momentum of the charged particles in the pseudorapidity range $|\eta| < 2.7$ and to trigger on these particles in the region

$|\eta| < 2.4$. The momentum resolution is $\sim 10\%$ for 1TeV tracks. The system is divided into a barrel part, up to $|\eta| < 1.05$, and two end-caps. The geometry of the barrel is coaxial with three cylinders centred in the IP, called: Barrel-Inner (BI), Middle (BM) and Outer (BO), at radii of approximately 5m, 7.5 m and 10 m. The end-caps are made of three wheel-shaped structures named Endcap-Inner (EI), Middle (EM) and Outer (EO) [2] which are placed at distances of 7.4m, 14 m and 21.5 m from the IP respectively. The end-caps cover the region at high η. In both the barrel and the end-caps the magnetic field goes up to 2T. The muon spectrometer consists of 4000 individual muon chambers using four different technologies: Thin Gap Chambers (TGC), Resistive Plate Chambers (RPC), Monitored Drift Tubes (MDT) and Cathode Strip Chambers (CSC). TGC and RPC are used as triggers, while MDT and CSC are used as precision chambers.

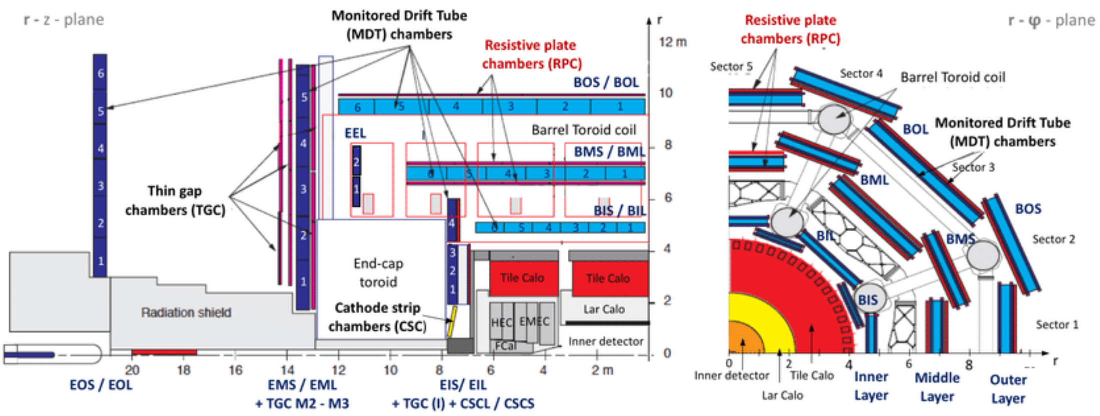

Figure 3.9: Cross-section of the ATLAS MS in the (r, z) plane (left) and in the $r - \phi$ plane (right) comprising all detector modules [67].

Precision chambers MDT are used for precision measurements of the muon tracks in a pseudorapidity range $|\eta| < 2.7$, except in the innermost end-cap layer, where their coverage is limited to $|\eta| < 2.0$. The MDT chambers consist of three to eight layers of aluminium drift tubes filled with a gas mixture of $Ar : CO_2$ (93% : 7%). The drift tubes are placed along the $r - z$ plane and they yield a resolution up to 3 µm. CSC are installed on the Small Wheel, in the $|\eta| > 2.0$ region, due to their ability to cope with a high rate of particles. CSC are multi-wire proportional chambers based on a 80% : 20% mixture of Ar and CO_2. The chambers are organised in quadruplets of planes, divided into strips, providing four independent measurements of the $|\eta|$ and ϕ coordinates. This gives a resolution of 40 µm in the bending plane

[2]Also called: Small Wheel, Big Wheel and Outer Wheel

(η) and of 5 mm in the transverse plane (ϕ). The difference in resolution between the bending and non-bending planes is due to the different readout pitch.

Trigger Chambers The MS is also used as a trigger system for the ATLAS experiment, therefore it must be fast. Two different technologies are used for this scope: RPC and TGC. Resistive Plate Chambers are used in the barrel region, in the pseudorapidity range of $|\eta| < 1.05$. In the RPC, two resistive plates are separated by 2 mm gaps filled with a gas mixture of $C_2H_2F_4 : C_4H_{10}$ (97% : 3%). Each plate is segmented into strips, which allows a preliminary measurement of the position of the hit left by a track. Two doublets of RPCs are installed in the BM and BO layers. In the larger pseudorapidity region, $1.05 < |\eta| < 2.4$, a triplet of TGC is installed on the small wheel, while two doublets are located on the big wheel, closer to the IP. The TGCs use a gas mixture of $CO_2 : n - pentane$ (55% : 45%), with anodes parallel to the MDT wires and cathode strips along the radial direction, providing a two-dimensional measurements of a hit with a time resolution of the order of 5 ns. The trigger chambers also complements the precision chambers with additional information about the track position in the bending plane (η) and one in the non-bending plane (ϕ).

3.2.4 Forward Detectors

The ATLAS forward region is covered by three smaller detectors. The data provided by these detectors are not explicitly utilized in this thesis, and as a result, they are only briefly outlined in the following. The LUCID (LUminosity measurements using Cherenkov Integrating Detector) [68] and ALFA (Absolute Luminosity For ATLAS) [69] detectors are used to to determine the luminosity delivered to ATLAS. The Zero Degree Calorimeter (ZDC) [70] is used to determine the centrality of heavy-ion collisions. AFP (ATLAS Forward Proton) [71] aims at tagging very forward protons.

3.2.5 Trigger system

The huge amount of data produced by the LHC exceeds the ATLAS readout capacity and not all the collected data is of interest for physics analyses. Therefore, a trigger system [72] is used to select the interesting events and to reduce the amount of data recorded. As Figure 3.10 shows, events are selected using a two-stage trigger system: Level 1 (L1) and High-Level Trigger (HLT).

L1 is hardware based and it selects interesting events coming from the calorimeter (L1Calo) or the muon spectrometer (L1Muon). L1Calo can identify electrons, photons or tau-leptons and it can also provide jet candidates and the missing

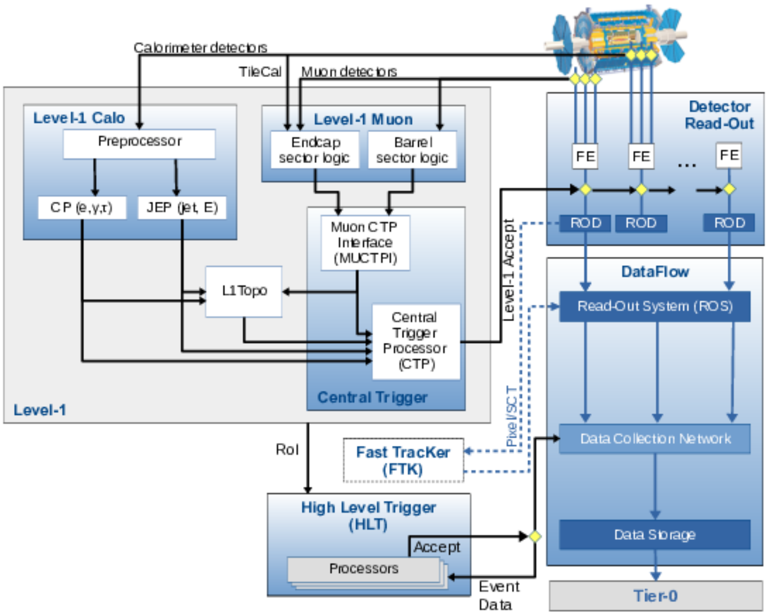

Figure 3.10: Scheme of the ATLAS trigger system in Run 2. [72] [3]

transverse momentum calculation. L1Muon can provide an estimate of the transverse momentum of the muon candidate. The combined information from the L1Calo, L1Muon and additional control subsystems (such LUCID and ZDC) is sent to the Central Trigger Processor (CTP) decides to accept or reject the events or to limit the number of accepted L1 candidates, if the read-out rate exceeds the system capability. L1 can select objects by considering event-level quantities (such total energy in the calorimeter) or by considering topological requirements (such angular distances or invariant masses). The second step in the trigger chain is the HLT, which is software based and processes events accepted by the L1 trigger. It performs a more sophisticated analysis of the events and it is largely based on the offline software Athena [73]. The output rate of the HLT system during Run 2 was 1.2kHz, with a typical disk writing rate of 1.2 $\geq$ GB/s [72].

4

Monte Carlo event Generators

In order to compare the data measured with the ATLAS detector with theoretical calculations, it is important to introduce a method to generate the expected detector response starting from a given physics process. This is done by simulating the entire chain of events, starting from the *pp* collisions and ending with the detection of stable particles within the simulated detector.

There are different steps to generate accurately the Monte Carlo simulated data, which are shown in Figure 4.1. The first step involves the calculation of the *Matrix Element* (ME) for the hard-scatter process of interest. Subsequently, the *Parton Shower* (PS) is used to simulate additional partons. Any resulting partons then undergo the process of *hadronisation*. Additionally, it is necessary to account for events that involve remnants of the collisions interacting further (underlying events) as well as pile-up. Finally, the comparison between the generated MC events and the actual data occurs after their interaction with the detector volume, in order to accurately replicate the detector response.

The previous steps allow for various levels to be defined, at which data and simulation can be compared:

- Parton-level: the process is terminated before the hadronisation, resulting in only quarks and gluons in the final state. The decay of unstable particles, such as the top quark and W-boson, is not calculated.

- Particle-level: physical particles before they interact with the detector material

- Detector-level: physical particles after passing through the detector simulation

The analysis discussed in this thesis is performed at particle-level, with the events in the data adjusted for the limited acceptance and precision of the detector (see Chapter 7).

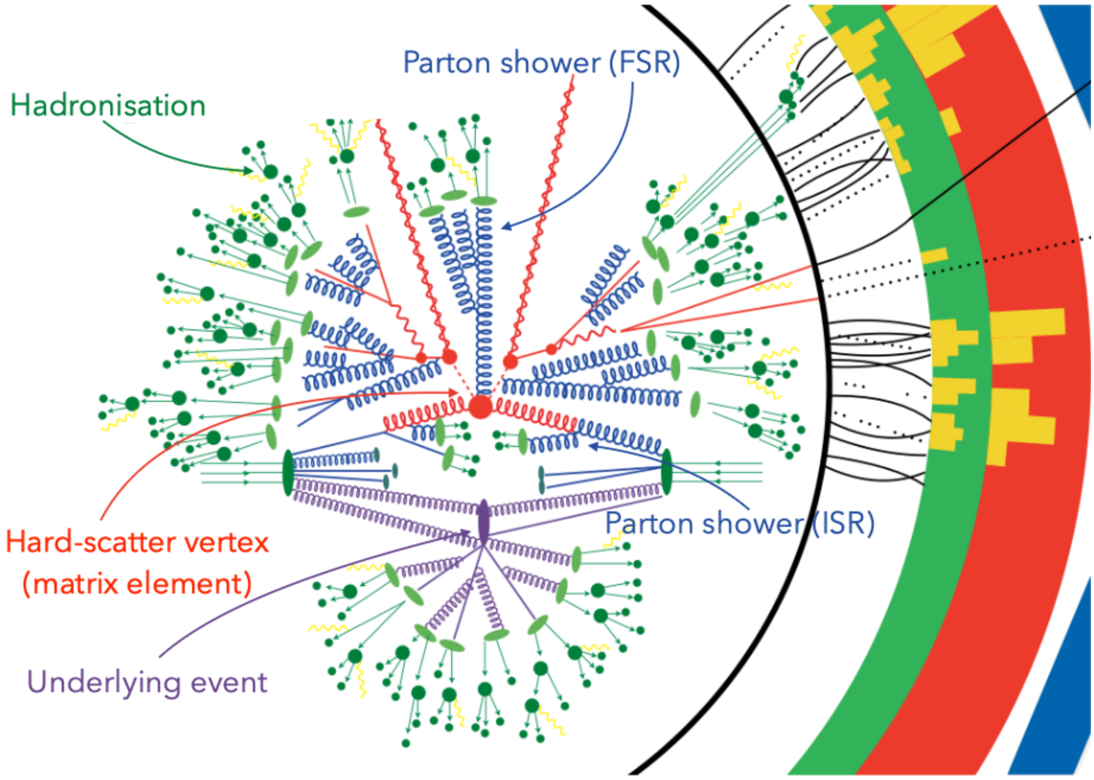

Figure 4.1: Illustrative diagram of the simulation of a proton-proton collision. Partons from the protons are shown by dark blue lines. The large dark red circle indicates the most energetic parton interaction. The emerging particles decay at the light red circles. Resulting hadrons are illustrated by light green ellipses and their decays in dark green. Photons and leptons are drawn in yellow. Additional parton-parton interactions (purple ellipsis) and the hadronisation of further proton remnants (small dark green ellipses) form the underlying event. Figure adapted from Ref. [74].

4.1 Generator building blocks

The Monte Carlo simulations rely on the concept of factorisation, which has been explained in detail in Chapter 2. In general, at high energies the partons (quark and gluons) forming the hadrons produce highly energetic outgoing partons when colliding. This hard process is computable and it is the one of the main interest in particle collisions. It is also important to know what happens at low energies to obtain a complete description of the final state. At scales at which α_S becomes large (order 1 GeV), the perturbative QCD breaks down, and phenomenological models are considered to describe the process of fragmentation of the partons. The hadronisation cannot be calculated and it has to be modelled from QCD. The transition from high to low scales is given by the parton showering. In this process, partons combine or hadronise to form colour neutral particles, which may decay further to form more stable states. The following sections will give an overview of each step that is necessary to generate a Monte Carlo sample which can be used for physics analyses.

4.1.1 Matrix Element (ME)

The starting point is to choose a hard process and generate it according to its matrix element (ME) and phase space. The hard process is typically calculated at leading order (LO), next- to-leading order (NLO). Higher orders provide higher accuracy but come with immensely increased computational complexity. This limits the choice for the available and commonly used order of the calculation.

As explained in Section 2.2, the determination of the cross section for a final state X in the pp collision involves the use of parton distribution functions and the cross sections of the partons i and j that produce X. Afterwards, the cross section is calculated by integrating the matrix element over the phase space.

A key aspect in the event simulation is the calculation of the matrix element (or scattering amplitude) $\mathcal{M}_{X+k}$, a quantity that describes the transition from an initial to a final state in a parton interaction. The matrix element is used in the definition of the partonic production cross section of a final state X, which is given by the formula

$$\hat{\sigma}_{pp\to X} = \sum_{k=0}^{\infty} \int d\Phi_{X+k} \left| \sum_{l=0}^{\infty} \mathcal{M}^{l}_{X+k}(\Phi_{X+k}) \right|^2 \tag{4.1}$$

In this equation Φ_{X+k} stands for the available phase space of the interaction resulting in a $X+k$ final state. The sum over k corresponds to the sum of the additional real emissions that can occur, and the sum over l is the sum over the number of virtual correction loops. The matrix element $\mathcal{M}_{X+k}$ is computed as the sum of the Feynman diagrams resulting in a $X+k$ final state with l loops. The numbers k, l are used to describe the order of the perturbative calculations needed for the determination of the partonic cross section. A configuration of $(k=0, l=0)$ means that the inclusive production cross section of a final state X is performed at LO, a configuration of $k=n, l=0$ describes the LO cross- section calculation for a final state of X produced in association with n jets and a more generic configuration of $(k+l \geq n)$ stands for a cross-section calculation of a final state X at $N^n nLO$, where the calculations at $N^{n-1}LO$ for $X + 1$ jet, $N^{n-2}LO$ for $X + 2$ jets,..., up to LO for $X + n$ jets are also included.

4.1.2 Parton Showers (PS)

Coloured particles can radiate gluons which can then radiate other gluons or quark-antiquark pairs, which result in *parton showers* (PS).

There are three possible QCD emissions (*splitting*) that can occur: $g \to gg$, $g \to q\bar{q}$ and $q \to gq$. To accurately simulate these additional emissions, a dedicated algorithm is required [26]. The parton shower estimates an energy scale q^2 for the final state particle if it emits a gluon, or if the gluon splits into two quarks. If the energy of the particle $q^2 < \Lambda_{QCD}$ ($\Lambda_{QCD} \sim 1\,\mathrm{GeV}$ is the cut-off scale), the quark or gluon is considered a final particle. However, if $q^2 > \Lambda$, the additional quark/gluon splitting is accepted and the parton shower continues recursively by adding emissions and splitting gluons from the resulting particles.

This principle applies to the outgoing partons. In case of showers coming from the incoming partons, among the radiated partons could be the ones from which the hard-scatter vertex is created. Then in this case the final energy q^2 of the shower is the initial energy scale of the hard-scatter interaction, and this is not compatible with the MC generators for the PS caused by the outgoing partons. For this reason, a backward evolution is being used in this case, where the shower from ISR is developed backwards by the MC generators with each of the partons before the splitting being at a higher energy.

Lastly, there is a potential risk of duplicating the partons from both the hard-process and the parton shower when combining multiple ME. To handle this different techniques have been developed, which are matching and merging.

In *matching* techniques, processes at a chosen order from the matrix element are directly matched to their parton shower equivalents and excluded from additional calculation in the parton shower. This gives exact results up to the chosen order.

In *merging*, a cut-off scale is introduced above which partons are taken from the matrix element, and below which they come from the parton shower. The result is then not accurate to a specific order but a mixture of the order used by the matrix element and all orders considered by the parton shower.

A comprehensive overview of the two methods is presented in Ref. [75].

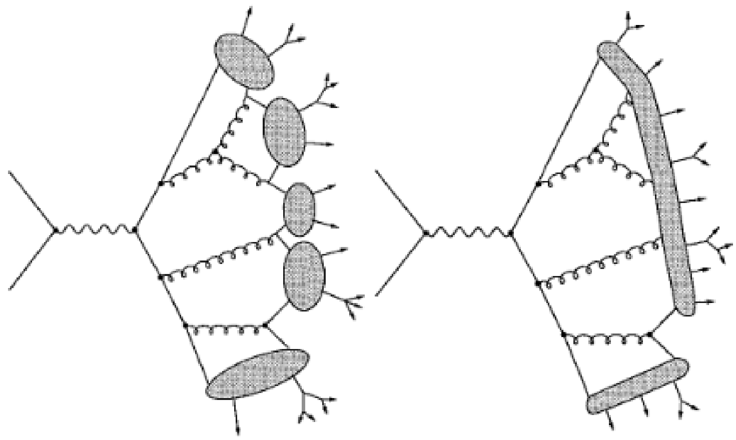

htpb

Figure 4.2: Illustrative diagram of the Lund string model (left) and the cluster model (right). Figure from Ref. [80].

4.1.3 Fragmentation and Hadronisation

The termination of a shower occurs when the radiated partons reach the hadronisation scale. At this point, the QCD calculations are no longer applicable, leading to the introduction of phenomenological models to describe the hadronisation process. There are two main models, shown in Figure 4.2, used in the event generators:

- **Lund string model**: in this model the quarks are connected by strings and gluons are represented by kinks in the strings. The energy between quarks increases as they are separated, eventually leading to the string breaking and forming $q\bar{q}$ pairs. The combined energy of the pairs is smaller than the original pair, reducing the total energy in the system until the process is no longer kinematically possible [76].
- **Cluster model**: this model is based on the concept of *pre-confinement* [77], which states that partons with the same colour charge are likely to be close in phase space after the PS, and can be grouped in colour-singlet clusters. As a first step the gluons from the PS are split into $q\bar{q}$ pairs and colour-singlet clusters are formed. Then, the clusters are divided until their invariant masses match the one of a known hadron [78, 79].

4.1.4 Underlying event

There are additional processes occurring alongside the hard process, initiated by the other partons in the protons. These underlying events and must also be incorporated into the Monte Carlo simulations of the different physics processes. Additionally, the pile-up has to be taken into account in the MC simulations. Similar to hadronisation, these interactions are described by phenomenological models that include parameters that are tuned by using the experimental data.

4.2 Overview of Monte-Carlo event-generators

The simulation of a physics process is dependent on Monte Carlo generators, which are software tools that incorporate specific algorithms for each stage of the simulation. These generators are classified into general-purpose, matrix-element, and special-purpose categories based on their functionality. The following is a brief overview of the MC generators and their respective characteristics.

4.2.1 Matrix-element generators

A matrix-element (ME) generator is specialised in providing accurate ME calculations and cannot perform the rest of the simulation steps (PS, hadronisation, etc.).

- `POWHEG-BOX` is an MC event generator able to implement NLO calculations in parton shower MC programs, known for its accuracy in handling higher-order corrections, crucial for precise theoretical predictions [81].

- `MADGRAPH5-aMC@NLO` is an MC event generator able to implement the MC@NLO method, allowing for the matching of NLO QCD calculations with event generators like `HERWIG` and `PYTHIA` for more accurate predictions. This tool is specialized in generating matrix elements for specific processes, particularly useful in scenarios involving new physics [82].

4.2.2 General-purpose generators

A general-purpose generator is able to perform a comprehensive event simulation, beginning with the matrix element calculation and extending to the hadronisation process. These generators are commonly utilized for parton showering and hadronisation, with integration with other generators specializing in ME calculations. The main general-purpose generators are outlined as follows:

- `PYTHIA` ME calculations for $2 \to n\,, (n \leq 3)$ physics processes at NLO accuracy. It is reliable during the PS simulation providing an accurate description both at high and low energy scale regimes. The PS emissions are ordered in transverse momentum (p_T). Apart from the ME and PS simulation `PYTHIA` is able to perform the hadronisation step following the Lund string model, while it can also simulate the UE interactions. It is commonly used mainly for the PS step in combination with other more accurate ME generators [83].

- `HERWIG` performs ME calculations at NLO for $2 \to 2$ physics processes. The PS emissions are ordered with respect to their opening angle and are accurately simulated due to the full spin correlation information that is included for the emitted partons. In contrast to `PYTHIA`, `HERWIG` makes use of the cluster model in the hadronisation and UE simulations [84].

- `SHERPA` performs ME calculations at LO (for ≤ 4 additional partons) and at NLO (for ≤ 2 additional partons). It uses a dedicated PS algorithm following the Catani-Seymour dipole formalism [85], a ME to PS matching algorithm based on the CKKW procedure [86] and the cluster model for the hadronisation step [87].

4.2.3 Special-purpose MC

- `EVTGEN` is specialized for the decays of heavy hadrons (those containing c-quarks and b-quarks), used on top of `PYTHIA` and `HERWIG` to improve their modeling of these hadrons [88].

- `MadSpin` is used for the modelling of heavy resonance decays after their ME has been estimated at NLO by `MADGRAPH5`. The tool takes into account the spin correlations among the decay products and it includes off-shell corrections, leading to a more accurate description of these processes [89].

4.3 Detector simulation

The particles generated with one of the simulation programs described in the previous sections are processed with the ATLAS detector simulation to obtain the detector response.

First, energy depositions of the generated particles in the sensitive volumes of the detector are emulated using the `Geant4` [90, 91] framework. The energy depositions are then transformed into electric signals and digital output signals for all of the detector components.

The Monte Carlo production chain, in a nutshell, is divided into several steps:

- **Event generation**: generation of the physics event by creating sets of particle four-momenta. In ATLAS, these sets are typically carried out by event generators. Stable or long-lived particles that decay in the detector volume are forwarded to the detector simulation. This type of MC simulated data is often referred to as particle level.

- **Detector Simulation**: next step is the simulation of the interaction of the particles with sensitive and non-sensitive detector material. In the sensitive materials, the interacting particles produce the *hits*, which are collected for further analysis in the next steps. The simulated data acquired from this procedure correspond to the reconstruction level, and are the ones used in comparisons with real data in the different physics analyses. An accurate simulation of the ATLAS detector is achieved with the `Geant4` [90, 91] framework.

- **Digitization**: the hits in the detector simulation need to be further processed to mimic the output of the detector readout. This process is different for each sub-detector. Digitization also deals, in almost all the sub-detectors, with noise modelling and event pile-up. These digital signals can then be processed by the same software used for the data and particles can be reconstructed, as described in Chapter 5.

- **Reconstruction**: consists of the local pattern recognition, reconstruction of tracks, vertices, cells and clusters in all the different sub-detectors. This step also includes the creation of the high-level objects such as particles of different identification, jets including their flavour tag or missing energy estimation.

4.4 Data and Monte Carlo Samples

This section presents the data and Monte Carlo simulated event samples used in the measurement presented in this thesis.

4.4.1 Data sample

The measurement presented in this thesis uses the full data-set collected by the ATLAS detector during the Run 2 operation. This consist of data from $p-p$ collisions at a centre-of-mass energy of 13 TeV corresponding to an integrated luminosity of 140 fb^{-1}. The partial integrated luminosities for each year of operation are reported in Table 4.1:

Year	Int. lumi. (pb^{-1})
2015	3244.5
2016	33 402.2
2017	44 630.6
2018	58 791.6
Run 2	140 068.94

Table 4.1: Integrated luminosity per year.

4.4.2 Monte Carlo simulated samples

The contribution of Standard Model processes is evaluated from Monte Carlo simulated samples [92].

The pile-up is modelled by overlaying the simulated hard-scattering event with inelastic pp events generated with `PYTHIA8.186` [93] using the `NNPDF2.3lo` set of parton distribution functions [94] and the `A3` set of tuned parameters [95].

The detector response is simulated with `Geant4` [91]. As a full simulation of the detector response is computationally expensive for some of the estimates of modelling uncertainties, the fast-simulation package AtlFast-II [92] is used, which parametrises hadronic showers in the electromagnetic and hadronic calorimeter to speed up the simulation.

The Monte Carlo events are weighted to reproduce the distribution of the average number of interactions per bunch crossing ($\langle\mu\rangle$) observed in the data. The $\langle\mu\rangle$ value in data is re-scaled by a factor of 1.03 ± 0.04 to improve agreement between data and simulation in the visible inelastic pp cross-section [96].

The signal samples are defined as the sum of the $t\bar{t}$ and the tW samples from the same combination of generators and parton showers. The signal samples are discussed in the paragraphs below and summarised in Table 4.2.

Nominal signal sample

$t\bar{t}$ production The production of $t\bar{t}$ events was modelled using the `POWHEGBOXv2` [81, 97, 98] generator, which provided matrix elements at NLO in the strong coupling constant α_S, and the `NNPDF3.0nlo` [99] parton distribution function. The h_{damp} parameter, which controls the matching in `POWHEG` and effectively regulates the high-p_T radiation against which the $t\bar{t}$ system recoils, was set to $1.5\, m_t$ [100]. The functional form of the renormalisation and factorisation scales was set to the default scale $\sqrt{m_t^2 + p_T^2}$. The events were interfaced with `PYTHIA8.230` [101] for the parton shower and hadronisation, using the `A14` set of tuned parameters [102] and the

NNPDF2.3lo set of PDFs [94]. The decays of bottom and charm hadrons were simulated using the EVTGEN1.6.0 program [88].

The $t\bar{t}$ sample was normalised to the cross-section prediction at NNLO in QCD including the resummation of NNLL soft-gluon terms calculated using TOPpp2.0 [103–109].

For pp collisions at a centre-of-mass energy of $\sqrt{s} = 13$ TeV, this cross-section corresponds to $\sigma(t\bar{t})_{\text{NNLO+NNLL}} = 832^{+41}_{-51}$ pb using a top-quark mass of $m_t = 172.5$ GeV.

tW **production** As discussed in Chapter 2, there are different treatments for the interference, corresponding to different Monte Carlo samples that can be used for single-top production. The Diagram Removal (DR) scheme is the one nominally used by most ATLAS analyses, and is also referred to as the *nominal* signal sample in this thesis.

Single-top tW associated production was modelled using the POWHEGBOXv2 [81, 98, 110, 111] generator, which provided matrix elements at NLO in the strong coupling constant α_S in the five-flavour scheme [1] with the NNPDF3.0nlo [99] PDF set. The functional form of the renormalisation and factorisation scales was set to the default scale $\sqrt{m_t^2 + p_T^2}$. The Diagram Removal scheme [36] was employed to handle the interference with $t\bar{t}$ production [100]. The events were interfaced with PYTHIA8.230 [101] using the A14 tune [102] and the NNPDF2.3lo PDF set. The decays of bottom and charm hadrons were simulated using the EVTGEN1.6.0 program [88]. The inclusive cross-section was corrected to the theory prediction calculated at NLO in QCD with NNLL soft-gluon corrections [112, 113]. For pp collisions at a centre-of-mass energy of $\sqrt{s} = 13$ TeV, this cross-section corresponds to $\sigma(tW)_{\text{NLO+NNLL}} = 71.7 \pm 3.8$ pb, using a top-quark mass of $m_t = 172.5$ GeV.

Another signal sample is considered for tW, which is the PH+PY8 (DS). It similar to the nominal PH+PY8 sample but using the diagram subtraction scheme [36, 100]. Combined with the nominal $t\bar{t}$ sample, it is presented in legends and tables as PH+PY8 (DS).

Process	@c@Event Generating Program (GEN)	GEN PDF accuracy	PS	PS Tune	Total-cross section accuracy
$t\bar{t}$	POWHEGBOXv2	NLO	PYTHIA8.230	A14	NNLO + NNLL
tW	POWHEGBOXv2	NLO	PYTHIA 8.230	A 14	NLO + NNLL

Table 4.2: Software setup used to generate simulated events for the Standard Model signal.

[1] Consist in a consistently massless treatment of the b-quark, which can therefore be found in both initial and final states.

4.4.3 Background samples

The background samples used in the analysis are discussed below and summarised in Table 4.3. The dominant background are the W-jets events. Other backgrounds are grouped in categories. In the plots and tables *other top* consists of s-channel and t-channel single-top production. The Z+jets and diboson events are named *Other V/VV* in the following plots and tables.

W+jets and Z+jets production The production of V+jets was simulated with the `SHERPA2.2.11` [114] generator. In this set-up, NLO-accurate matrix elements for up to two partons, and LO-accurate matrix elements for up to five partons were calculated with the `Comix` [115] and `OPENLOOPS` [116–118] libraries. The default `SHERPA` parton shower [119] based on Catani-Seymour dipole factorisation and the cluster hadronisation model [120] were used. They employed the dedicated set of tuned parameters developed by the `SHERPA` authors and the Hessian `NNPDF3.0nnlo` PDF set [99]. The NLO matrix elements for a given jet multiplicity were matched to the parton shower (PS) using a colour-exact variant of the `MC@NLO` algorithm [121]. Different jet multiplicities were then merged into an inclusive sample using an improved CKKW matching procedure [86, 122] which was extended to NLO accuracy using the `MEPSatNLO` prescription [123]. The merging threshold was set to 20 GeV. Electroweak virtual corrections are included in the `2.2.11` configuration, and are available as an alternative generator weight based on the NLO EW_{virt} approach [124, 125].

The V+jets samples were normalised to a next-to-next-to-leading-order (NNLO) prediction [126].

Diboson production Samples of diboson final states (VV) were simulated with the `SHERPA2.2.1` or `2.2.2` [114] generator depending on the process, including off-shell effects and Higgs boson contributions, where appropriate. Fully leptonic final states and semileptonic final states, where one boson decays leptonically and the other hadronically, were generated using matrix elements at NLO accuracy in QCD for up to one additional parton and at LO accuracy for up to three additional parton emissions. Samples for the loop-induced processes $gg \to VV$ were generated using LO-accurate matrix elements for up to one additional parton emission for both the cases of fully leptonic and semileptonic final states. The matrix element calculations were matched and merged with the `SHERPA` parton shower based on Catani-Seymour dipole factorisation [115, 119] using the `MEPS@NLO` prescription [86, 121–123]. The virtual QCD corrections were provided by the `OPENLOOPS` library

[116–118]. The NNPDF3.0nnlo set of PDFs was used [99], along with the dedicated set of tuned parton-shower parameters developed by the SHERPA authors.

Other single top production Single-top t-channel production was modelled using the POWHEGBOXv2 [81, 98, 111, 127] generator at NLO in QCD using the four-flavour scheme and the corresponding NNPDF3.0nlo set of PDFs [99]. The events were interfaced with PYTHIA8.230 [101] using the A14 tune [102] and the NNPDF2.3lo set of PDFs [94]. Single-top s-channel production was modelled using the POWHEGBOXv2 [81, 98, 111, 128] generator at NLO in QCD in the five-flavour scheme with the NNPDF3.0nlo [99] parton distribution function set. The events were interfaced with PYTHIA8.230 [101] using the A14 tune [102] and the NNPDF2.3lo PDF set.

ttV **production** The production of ttV events was modelled using the MGNLO2.3.3 [82] generator, which provided matrix elements at NLO in the strong coupling constant α_S with the NNPDF3.0nlo [99] PDF. The functional form of the renormalisation and factorisation scales was set to the default of $0.5 \times \sum_i \sqrt{m_i^2 + p_{\mathrm{T},i}^2}$, where the sum runs over all the particles generated from the matrix element calculation. Top quarks were decayed at LO using MADSPIN [89, 129] to preserve spin correlations. The events were interfaced with PYTHIA8.210 [101] for the parton shower and hadronisation, using the A14 set of tuned parameters [102] and the NNPDF2.3lo [99] PDF set. The decays of bottom and charm hadrons were simulated using the EVTGEN1.2.0 program [88].

ttH **production** The production of ttH events was modelled using the POWHEGBOXv2 [81, 97, 98, 111, 130] generator at NLO with the NNPDF3.0nlo [99] PDF set. The events were interfaced to PYTHIA8.230 [101] using the A14 tune [102] and the NNPDF2.3lo [99] PDF set. The decays of bottom and charm hadrons were performed by EVTGEN1.6.0 [88].

Process	@c@Event Generating Program (GEN)	GEN PDF accuracy	PS	PS Tune	Total-cross section accuracy
V + jets	SHERPA 2.2.11	NLO	SHERPA	SHERPA	NLO
VV	SHERPA 2.2.1 & 2.2.2	NLO	SHERPA	SHERPA	NLO
Othertop	POWHEGBOXv2	NLO	PYTHIA8.230	A14	NLO
ttV	MGNLO 2.3.3	NLO	PYTHIA8.230	A14	NLO
ttH	POWHEGBOXv2	NLO	PYTHIA8.230	A14	NLO

Table 4.3: Software setup used to generate simulated events for the Standard Model backgrounds.

5
Object Reconstruction

Particles generated by the collision travel through the ATLAS detector interacting with the detector material (see Chapter 3). Different particles leave distinct signatures in various sub-detectors, as illustrated in Figure 5.1.

Electrons (depicted in yellow) create signals in the ID and produce showers in the electromagnetic calorimeter, while photons (shown in green) only produce showers in the electromagnetic calorimeter. Muons (in orange), as minimum-ionizing particles (MIP), can traverse the entire detector and leave only traces in the inner detector and (small ones) in the calorimeters. They are the only charged SM particles that commonly reach the Muon Spectrometer. Neutrinos (represented by dashed white lines) do not leave any signals in the sub-detectors, their presence can only be deduced from observing momentum imbalance in the event. Charged hadrons (in red) generate signals in the ID, electromagnetic calorimeter and in the hadronic calorimeter. Conversely, neutral hadrons (depicted in red) pass through the detector without leaving a track and then shower in the calorimeters.

The deposits left by these particles are collected, transformed into electronic signals, and digitized for subsequent analysis. *Object reconstruction* is the procedure that allows the conversion of digital electronic signals into the characteristics of the particles involved in the interactions. These reconstructed objects are used to select events of interest for the physics analyses.

The following sections provide a description of how the detector signatures are reconstructed as physics objects.

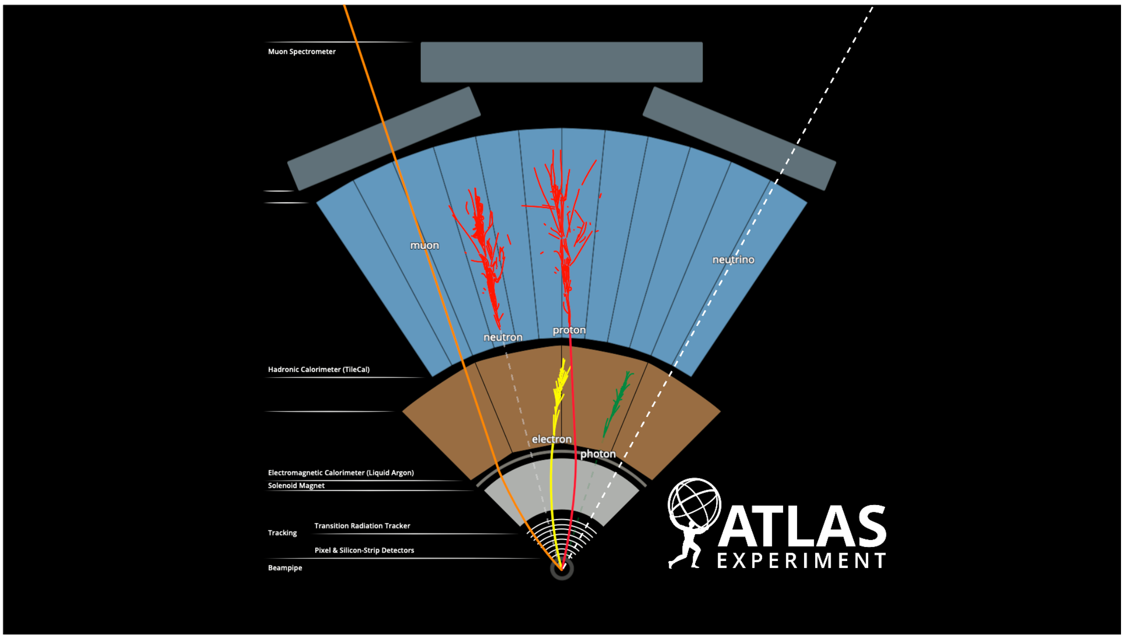

Figure 5.1: How ATLAS detects particles: diagram of particle paths in the detector [131].

5.1 Charged particles in the Inner Detector

The trajectories of the charged particles, or *tracks*, are one of the fundamental ingredients to reconstruct the objects in the ATLAS detector. The tracks are reconstructed using the Inner Detector. Since it is immersed in a magnetic field, the particles have a helicoidal trajectory inside the detector. The trajectory with respect to the primary vertex position is described by a curvilinear parametrization using five parameters, shown in Figure 5.2.

- Transverse impact parameter d_0: distance of closest approach in the transverse plane between a track and the beamline
- Longitudinal impact parameter z_0: z-coordinate of the space point at which d_0 is determined
- θ and ϕ: polar and azimuthal angle at the perigee, defined in Section 3.2
- Charge over momentum q/p: defines orientation and curvature

The foundation of the tracking process is the detection of *hits* generated by particles in the Pixel and SCT detectors, provided that the energy deposit, in the silicon sensors or drift tubes, exceeds a fixed threshold. The hits in neighboring cells are combined into *clusters* to create *space-points*. These space points are built

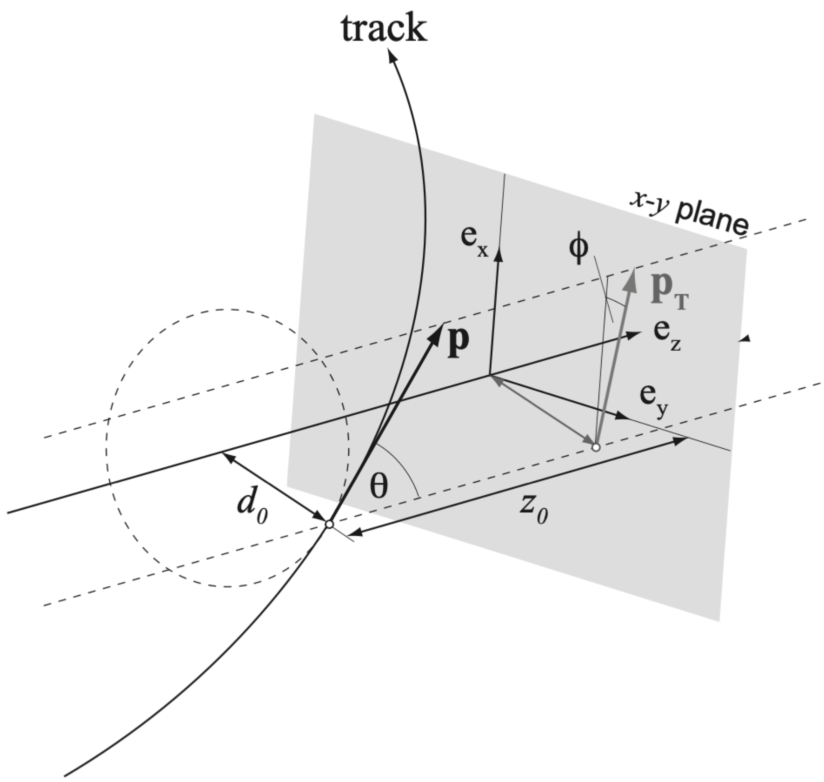

Figure 5.2: Scheme of the parameters used to construct the tracks in the Inner Detector [132].

using the centre of gravity of the energy deposits in the hits. A group of three space-points form the initial *track seeds*. These track seeds are then extended into *track candidates* by incorporating hits from other layers of the inner detector, excluding the TRT, with the assistance of a Kalman filter [133]. The track candidates may share some of the hits, and to resolve any ambiguities, a quality score is used in an ambiguity resolution algorithm. The latter takes into account several criteria, such as the number of ID layers with a hit, the χ^2-squared value and the p_T of the track candidate, as extensively explained in the reference [132]. Track candidates that do not meet the selection criteria are rejected during the ambiguity resolution process.

The final step involves extrapolating the tracks to the TRT and combining them to form the ultimate reconstructed objects. The complete reconstruction procedure is thoroughly described in Reference [134]. A visual representation of the tracking procedure can be seen in Figure 5.3.

There are multiple proton-proton collisions per bunch-crossing, as mentioned in Chapter 3. However, only one collision is of interest, to identify it, the *vertex* must be reconstructed. The vertex reconstruction is based on reconstructed tracks

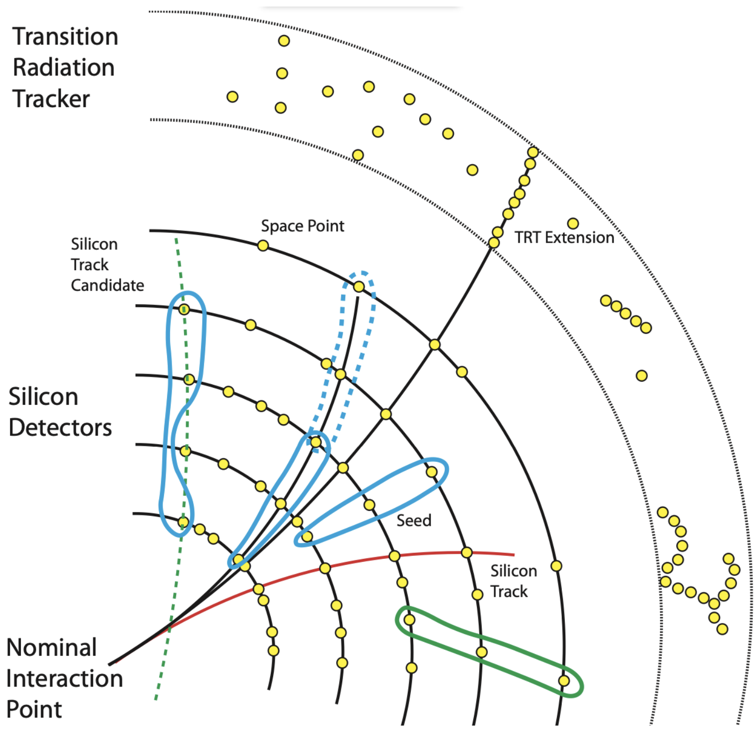

Figure 5.3: Schematic representation of the tracking procedure. Figure adapted from [135].

that are compatible with the one originating from the interaction region and fulfill certain quality criteria. By identifying peaks in the distribution of these tracks along the z-axis, *seed-vertices* are constructed. For each seed-vertex, an exact vertex position is calculated using a dedicated vertex fitting algorithm. Tracks that are not compatible with a fitted vertex are used in the reconstruction of other vertices.

Primary vertices are those directly at the beamline where proton-proton interactions occurred. Typically, there is more than one primary vertex per bunch crossing. The *hard-scatter vertex* is the primary vertex with the highest sum of squared transverse momenta of the associated tracks. *Secondary vertices* arise from particles with a long lifetime, such as b-hadrons, which travel before decaying, causing a displacement between the vertex position and the beamline.

5.2 Electrons and photons

Electrons and photons are reconstructed from energy deposits in the electromagnetic calorimeter with a matching (for e^-) or a non-matching track (for γ). As they are reconstructed similarly, they are discussed together. A schematic representation of the reconstruction process is shown in Figure 5.4 and discussed in the following.

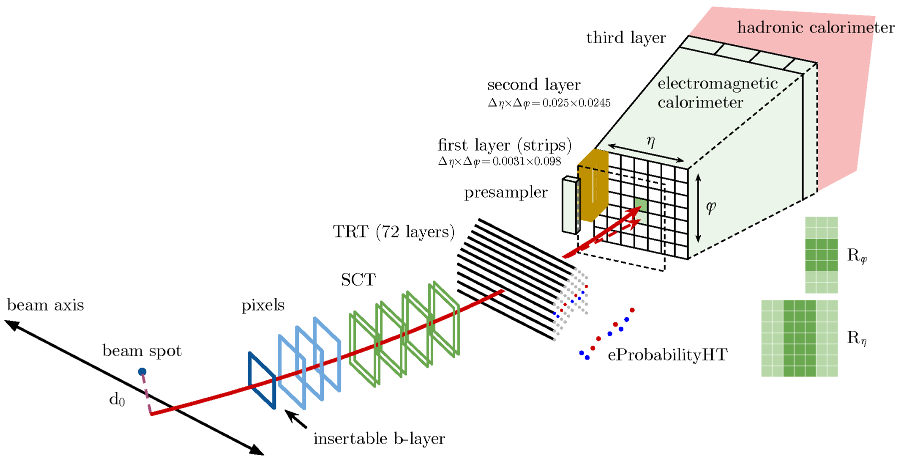

Figure 5.4: Schematic view of the electron reconstruction and identification. Picture from [136].

The reconstruction process starts with the creation of *topoclusters*, which are clusters of energy deposits in the electromagnetic calorimeter and hadronic calorimeter that are topologically connected. These clusters are dynamic and adjusted in size based on the energy they contain, allowing for the recovery of energy from bremsstrahlung photons or electrons resulting from photon conversions ($\gamma \rightarrow e^+e^-$). Once the topoclusters are defined, they are matched to ID tracks which are re-fitted to accommodate the bremsstrahlung effect. Additionally, efforts are made to reconstruct vertices where photon conversions have occurred (such as those involving two oppositely charged tracks).

Topoclusters that are matched to tracks are identified as electrons, those with matched conversion vertices are classified as converted photons, and those with neither are categorized as unconverted photons.

After the formation of topoclusters, it is necessary to distinguish between *prompt leptons*, which originate from the hard scatter or the decays of heavy resonances (such as the Higgs, Z, and W-bosons), and background sources. The background consists of misidentified jets as electrons or photons, non-prompt decays from b- or c-quarks, or cases where electrons are reconstructed as photons or vice versa.

In order to distinguish between signal and background, two additional steps are implemented:

- **Identification**: the identifications of prompt electrons is accomplished by constructing a likelihood discriminant using measurements from the ID, calorimeter, and their combination. Three sets of identification selection requirements are defined correspondingly to increasingly restrictive selections:

`Loose`, `Medium` and `Tight`. These selections result in progressively reduced background, but also a decrease in signal acceptance. These identification requirements are valid in the pseudorapidity range $|\eta| < 2.5$.

- **Isolation**: to further suppress the *non-prompt* objects from heavy flavour decays or the mis-identification of light hadrons as electrons, isolation criteria are applied. These criteria are applied to tracks and energy clusters in the proximity of the electron candidate. The requirements are based on topoclusters of energy deposits in the calorimeter and reconstructed tracks in a direction similar to that of the photon candidate. Both calorimeter-based and track-based isolation variables are utilized to ensure electron isolation. The metric employed is based on the variable E_T^{cone20}, which represents the sum of the missing transverse energy of clusters within a $\Delta R = 0.2$ cone, excluding the clusters associated with the candidate itself.

Differences in reconstruction, identification and isolation between the simulated objects and the collected data lead to differences in reconstruction efficiency. To correct for these disparities *Scale Factors* (SF) are applied. These are calculated from $Z \to e^+e^-$ as well as from $J/\psi \to e^+e^-$ events and are applied as per-event weight. The efficiencies are shown in Figure 5.5.

The electron used in this analysis use the `Tight` working point for both the identification and isolation. Photons are not specifically selected in the measurement. For electrons there is also a requirement of $p_T > 10\,\text{GeV}$ and $|\eta| < 2.47$.

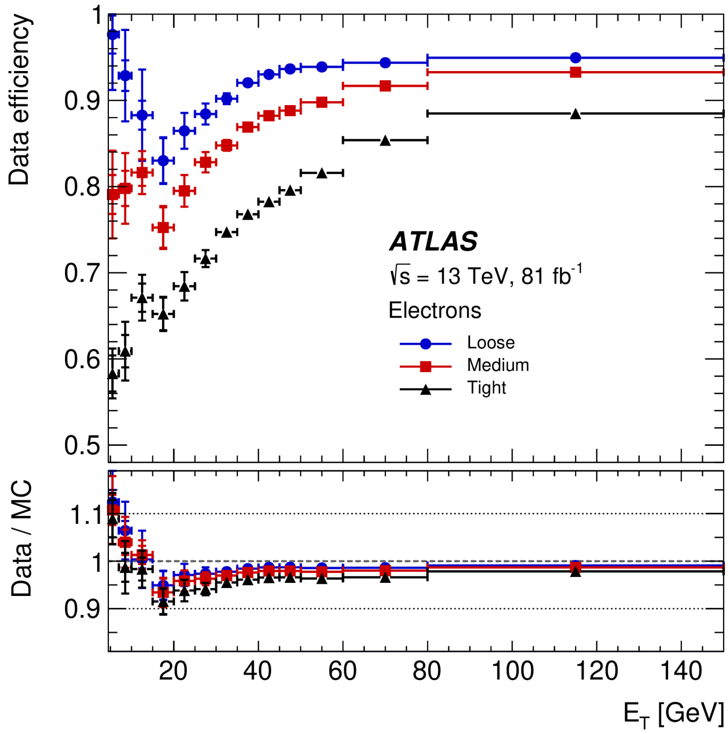

Figure 5.5: Efficiency for the electron identification at different working points, as a function of the transverse energy E_T. The inner (outer) uncertainty bars give the statistical (total) uncertainties. Picture from [137].

5.3 Muons

The primary signature utilized for muon reconstruction is that of a *Minimum Ionizing Particle* (MIP), which can be identified by the presence of a track in the Muon Spectrometer and very low energy deposits in the calorimeters. The global muon reconstruction process relies on informations from the inner detector and muon spectrometer tracking detectors, as well as the calorimeters.

The track reconstruction in the inner detector follows the procedure described in Section 5.1. The track reconstruction in the muon spectrometer begins with the identification of *muon segments*, which are straight lines in the segment of the muon spectrometer. These muon segments from multiple stations are combined using a loose constraint based on the position of the IP and a parabolic trajectory, which provides an initial approximation of the muons path in the bending plane. Subsequently, a χ^2 fit of the muon trajectory is performed, taking into account potential misalignment effects and interactions with detector material. Once this preliminary muon track is obtained, the association of muon spectrometer hits with the track is verified, removing outlier hits and including those that were not initially used. There are five main strategies for muon reconstruction, each corresponding to a specific type of muon. The muons used in the analysis presented in this thesis are *Combined (CB)* muons, in this case muons are reconstructed by matching muon system tracks to ID tracks. More detailed informations on the other types of muons can be found in Ref. [138]

Two more steps are needed, as for electrons and photons, to distinguish between signal and background:

- **Identification**: after the reconstruction, high-quality muon candidates used for physics analyses are selected based on specific criteria related to the number of hits in various ID sub-detectors and muon spectrometer stations, track fit properties, and variables assessing the compatibility of individual measurements in the two detector systems. Three standard selection Working Points are designed: `Loose`, `Medium` and `Tight`. The `Loose` selection WP is optimised for maximal efficiency. The `Medium` WP provides an efficiency and purity suitable for a wide range of analyses, while keeping the systematic uncertainties in the prompt-muon efficiency and background rejection small. Finally, the `Tight` selection WP provides the highest level of hadron rejection.
- **Isolation**: similar to electrons and photons, the activity close to the reconstructed muons is taken into account from the ID, from the calorimeters, or from both.

The different reconstruction efficiencies between data and simulation are investigated in $Z \to \mu^+\mu^-$ and $J/\psi \to \mu^+\mu^-$events and corrected by applying different event weights to simulated events. Figure 5.6 displays the selection efficiency as a function of the transverse momentum of the muon for the three WPs.

In the measurement performed in this thesis, the muons are of the combined type and the `Tight` working point is used for both isolation and identification. There is also a requirement of $p_T > 10\text{GeV}$ and $|\eta| < 2.5$.

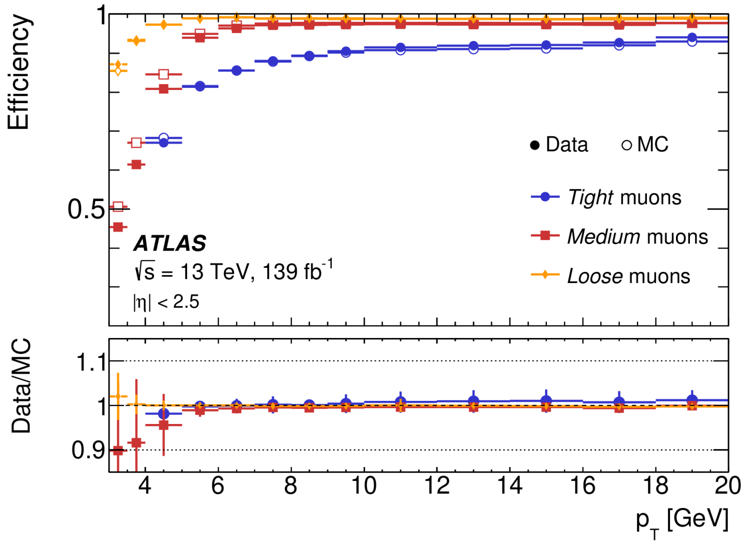

Figure 5.6: Muon reconstruction and identification efficiencies for the Loose, Medium, and Tight criteria. The plot shows the efficiencies measured in $J/\psi \rightarrow \mu^+\mu^-$ events as function of p_T. The predicted efficiencies are depicted as open markers, while filled markers illustrate the result of the measurement in collision data. When not negligible, the statistical uncertainty in the efficiency measurement is indicated by the error bars. The panel at the bottom shows the ratio of the measured to predicted efficiencies, with statistical and systematic uncertainties. Picture from [138].

5.4 Jets

Hadronic jets are the final product of the hadronisation of a quark or a gluon and are composed of a multitude of collimated hadrons. Given that, their corresponding signature has to be found in both the inner detector and the calorimeter System. The identification of a jet starts in the calorimeter, from the identification of clusters of localised energy deposits.

5.4.1 Jet identification and reconstruction

The high granularity of the ATLAS calorimeter allows the signals left by the particles interacting with the sensitive material of the detector to be combined into topoclusters (described in section 5.2). *Particle-flow* objects [139, 140] are the basic ingredient for the formation of jets. They are constituted of tracks and calorimeter clusters. Their reconstruction algorithm is described below and is extensively documented in Ref. [141].

Particle-flow objects are reconstructed starting from the topological clustering of the calorimeter cells following a "$4-2-0$" topocluster reconstruction algorithm [142] similarly to the electrons and photons reconstruction as described in Section

5.2. If the resulting topoclusters present two or more maxima, they are split into smaller topoclusters. Finally, the four-vector of the topocluster is constructed, assuming zero mass, using the direction with respect to the primary vertex and the sum of the energy in the cells making up the cluster.

A number of algorithms have been developed and studied to complete the reconstruction of the topoclusters that will constitute the jet. The most commonly used in ATLAS and in the analysis presented in this thesis is the anti-k_T jet clustering algorithm, presented in [143], which is an infrared and co-linear safe algorithm [1]. It is based on the evaluation of the distance metrics:

$$d_{ij} := min\left(p_{T,i}^{2m}, p_{T,j}^{2m}\right)\frac{\Delta R_i j^2}{R^2} \tag{5.1}$$

$$d_{iB} := \frac{1}{p_{T,i}^2} \tag{5.2}$$

where $d_{i,j}$ measures the distance between two constituents, while $d_{i,B}$ represents the distance between a constituent and the beam. The parameter R is called as the jet radius, which is the only free parameter in the represents the distance between constituents i and j in the in the rapidity-azimuth plane, i.e. $\Delta R^2 = (\eta_i - \eta_j)^2 + (\phi_i - \phi_j)^2$.

The parameter m is an integer that defines different types of algorithms with $m = 1$ representing the k_t *algorithm* [144]; $m = 0$ representing the *Cambridge/Aachen* algorithm [**Yu.L. Dokshitzer_1997**]; and $m = -1$ defining the *anti-k_t algorithm* [143].

This algorithm is appplied to the constituents with a defined four momenta, such as topo-clusters or particles. This constituents can be seen as a hadron with a four-momentum given by the sum of the four-momenta of the constituents. The procedure of finding jets goes as follows:

- Fix a value for R in the denominator of Equation 5.1 and compute the distance d_{ij} each constituent i and j using their corresponding p_T values. Evaluate d_{iB} for each constituent i as well.

- Find the smallest $d_i j$,i.e., $\min(d_{ij})$ and the smallest d_{iB} , i.e., $\min(d_{iB})$ among all combinations obtained from the previous step, and proceed as follows:

[1] Collinear and infrared safe, which means that the algorithm should not be sensitive to collinear splitting of the partons and to the extra radiation of arbitrarily soft particles.

- If $\min(d_{ij}) < \min(d_{iB})$: combine the two entities i and j to form a new constituent. Remove the entities i and j from the procedure and add the new constituent.
- If $\min(d_{ij}) > \min(d_{iB})$: recognise the constituent i as a jet and remove it from the iteration.

- Repeat the procedure until no constituents are left. The procedure so performed results into almost perfect conical jets.

The jets used in this thesis are clustered using *anti-k_T* algorithm with $R = 0.4$.

Furthermore, if high-energetic entities have $\Delta R_i j > 2R$, they are reconstructed as two individual, conic jets. For $R < \Delta R_i j < 2R$, the overlap is divided between the two jets. Constituents with $\Delta R_i j < R$ are merged into a single high-energetic jet.

Matching particle- and detector-level jets within $\Delta R_i j < 0.3$ in dijet events allows the particle- and detector-level jet energy (E_{part} and E_{det}, respectively) to be put in relation. The central value of the E_{det}/E_{part} distribution is called the *Jet Energy Scale* (JES), its width the *Jet Energy Resolution* (JER).

5.4.2 Jet Energy Scale (JES) and Jet Energy Resolution (JER) calibration

Successively, multiple calibration steps are carried out to correct differences in the jet energy between detector- and particle-level.

The first set of corrections aims to reduce the p_T of a jet taking into account the presence of pile-up interactions, exploiting the average p_T-density in the $y - \phi$ plane and the actual area of a jet. A residual effect correction, dependent on the number of interactions per bunch crossing and the number of primary vertices, is applied to the jet transverse momentum.

At a second stage, an absolute correction of the JES and the jet-η attempts to match the four-momentum of the reconstructed jet with the one of the particles originating the shower. This correction is derived by simulated events, using reconstructed jets after the origin and pileup corrections, matching the truth jet to the reconstructed one if the first is within a $\Delta R = 0.3$ cone centred in the second one. For such jets the energy response, defined as the ratio E_{reco}/E_{truth}, is computed and determined in bins of E_{truth}, then is inverted and applied to the EM scale jets. A similar correction is applied to the reconstructed value of η, parametrising the difference between η_{truth} and η_{reco} as a function of η and E_{truth}, this correction has a significant effect for jets in the transition region between the barrel and the endcap, and between the endcap and forward calorimeter.

After the previous corrections have been applied, the difference of p_T between truth and reconstructed jets can vary, depending on many aspects like the jet energy distribution, the development of the shower along the calorimeter depth and the particle that initiates the shower. A set of sequential corrections, named Global Sequential Calibration are derived using different observables and applying the relative correction as a function of the truth p_T and η of the jet.

The last step of the jet calibration consists in applying correction factors derived in data events, measuring well known processes. These in-situ calibrations are divided in two classes, the first corrects the p_T response of jets in the forward region ($0.8 < |\eta| < 4.5$), to that of well-measured events in which two central jets ($|\eta| < 0.8$) are back-to-back in ϕ. A second step consists in balancing the p_T of central jets to a reference object which provides the correct p_T scale; for this purpose $Z \to e^+e^-$ or $Z \to \mu^+\mu^-$ are reference objects for the p_T up to 950 GeV, while the balance to a set of low-p_T jets allows for a correction up to 2 TeV.

A scheme of the steps for the jet reconstruction and calibration is shown in Figure 5.7. A more detailed overview of the Jet Energy Scale (JES) and Jet Energy Resolution (JER) corrections is given in Ref. [140].

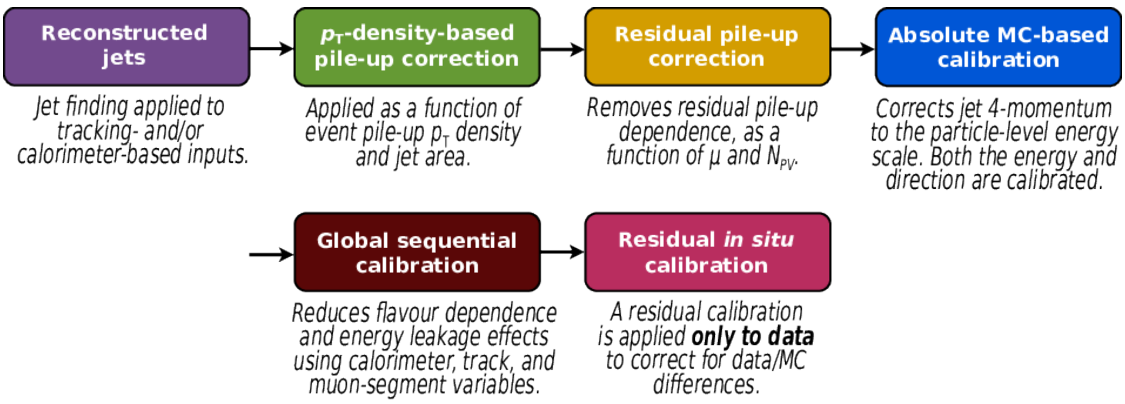

Figure 5.7: Schematic steps for the jet reconstruction and calibration [140].

The jets used in the measurement presented in this thesis have a requirement of $p_T > 25$ GeV and $|\eta| < 2.5$.

5.4.3 Jet Vertex Tagger

The pile-up interactions can lead to additional reconstructed jets in an event, which are not of interest. These jets can are identified and suppressed with the use of the Jet Vertex Tagger (JVT) [145]. The JVT is a multivariate algorithm which outputs the probability that a jet is originated by the primary vertex. It is based on two inputs: the fraction of the total momentum of tracks in the jet which is associated to the primary vertex (JVF) [146] and on the number of primary vertices in the events, N_{PV}. The former is defined as the ratio of the p_T sum of the tracks which are associated with the jet and originate from the hard-scatter vertex and the p_T sum of all the associated tracks. The JVT is only used for jets within $|\eta| < 2.5$. For more forward jets, the forward Jet Vertex Tagger (fJVT) is used, which is detailed in Ref. [147]. The JVT is constructed in such a way that the resulting hard-scatter jet efficiency is stable as function of N_{PV}. This requirement on the jet tracks reduces the fraction of jets from pile-up to 1%, with an efficiency for pure hard-scatter jets of about 90%.

5.4.4 b-tagging algorithms in ATLAS

Identifying jets containing a b-quark is referred to as b-tagging. When a b-quark is produced during a collision event, it hadronizes to form a jet in the detector, known as the b-jet. b-tagging is used to study the properties of the decay modes of the b-hadrons, using the reconstructed tracks associated with the corresponding b-jet.

The algorithms used for b-tagging exploit the characteristic lifetime (τ of b-hadrons $1.5 \cdot 10^{-12}$ s, that corresponds to a travelled distance of $c\tau \sim 0.45$ mm inside the detector before they decay. They are therefore characterised by topologies with at least one displaced vertex with respect to the point where the hard-scatter collision occurred. The algorithms used by the ATLAS experiment to identify the b-jets are described below [148].

In order to characterise the performance of b-tagging in simulation, it is necessary to assign a label to the jets based on the truth information obtained from MC simulations. If a b-hadron with a transverse momentum $p_T > 5$ GeV is found within a cone of radius $R = 0.3$ centered on the jet axis, the jet is classified as a b-jet. If no b-hadron is detected, the same procedure is repeated for c-hadrons and τ-leptons. Any remaining jets are categorized as *light*-jets[2].

The low-level taggers

To identify the b-jets ATLAS has developed multiple low-level taggers, which are based on different features of the b-jets. These low level algorithms are then combined together into the high-level taggers.

[2]A *light*-jet refers to a jet originating from a $u/d/s$ or *gluon*

The IP2D and IP3D [149] taggers are the two primary algorithms based on the impact parameter (IP) associated with the jet. The IP2D only considers d_0 as discrimintant, while IP3Dmakes also use of the z_0 parameter and its correlation with d_0. For both the taggers, a Log-Likelihood Ratio (LLR) quantifies the probability for a track to be compatible with a b-, c- or a *light*-jet. Since the IP2D and IP3D don't account for correlation between the tracks a Recurrent Neural Network (RNNIP) [150] has been developed, it takes tracks as input and produces a single output score for each jet.

ATLAS employs two algorithms for secondary vertex reconstructions. SV1 [151] reconstructs the displaced vertex, while JetFitter [152] performs a reconstruction of the full weak decay chain of the b-hadron. All of these low-level taggers are combined using a multivariate classifier to maximize the performance of b-tagging and obtain high-level taggers.

These low-level taggers are then combined into the High-Level Taggers (HLT) to increase the discrimination power of identifying the b-jets.

The high level taggers

During ATLAS history, there are several variants of the high-level taggers were implemented [153]. The one that will be discussed in the following is the one relevant for ATLAS Run 2 and for the measurement presented in this thesis. The more advanced version optimised for Run 3 can be found in Ref. [154].

The DL1r algorithm combines the low-level taggers in a deep neural network. The outputs of DL1r are represented by p_b, p_c, and p_{light}, indicating the probabilities of a jet being classified as b-, c-, or *light*, respectively. These probabilities are then combined to generate a single output score for each jet ($\mathrm{D_{DL1}}$):

$$\mathrm{DL1} = \ln \frac{p_\mathrm{b}}{f_\mathrm{c} p_\mathrm{c} + (1 - f_c) p_\mathrm{light}} \tag{5.3}$$

where f_c is the fraction of c-jet events used in the training, that is set to 0.0018.

From the output score of the three high level taggers, different *Working Points* (WP) are defined, independently of the jet p_T, corresponding to a b-jet tagging efficiency of $60\%\,, 70\%\,, 77\%\,, 85\%$. The b-jet tagging efficiency is defined as:

$$\epsilon^{flav} = \frac{N^{flav}_{pass}(D_{HLT} > T_f)}{N^{flav}_{total}} \tag{5.4}$$

where ϵ^{flav} is the efficiency for b-, c- or *light* flavoured jet, in which for each flavour the denominator is the total number of jets, while the numerator represents the number of jets with a High Level Tagger score (D_{HLT}) larger then a threshold T_f, where T_f is the cut value of the WP derived using a $t\bar{t}$ sample.

Figure 5.8 illustrates the efficiency of b-tagging and the c-jet rejection factor, defined as the inverse of the efficiency for a background jet to pass the given selection requirement, as a function of the transverse momentum of the jet for three high-level taggers. All three taggers exhibit similar levels of performance for what concerns the b-jet.

The efficiency of tagging a c- or a *light*-jets as a b-jets is the *mis-tag rate*.

An incorrect modelling of the variables used for the identification of the heavy quarks in Monte Carlo simulations would result in different labelling efficiency in data and Monte Carlo. To correct for these effects the performance in the simulation is matched to the data by special calibrations. The calibrations are performed in $t\bar{t}$ dilepton events for b jets and c jets, while the *light* jets are calibrated with Z+jets events.

Scale factors (SF) are defined to match the b-tagging performance of the simulations to that of the data. They are defined as a function of the transverse momentum, as

$$SF_{data-MC} = \frac{\epsilon_{data}}{\epsilon_{MC}} \tag{5.5}$$

where ϵ_{MC} is the efficiency computed in simulation with parton shower models for a $t\bar{t}$ sample based on `Powheg+Pythia8` generator and ϵ is the efficiency calculated from data. The scale factors are derived separately for b-, c- and *light*-flavour jets and are assumed to be independent between different jets. The scale factors are applied as a multiplicative correction to the event weights in the analyses.

The analysis presented in this thesis selects b-jets with 77% efficiency working point. This means that the efficiency of b-tagging a b-jet is 77%. Using this working point also means that 20% of the c-jets are mis-identified as b-jet and less than 1% of the *light*-jets mis-identified as b-jets.

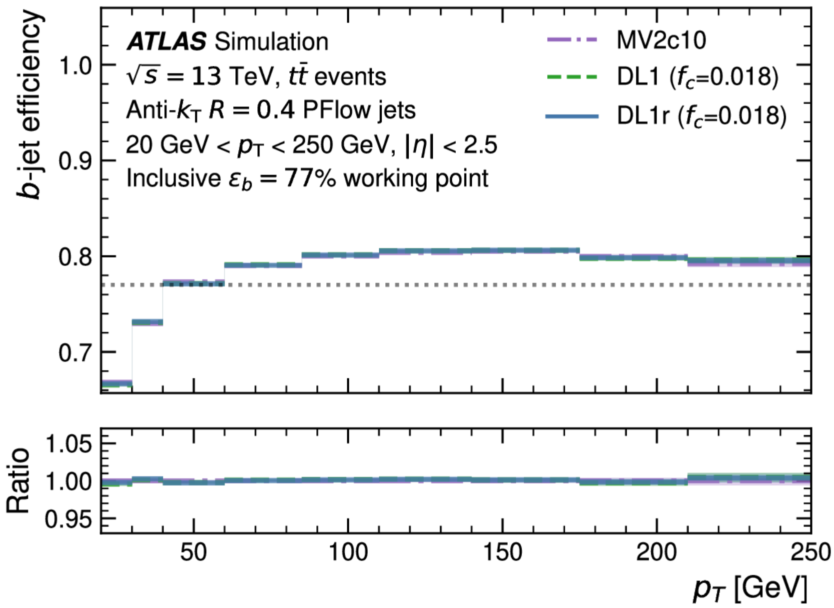

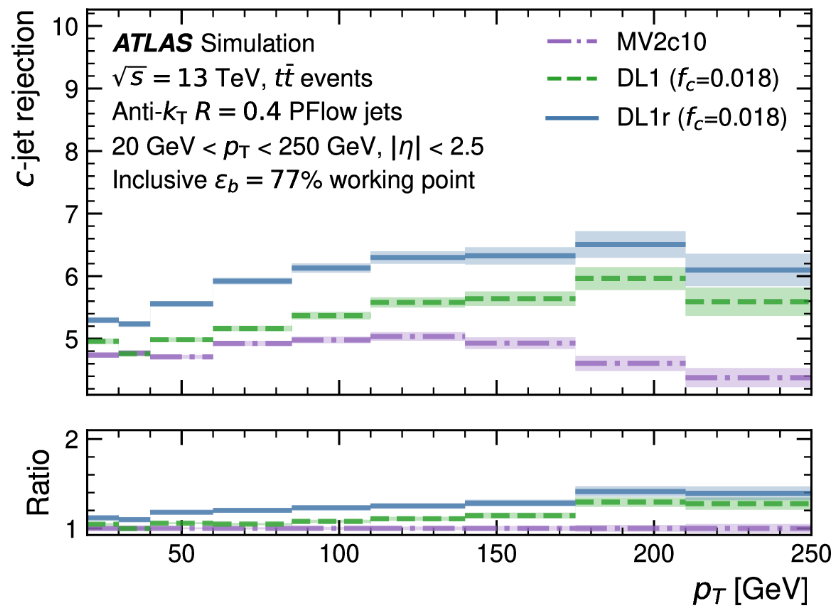

Figure 5.8: The b-tagging efficiency, ϵ_b, and c-jet rejection factor for several high-level b-taggers, including DL1r, as a function of jet p_T, evaluated using simulated $t\bar{t}$ events, for the 77% WP. The lower panels show the ratio of each algorithm's performance to that of MV2c10. The statistical uncertainties of the efficiencies are indicated as coloured bands [148].

5.5 Overlap Removal

The physics objects are reconstructed individually, as explained in the previous sections. However, it may happen that a physical object is reconstructed by several different algorithms, which are designed to reconstruct different particles, e.g. an electron is also reconstructed as a jet, resulting in a double counting of energy deposit in the calorimeter. This can lead to an overlap of these objects. To avoid reconstruction ambiguities and double counting, an overlap removal procedure is applied, depending on the definition of the objects involved. The following overlap removal procedure is applied to the baseline leptons and jets:

- First, calorimeter-tagged muons are removed if sharing an ID track with electrons,
- All electrons sharing an ID track with a muon are removed,
- Jets which lie in a cone of $\Delta R = \sqrt{(\Delta\eta)^2 + (\Delta\phi)^2} = 0.2$ around an electron candidate are removed.
- All jets lying within $\Delta R = 0.2$ of an electron are removed. Electrons within $\Delta R < 0.4$ of the remaining jets are discarded.
- Finally, jets within $\Delta R < 0.2$ of a muon and which either have less than three tracks or fulfil $p_T(\mu)/p_T(\text{jet}) > 0.5$ and $p_T(\mu)/\sum p_T(\text{all jet tracks}) > 0.7$ are removed. Muons overlapping with $\Delta R < 0.4$ of the remaining jets are removed.

5.6 Missing Transverse Momentum (E_T^{miss})

The missing transverse momentum (E_T^{miss}) arises due to undetected energy in the event, either due to neutrinos escaping detection or to other particles outside the acceptance.

The momentum imbalance is defined in the transverse plane, as $\overrightarrow{p}_T^{miss} \equiv (p_x^{miss}, p_y^{miss}, 0)$, a schematic view of the $\overrightarrow{p}_T^{miss}$ is shown in Figure 5.9. The magnitude of the missing transverse momentum is referred to as the *missing transverse energy* $E_T^{miss} := |\overrightarrow{p}_T^{miss}|$.

The reconstruction of the E_T^{miss} is performed at the analysis stage, by including the reconstructed physics object (hard term), as well as additional signatures that are not associated to other objects or objects that fail analysis selection-criteria (soft term). The latter can be *calorimeter-based* or *track-based.* The track-based

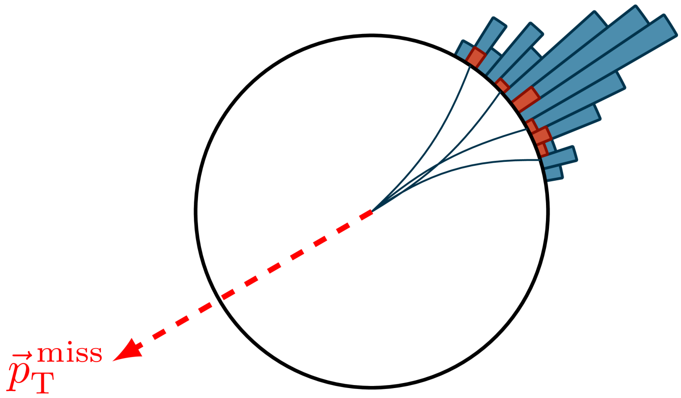

Figure 5.9: Schematic view of the momentum imbalance [35].

method is used in the measurement presented in this thesis due to its enhanced performance in E_T^{miss} against pile-up [155].

The E_T^{miss} is reconstructed as:

$$E_T^{miss} := \left| -\sum_{e} \vec{p}_T^{\,e} - \sum_{\mu} \vec{p}_T^{\,\mu} - \sum_{\tau} \vec{p}_T^{\,\tau} - \sum_{\gamma} \vec{p}_T^{\,\gamma} - \sum_{\mathrm{jet}} \vec{p}_T^{\,\mathrm{jet}} - \sum_{\mathrm{soft}} \vec{p}_T^{\,\mathrm{soft}} \right| \quad (5.6)$$

The correct determination of E_T^{miss} is challenging as it requires the reconstruction of all other objects and precise measurements of the properties in all detector subsystems, leading to a complete description of the hard scatter of interest. The constructed value for E_T^{miss} is therefore strongly influenced by the excellent, but still limited, resolution of the detector and sensitive to pileup.

A complete description of E_T^{miss} definition and performance can be found in Ref. [156].

6
Event Selection and Background Estimation

The $WbWb$ final state is a complex final state which encompasses contributions from various topologies. In this thesis the considered final state is the semileptonic final state, in which one of the W decays leptonically and the other one decays hadronically. The dilepton final state has been analysed in ATLAS Run-1, and the result is shown in Chapter 2. The semileptonic channel is the best compromise between statistics and purity of selection, as explained in Chapter 2.

In this case, the $WbWb$ final states is:

$$pp \to WbWb \to l\nu q\bar{q}b\bar{b} \tag{6.1}$$

where $l = e^-, \mu^-$ and $\nu = \bar{\nu}_e, \bar{\nu}_\mu$.

The analysis presented in this thesis focuses on two kinematic regions. The first, which will be referred to as *measurement-like phase space (MLPS)*, considers a rather inclusive phase space in order to constrain the interference effects between the $t\bar{t}$ and tW processes.

The second region is referred to as the *search-like phase space (SLPS)* due to its purpose of investigating a phase space typically targeted by Beyond Standard Model searches. This region is motivated by large impact observed by various searches of systematic uncertainties related to the modeling of $t\bar{t}$ and tW interference. Examples of such uncertainties include SUSY searches [8] or searches for Dark Matter [9].

6.1 Interference sensitivity metrics

Two metrics have been defined to assess whether an observable is sensitive to interference between tW and $t\bar{t}$. The first metric measures the difference between DR and DS simulated tW samples as follows:

$$\frac{N_{\text{DS}}}{N_{\text{DR}}} \tag{6.2}$$

where the quantities N_{DR} (N_{DS}) are the number of events simulated with the single-top DR (DS) generators, respectively, passing the event selections. The events are normalised to the luminosity. This ratio it is at least 5% in at least 50% of the bins of each observable under study, with peaks up to 20% for the most sensitive distributions in the measurement-like phase space and up to 50% in the search-like phase space.

Given the variation in the modelling of the tW sample, measuring the quantities that are sensitive to it will help to tune the generators. This will specifically highlight areas of phase space where the modelling may be inaccurate. It is also important to measure any region where the proportion of tW contribution is significant, as effects of interference cannot be observed in areas of the phase space where the top-pair process vastly dominates over the single-top process. This effects leads to the definition of a second metric, defined as the fraction of tW events in the signal:

$$\frac{N(tW)}{N(tW) + N(t\bar{t})} \tag{6.3}$$

For the search-like phase space, an additional metric is used to optimise event selection with respect to those described in Eq. 6.2 and 6.3. The Figure Of Merit (FOM), is defined as the difference between the purity of DR and DS, the first and second terms in the following equation, such that:

$$FOM = \frac{N_{\text{DR}}}{N_{\text{total-simulated(DR)}}} - \frac{N_{\text{DS}}}{N_{\text{total-simulated(DS)}}} \tag{6.4}$$

where N_{DR} (N_{DS}) are the number of events simulated with the single-top DR (DS) generators passing the event selections. $N_{\text{total-simulated(DR)}}$($N_{\text{total-simulated(DS)}}$) are the total number of events simulated with the single-top DR (DS) generators.

6.2 Event selection

The selection is optimised using simulated MC event samples. All events are required to contain exactly one signal lepton as defined in Chapter 5. Events are selected with a single lepton trigger and a minimum p_T requirement of $> 30\,\text{GeV}$ is placed on the lepton. Furthermore the expected number of jets in the signal is 4 (2 jets from top-quark decays and 2 from W-boson decays), so a preselection condition of at least 4 jets and at least 2 b-jets in the event, tagged at the 77% WP, is applied. The neutrino from the second W-boson decay introducesE_T^{miss}. This allows a cut on $E_T^{miss} + m_T^W > 60\,\text{GeV}$ to be applied to remove the QCD background, which in this case enters the selection as a mis-identified or non-prompt lepton. The m_T^W is defined as the transverse mass computed from the lepton and E_T^{miss} 4-vectors where the z-component is set to 0.

In the search-like phase space, additional event selections are incorporated, to bring the phase space close to the one targeted by searches. In this particular region, both the transverse momentum of leptons (p_T) and missing transverse energy (E_T^{miss}) demonstrate sensitivity to the difference between DR and DS. For the characteristic distributions please refer to figures in Section 6.4.

To enhance the sensitivity of the measurement to the interference in the search-like region, a requirement is imposed on the linear combination of E_T^{miss} and p_T as follows:

$$E_T^{miss} > -A \cdot p_T(l) + C \tag{6.5}$$

where A and C represent the gradient and the intercept, respectively. The combination maximise the separation between DR and DS while maintaining enough statistical data. The cut is set at $E_T^{miss} > -0.625 \cdot p_T(l) + 270\,\text{GeV}$. A scheme of the cut is shown in Figure 6.1.

In addition to the baseline selection, other cuts are introduced to suppress $t\bar{t}$ events and to enhance the difference between DS and DR as a proxy for a phase space sensitive to the interference:

- The m_{bl}^{min} variable, described in 6.3.1, was chosen to discriminate single-top from $t\bar{t}$ events. It was found that selecting a phase space where events containing two on-shell top quarks were suppressed provided a strong sensitivity to the interference. This was achieved by selecting $m_{bl}^{min} > 150\,\text{GeV}$.

- The $\Delta R(b_1, b_2)$ variable, described in 6.3.3, was chosen to further reduce the $t\bar{t}$ on-shell background. The cut applied was set at $\Delta R(b_1, b_2) > 1.4$.

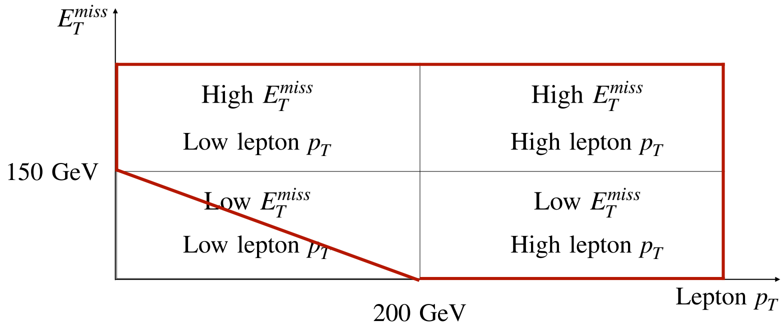

Figure 6.1: Scheme of the triangular cut in the search-like phase space

- The Leading b-jet p_T variable was chosen to reduce the $t\bar{t}$ on-shell and W+jets backgrounds. This was set to $p_T(b_1) > 160\,\text{GeV}$.

The summary of the event selection can be found in Table 6.1.

Selection	measurement-like phase space	search-like phase space
N_{jets}	≥ 4	
N_{b-jets}	≥ 2	
$E_T^{miss} + m_T^W$	$(60, \infty)$	
$p_T(l)$	$(30, \infty)$	
$p_T(j)$	$(25, \infty)$	
E_T^{miss}	—	$\geq -0.625\, p_T(l) + 270$
m_{bl}^{min}	—	$(150, \infty)$
$p_T(b_1)$	—	$(160, \infty)$
$p_T(b_2)$	—	$(50, \infty)$
$\Delta R(b_1, b_2)$	—	$(1.4, \pi)$
$p_T(j_1, j_2)$	—	$(50, \infty)$

Table 6.1: A summary of the event selection for measurement-like and search-like phase space.

6.3 Studied observables

To suppress a large fraction of semi-leptonic on shell $t\bar{t}$ events and SM background, dominated by W+jets events, a number of discriminating variables have been selected. Out of basic quantities as lepton p_T, leading b-jet p_T and subleading b-jet p_T show both high fraction of tW events in the signal and large DR/DS difference. Several compound variables have also been defined, which are introduced below. Missing transverse momentum is used as defined in Section 5.6. All the variables are shown in Section 6.4.

6.3.1 m_{bl}^{min}

It is the invariant mass of a b-jet and a lepton [10], it is a quantity that discriminates very well between resonant and non-resonant $WbWb$ production. m_{bl}^{min} constrains well one of the $t\bar{t}$ top quark decays, because it is expected that m_{bl} is always below m_{top}, while in non-resonant Wb systems m_{bl} can have any value. Therefore events which have $m_{bl} > m_{top}$ indicate that at least one of the two Wb pairs was produced non-resonantly.

It is designed to feature and end point at 150 GeV for a b-jet and a lepton coming from the decay of an on-shell top quark. An ambiguity is present when pairing the correct b-jet to the lepton. The solution which provides the highest sensitivity is:

$$m_{bl}^{min} \equiv \min\{m_{b_i l}\} \tag{6.6}$$

where the b_i goes over all b-jets in the event. As a result of the suppression of the on-shell $t\bar{t}$ contribution for high values of m_{bl}^{min}, the differential cross-section above this kinematic endpoint has an increased sensitivity to Wb systems with a higher invariant mass, which is greater than the one expected from resonantly decaying top quarks.

6.3.2 Asymmetric stranverse mass

It is based on the definition of the stransverse mass, which is an extension of the transverse mass. It is used to measure masses of particles pair produced at hadron colliders, where each particle decays to one particle that is directly observable and another particle whose existence can only be inferred from missing transverse momenta.

The symmetric $m_{\mathrm{T}2}$ variable is defined as

$$m_{T2}(\mathbf{p}_{T,1}, \mathbf{p}_{T,2}, \mathbf{E}_T^{miss}) = \min_{\mathbf{q}_{T,1}+\mathbf{q}_{T,2}=\mathbf{E}_T^{miss}} [\max(m_T(\mathbf{p}_{T,1}, \mathbf{q}_{T,1}), m_T(\mathbf{p}_{T,2}, \mathbf{q}_{T,2}))], \tag{6.7}$$

where m_T is the transverse mass, $\mathbf{p}_{T,1}$ and $\mathbf{p}_{T,2}$ indicate the transverse momentum vectors of two particles of the same mass and E_T^{miss} is the missing transverse momentum vector.

It can be generalised for the asymmetric case where one of the particles of the same mass decays fully visibly and the other decay involves an invisible particle, as is the case for the $t\bar{t}$ channel in this analysis [157].

$$am_{T2}(\mathbf{p}_{T,b1}, \mathbf{p}_{T,b2}, \mathbf{p}_{T,\ell}, \mathbf{E}_T^{miss}) = \min[m_{T2}(\mathbf{p}_{T,b1}+\mathbf{p}_{T,\ell}, \mathbf{p}_{T,b2}, \mathbf{E}_T^{miss}), m_{T2}(\mathbf{p}_{T,b1}, \mathbf{p}_{T,b2}+\mathbf{p}_{T,\ell}, \mathbf{E}_T^{miss})] \tag{6.8}$$

where m_{T2} is the stransverse mass, $\mathbf{p}_{\mathrm{T},1}$ and $\mathbf{p}_{\mathrm{T},2}$ indicate the transverse momentum vectors of two particles of different mass (the b-jets and the lepton) and E_T^{miss} is the missing transverse momentum vector.

6.3.3 $\Delta R(b_1, b_2)$

It is the distance between two b-tagged jets, it is used to further reduce the $t\bar{t}$ non-resonant contribution. It is defined as:

$$\Delta R(b_1, b_2) = \sqrt{(\eta_{b_1} - \eta_{b_2})^2 + (\phi_{b_1} - \phi_{b_2})^2} \tag{6.9}$$

It can evade the m_{bl}^{min} kinematic end point at 150 GeV if the two b-tagged jets used in the reconstruction do not originate from the two top decays, but instead from the b- and a misidentified c-quark from a hadronic top decay.

6.4 Detector-level plots

Sensitive variables were defined by evaluating the sensitivity metrics described in Section 6.1. They can be split into two categories, where the sensitivity to the tW and $t\bar{t}$ interference is targeted: basic quantities describing individual particles and more complex composite quantities. Figures 6.2 and 6.3 show the expected distributions of lepton p_T, leading b-jet p_T, E_T^{miss} and m_T^{min} (bl), for the measurement-like and search-like phase space, respectively. The top panel of the figures shows the detector-level distribution of the signal, which is composed of $t\bar{t}$ and tW (DR) samples, shown with a green line. The DS signal sample is shown in purple. The different backgrounds are also shown in different colours, the dominant backgrounds being W+jets, in orange. The metric discussed in Equation 6.3 is shown in the first bottom panel. The green line represents the nominal signal modelling sample (DR), while the purple line represents the alternative modelling sample (DS). The ratio highlights the regions where the tW contribution is significant: a lower value indicates a higher tW contribution. In this ratio, the tW contribution is highest in the case of the Diagram Subtraction (DS), for all the six variables. The second ratio plot shows the second metric, as defined in Eq. **??**. This ratio highlights the discrepancy between DR and DS generators, it reveals the inconsistencies between different theoretical predictions for all variables.

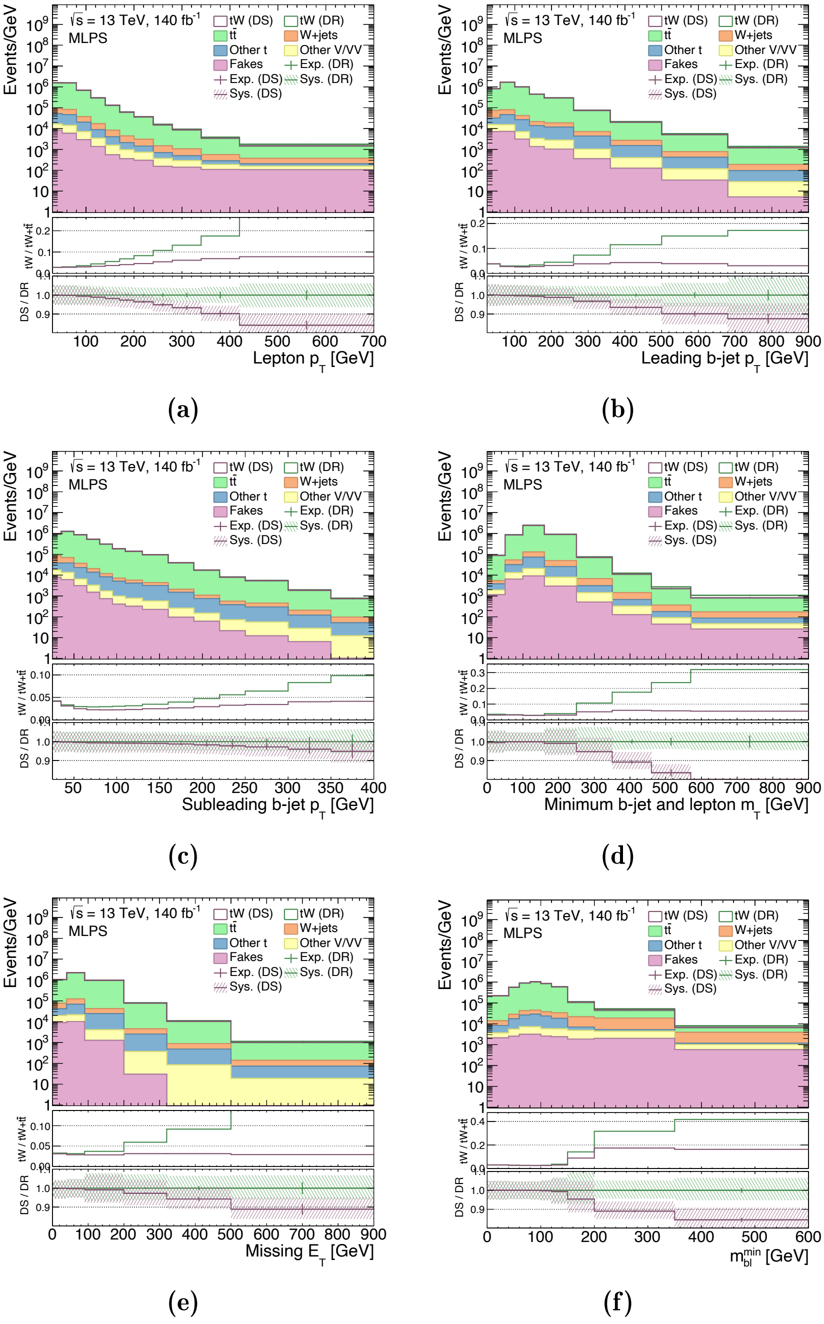

Figure 6.2: Kinematic distributions of basic and compound variables sensitive to the interference between $t\bar{t}$ and single-top processes at detector level: a lepton p_T distribution, b leading b-jet p_T distribution, c subleading b-jet p_T distribution, d $m_T^{min}(bl)$ distribution, e E_T^{miss} distribution, f m_{bl}^{min} distribution. Detector-level distributions are compared with predictions using `Powheg + Pythia 8` as the $t\bar{t}$ signal model and both `Powheg + Pythia 8` DR and DS for the tW signal model. The two predictions differ only in the modelling of the tW contributions. The upper ratio panel displays the ratio of the tW contributions for each of the four modelling schemes to the combined $t\bar{t} + tW$ signal predictions. The lower ratio panel displays the ratio of the DS prediction to the nominal one. Expected data uncertainty is displayed using error bars. Shaded areas show Monte Carlo systematic uncertainty.

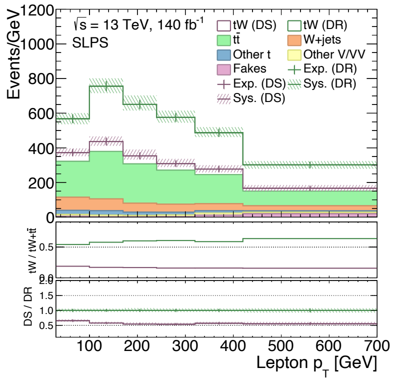

(a)

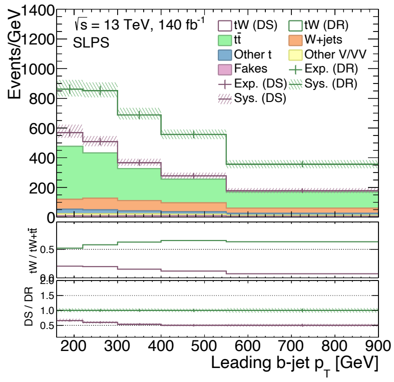

(b)

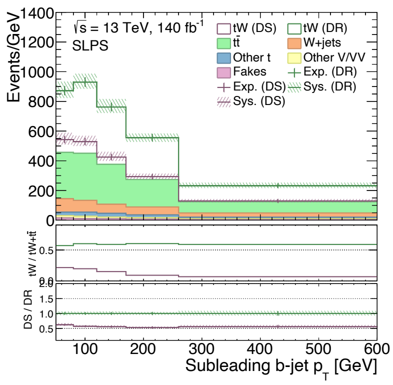

(c)

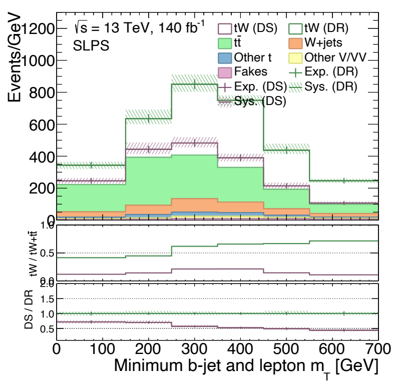

(d)

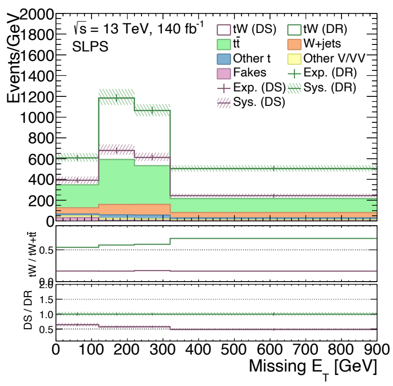

(e)

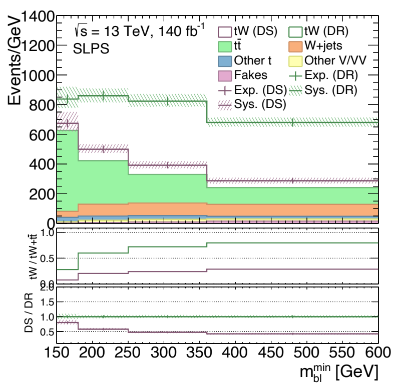

(f)

Figure 6.3: Kinematic distributions of basic and compound variables sensitive to the interference between $t\bar{t}$ and single-top at detector level: a lepton p_T distribution, b leading b-jet p_T distribution, c subleading b-jet p_T distribution, d leading $m_T^{min}(bl)$ distribution, e E_T^{miss} distribution, f m_{bl}^{min} distribution. Detector-level distributions are compared with predictions using `Powheg + Pythia 8` as the $t\bar{t}$ signal model and both `Powheg + Pythia 8` DR and DS for the tW signal model. The two predictions differ only in the modelling of the tW contributions. The upper ratio panel displays the ratio of the tW contributions for each of the four modelling schemes to the combined $t\bar{t} + tW$ signal predictions. The lower ratio panel displays the ratio of the DS prediction to the nominal one. Expected data uncertainty is displayed using error bars. Shaded areas show Monte Carlo systematic uncertainty.

6.5 Background Estimation

Several backgrounds have to be taken into account in the analysis. The W+jets, other vector boson (Z-jets and diboson events) and other top (s-channel and t-channel single top, ttV, ttH), are estimated using Monte Carlo simulations. The prompt background leptons originating from decays of Z-, W-, and H-bosons, or from prompt leptonic τ decays are also estimated using Monte Carlo simulations. The misidentified (mis-ID) lepton contributions, which come from processes such as in-flight decays of mesons, jets reconstructed as leptons, and electron photon conversions are estimated using the data-driven fake-factor method (briefly explained in Section 6.5.2).

The yields in the measurement-like phase space are listed in Table 6.2, and in Table 6.3 for the search-like one. These are estimated for all relevant Standard Model processes using Monte Carlo simulation described in Chapter 4.

Measurement-like Selection	Yield
Mis-ID lep.	$20\,370 \pm 150$
Other V	$25\,180 \pm 80$
Other *top*	$91\,080 \pm 67$
W-jets	$109\,800 \pm 260$
$t\bar{t}$	$4\,003\,000 \pm 700$
tW (DR)	$143\,100 \pm 140$
tW (DS)	$120\,500 \pm 130$
Expected	$4\,393\,000 \pm 780$
Data	$4\,305\,000 \pm 2100$

Table 6.2: Yields of individual signal and background samples in the measurement-like phase space. The total expected yield is estimated using the nominal $t\bar{t} + tW$ Diagram Removal (DR) sample. The alternative Diagram Subtraction (DS) scheme is also shown. The uncertainties are only statistical.

Although the Monte Carlo simulations are used for optimisation of the signal selection and for the estimate of the contamination of the Standard Model background processes, the analysis strategy is designed such that the normalisation of the dominant processes is directly derived from data, as explained in the following section.

Search-like Selection	Yield
Mis-ID lep.	42.11 ± 3.0
Other V	53.21 ± 0.93
Other *top*	74.26 ± 1.3
W-jets	274.1 ± 3.6
$t\bar{t}$	617.2 ± 4.0
tW (DR)	1542 ± 15
tW (DS)	187.6 ± 5.3
Expected	2603 ± 16
Data	1834 ± 43

Table 6.3: Yields of individual signal and background samples in the search-like phase space. The total expected yield is estimated using the nominal $t\bar{t} + tW$ Diagram Removal (DR) sample. The alternative Diagram Subtraction (DS) scheme is also shown. The uncertainties are only statistical.

6.5.1 W+jets Control Region

The dominant background in the analysis comes from the W+jets processes. A Control Region (CR) is defined to determine the background and to constrain the normalisation of the W+jets background in the measurement-like and search-like phase space. The control region is designed to have similar kinematic properties to the corresponding phase space but with inverted variable selection, to increase the yield and the purity of the background. The W+jets control region contains exactly three jets, which are selected to ensure orthogonality to the SR, two of which are b-jets. To further enhance the fraction of the W+jets events, a cut centred around the W-boson boson mass is applied through the variable m_T^W. In addition, to reduce the $t\bar{t}$ contribution, a cut is made at $m_{bl}^{min} > 180\,\text{GeV}$. The resulting W+jets selection is shown in Table 6.4 and the corresponding yields in Table 6.5.

Figure 6.4 shows the distribution of the m_{bl}^{min} variable. The purity of the W+jets sample is approximately 50 % and no significant sensitivity to the $t\bar{t}$ and tW interference is observed. A single-bin distribution is used in the likelihood fit as described in the following.

Selection	W+jets CR
N(central jet)	$= 3$
N_{b-jets}	≥ 2
$m_T^W + E_T^{miss}$	$(60, \infty)$
$p_T(l)$	$(30, \infty)$
$p_T(j)$	$(25, \infty)$
m_T^W	$(40, 100)$
m_{bl}^{min}	$(180, \infty)$
SR veto	enabled

Table 6.4: A summary of the event selection for the W+jets control region.

W-jets CR	Yield
Mis-ID lep.	$12\,820 \pm 88$
Other V	$21\,530 \pm 83$
Other top	6140 ± 19
W-jets	$198\,300 \pm 550$
$t\bar{t}$	$131\,000 \pm 130$
tW (DR)	$23\,810 \pm 60$
tW (DS)	$21\,250 \pm 56$
Expected	$393\,600 \pm 580$
Data	$412\,000 \pm 640$

Table 6.5: Yields of individual signal and background samples in the W+jets control region. The total expected yield is using the nominal tW DR sample. Uncertainties are statistical only.

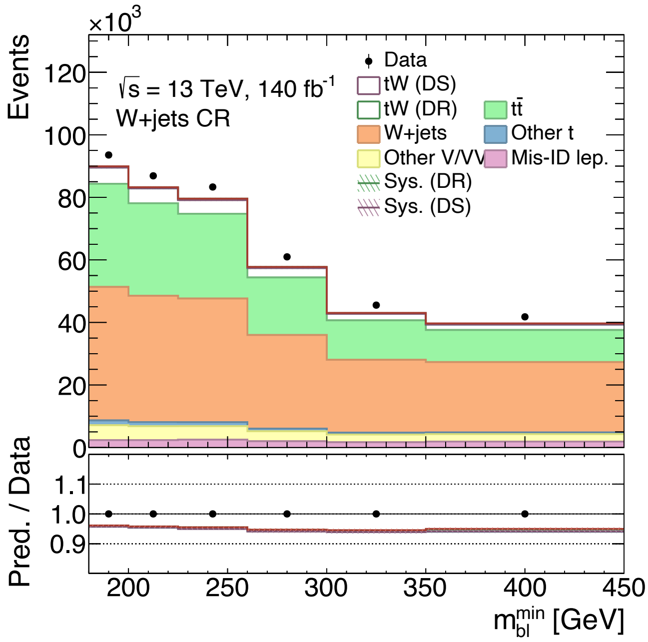

Figure 6.4: Distributions of the m_{bl}^{min} variable in the W+jets Control Region.

Likelihood Fit

The fitting procedure is implemented using the HistFitter [158] fitting framework.

A background-only likelihood fit is performed for the W+jets control region, introduced in the previous section. The likelihood fit aims to maximise the logarithm of the likelihood function, taking into account the observed data in the control region and the expected background predictions.

The fit is modelled by a probability density function (PDF), which combines a Poisson terms for all the events corresponding to the background processes in the relevant regions.

The normalisation of the W+jets background is regulated by a free-floating parameter, also known as the *normalisation parameter*. Additional parameters, referred to as *Nuisance Parameters (NP)*, are modelled with Gaussian distributions in order to account for uncertainties associated with various sources such as statistical fluctuations and systematic effects.

The HistFitter framework [158] internally splits each uncertainty nuisance parameter into normalisation and shape components. All the systematics are included the fitting process.

The extrapolation from the Control Region to the signal region is determined by the so-called *transfer factor* for the normalised W+jets background process. This factor determines the estimation of the yields in the measurement-like and search-like phase space and is calculated as:

$$N(\mathrm{PS, est.}) = N(\mathrm{CR, fit.}) \times \left[\frac{\mathrm{MC(PS, init.)}}{\mathrm{MC(CR, init.)}}\right] = \mu \times \mathrm{MC(PS, init)} \tag{6.10}$$

where $N(\mathrm{PS, est.})$ is the estimated background in the measurement-like and search-like phase space for the normalised W+jets background process, $N(\mathrm{CR, fit.})$ is the fitted number of events for W+jets in the control region, $\mathrm{MC(PS, init.)}$ and $\mathrm{MC(CR, init.)}$ are the initial estimates of the contributions from the W+jets background in the two analysis phase space and CR respectively, as obtained in the MC simulation. The ratio in the square brackets in Eq. 6.10 is defined as the *Transfer Factor* (TF). $N(\mathrm{CR, fit.})$ can be rewritten as μ, multiplied by a fixed nominal background prediction. μ is the *normalisation factor* obtained in the fit to the data. The application of the transfer factor allows systematic uncertainties in the predicted background processes to be (partially) removed in the extrapolation.

The normalisation factor for the W-jet background obtained from the fit to the data is $\mu = 1.095 \pm 0.099$.

The pre- and post-fit distributions for the measurement-like and the search-like phase space are shown in Figure 6.5 and 6.6, respectively. A small reduction in uncertainties is observed in the tail of the m_{bl}^{min} variable in the measurement-like phase space, where the fraction on W+jets background is particularly high. The uncertainty is still high as the signal modelling uncertainty is unchanged and only the W + jets background is affected by the fit.

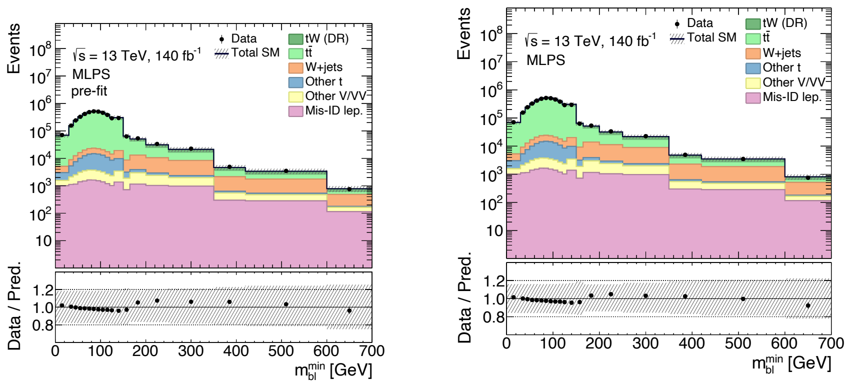

(a) (b)

Figure 6.5: Pre-fit and post-fit distributions for m_{bl}^{min} in the measurement-like phase space.

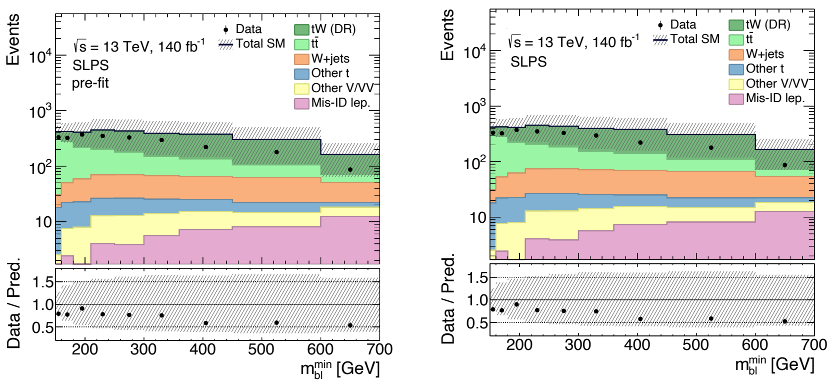

(a) (b)

Figure 6.6: Pre-fit and post-fit distributions for m_{bl}^{min} in the search-like phase space.

6.5.2 Fake and non-prompt leptons

The fake-factor method is a technique used to estimate the misidentified electrons, or muons, derived from a control region which is abundant in this type of background. For each misidentified lepton, a *fake factor* is calculated, which is a weight related to the probability of a mis-identified fake lepton satisfying the selection criteria of a prompt lepton. The events containing fake leptons are then weighted by the fake factors weights. The fake factors are measured in a control region, in which the data has orthogonal selections with respect to those in the analysis phase space.

Fake electrons arise from three background sources. They are either misreconstructed jets, mostly originating from light quark or gluon fragmentation, photon conversions or real electrons arising from secondary decays of light and heavy flavour mesons within jets. Fake electrons are typically less isolated than prompt electrons and have a lower chance of passing tighter identification levels. The simulation does not provide an optimal modelling of fake electrons which ultimately arise as the final product of a chain initiated by strong interactions.

Fake muons arise from in-flight decays of mesons inside jets with the semi-leptonic decay of the B meson as one of the largest contributions. Combinations of prompt and fake muons can contribute to the measurement region if the fake muons satisfy tight isolation and impact parameter requirements.

In the analysis presented in this thesis the fake and non-prompt background is negligible with respect to other backgrounds.

7
Unfolding

At a collider, measurements are typically based on counting experiments in which the observed events are classified according to their properties. The measured spectrum of the data differ from the Monte Carlo simulated spectrum, due to detector effects, as resolution, as well as limited acceptance and efficiency. Consequently, the reconstructed distributions of physical quantities cannot be directly compared with theoretical distributions or among different experiments. Data need to be corrected for these effects using the so-called *unfolding procedure*. The unfolding procedure has to be performed on data and can correct towards parton- or particle-level.

For this analysis, the particle-level approach is used, because parton-level is an ill-defined intermediate step in event generation, as explained in Chapter 4.

The aim of the unfolding is to retrieve the particle-level distribution $f(x)$ of a physical quantity x, starting from the experimental measurement y whose distribution $g(y)$, is altered by detector effects.

Detector effects can be categorised into two different categories:

- Detector efficiency and geometrical acceptance: not all events are included in the measurement of the physical quantity of interest due to geometric acceptance and trigger selection efficiency.

- Limited resolution effect: it is impossible to measure any physical quantity with infinite accuracy. As a result, there will be discrepancies between the measured value y and the true value x, resulting in a smeared distribution of $g(y)$ compared to $f(x)$.

The relation that links $f(x)$ and $g(x)$ is given by:

$$\int M_R(y,x)f(x)dx + b(y) = g(y) \tag{7.1}$$

where the function $M_R(y,x)$ represents the smearing function that accounts for detectors effects and resolution, while $b(y)$ denotes the background.

The equation 7.1 can be rewritten as a matrix equation representing discrete measurements, specifically events collected in histograms [159]:

$$M_R\vec{x} + \vec{b} = \vec{y} \tag{7.2}$$

The distribution $f(x)$ is discretised into a vector $\vec{x}$ of dimension M_x, which represents how many events fall in a histogram bin. Similarly, $g(y)$ and $b(y)$ are transformed into vectors $\vec{y}$ and $\vec{b}$, respectively, each of dimension M_y. M_R is the $M_x \times M_y$ *response matrix* containing the *matched* events, i.e. events passing both the particle-level and the detector-level selection. The response matrix M_R is derived from Monte Carlo simulations and describes how many events migrate from bin particle-level i to reconstructed-level bin j. Nevertheless, some events in a reconstructed-level bin may move to another bin at particle-level, this phenomenon is referred to as *bin migration*.

The *migration matrix* M is obtained by normalising the response matrix to the sum of the particle-level rows, as

$$M_{i,j} = \frac{M_{R,i,j}}{\sum_j M_{R,i,j}} \tag{7.3}$$

Figures 7.1 and 7.2 show the migration matrices for the measurement-like and the search-like phase spaces, respectively, for simple (lepton p_T, leading b-jet p_T) and compound variables (E_T^{miss}, m_{bl}^{min} and $m_T^{min}(bl)$) of the analysis, introduced in Chapter 6. The probability for reconstructed-level events to be reconstructed in the same bin as the particle-level event is represented in the elements on the diagonal of the migration matrix. The fraction of off-diagonal events represents the elements that migrated to the other bins.

The choice of bin boundaries is crucial for the migration matrix, as the fraction of events on the diagonal depends on them. Mathematically, the matrix has to be be injective, i.e. distinct and invertible. In the case of the analysis presented in this thesis, the variables at detector and particle level are basically linearly dependent and the requirement is to have at least 45% of the events on the main diagonal.

Since the migration matrix describes only those events that satisfy both the particle and reconstructed-level selection criteria, two correction factors have to be taken into account.

- Efficiency: this is the fraction of all events passing the particle-level selection in bin i that are also matched to detector-level (i.e. pass both the detector- and particle level selections). It can be calculated from the response matrix as $\epsilon_i = \sum_j M_{R,i,j}$. A low efficiency indicates that either the event selection at the detector level is too strict or that there are deficiencies in object identification or event reconstruction.
- Acceptance: this is the fraction of all events that pass the detector-level selection in bin j that are also matched at particle-level (i.e. pass both the detector- and particle level selections). It can be calculated from the response matrix as $\mathrm{A}_j = \sum_i M_{R,i,j}$. A low acceptance indicates that the event selection at the detector level is too loose. This factor takes into account events at the reconstructed level that do not fall within the fiducial region defined at the particle-level.

Efficiency and acceptance for the measurement-like and searches-like phase space are shown in Figures 7.3 and 7.4, respectively, for simple and compound variables of the analysis. The x-axis represents the detector-level variable in the case of the acceptance (in red) and the particle-level variable in the case of the efficiency (in blue). In the measurement-like phase space, the acceptance is of the order of 70%, meaning that 70% of the events passing the detector-level selection fall within the particle-level fiducial region. On the other hand, an efficiency of 30% means that 30% of the events passing the particle-level phase space selections are correctly reconstructed at detector-level. In the search-like phase space the acceptance is slightly lower, of the order of 60%, while the efficiency is of the same magnitude.

The procedure for solving Equation 7.2 for the vector of interest $\vec{x}$ is called unfolding. If $M_x = M_y$ and $\vec{y}$ are redefined as $\vec{y} \to \vec{y'} := \vec{y} - \vec{b}$, then Eq. 7.2 takes on the characteristics of an inverse problem. However, due to the statistical nature of the experiment, the observed event counts typically follow

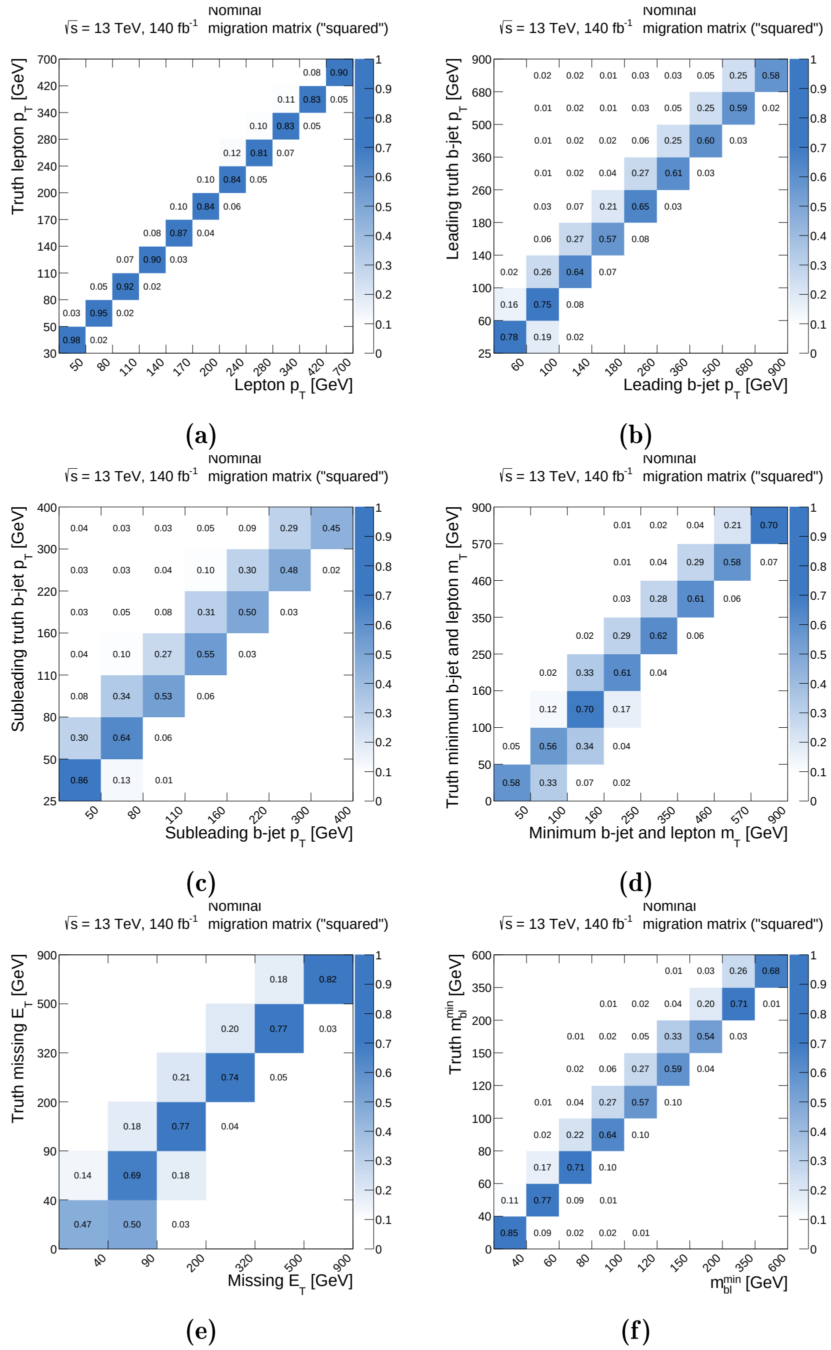

Figure 7.1: Migration matrix of: a lepton p_T distribution, b leading b-jet p_T distribution, c, c subleading b-jet p_T distribution, d $m_T^{min}(bl)$ distribution, e E_T^{miss} distribution, f m_{bl}^{min} distribution in the measurement-like phase space. The particle-level variables are displayed on the y-axis and the detector-level variables on the x-axis. The z-axis shows the percentage of the matched events in each bin.

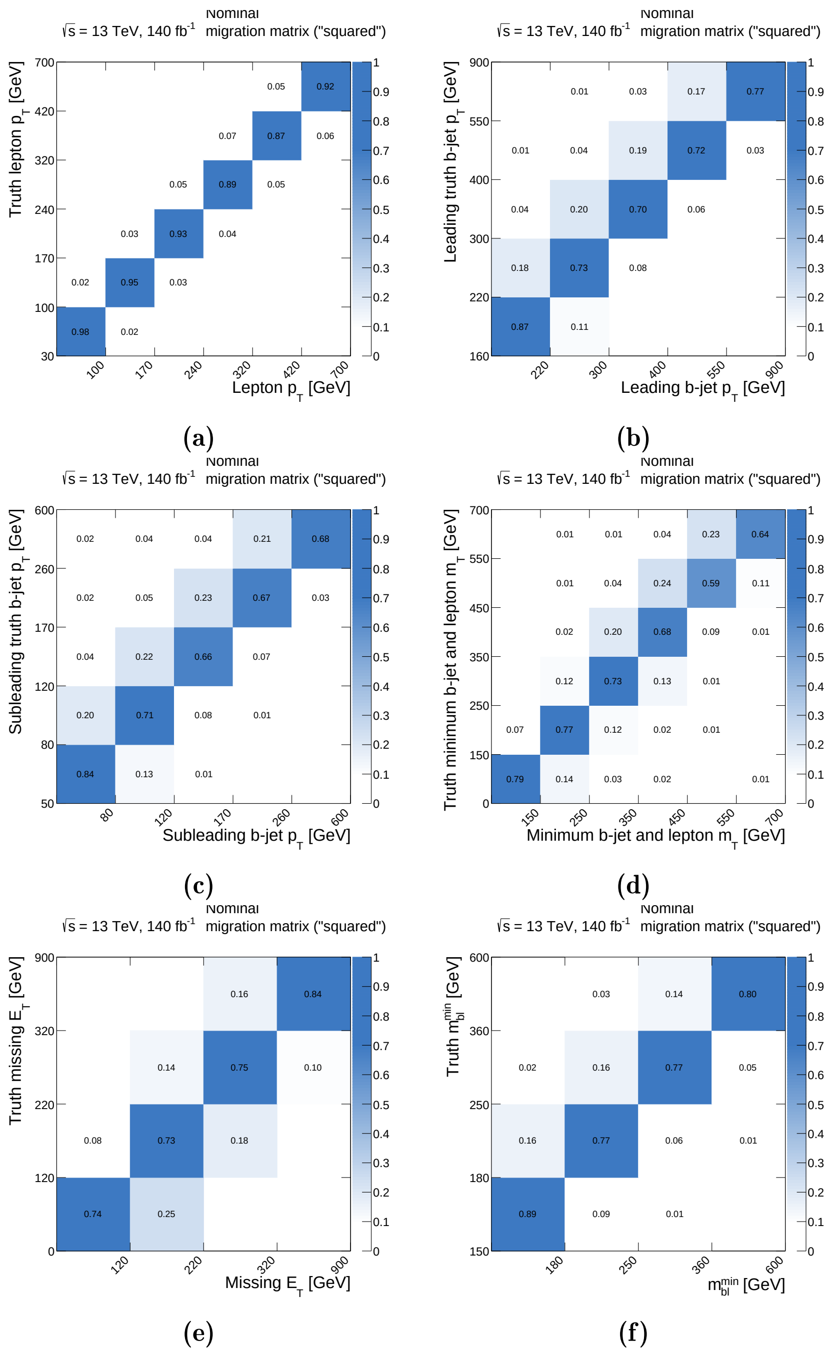

Figure 7.2: Migration matrix of: a lepton p_T distribution, b leading b-jet p_T distribution, c subleading b-jet p_T distribution, d $m_T^{min}(bl)$ distribution, e E_T^{miss} distribution, f m_{bl}^{min} distribution in the search-like phase space. The particle-level variables are displayed on the y-axis and the detector-level variables on the x-axis. The z-axis shows the percentage of the matched events in each bin.

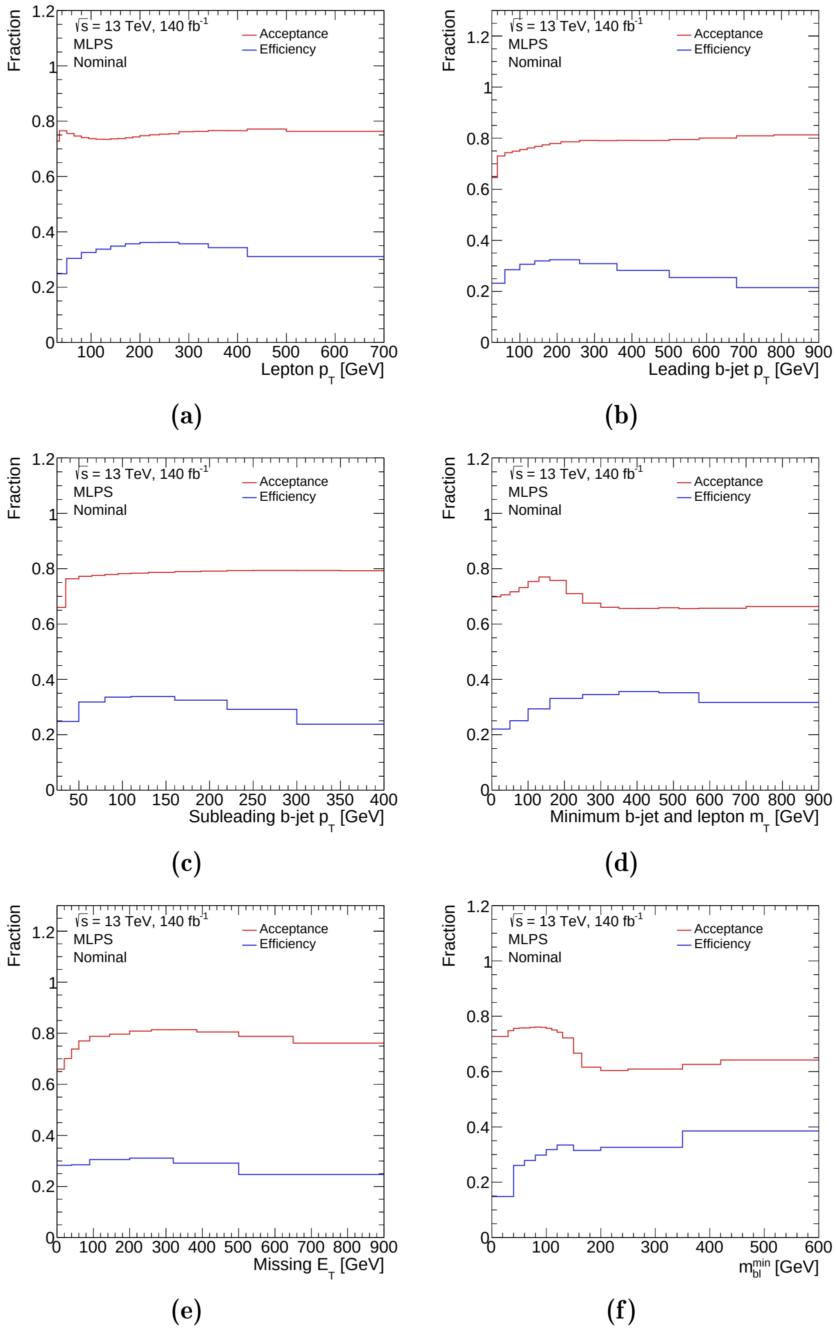

Figure 7.3: Acceptance (in red) and efficiency (in blue) for the measurement-like phase space: a lepton p_T distribution, b leading b-jet p_T distribution, c subleading b-jet p_T distribution, d $m_T^{min}(bl)$ distribution, e E_T^{miss} distribution, f m_{bl}^{min} distribution.

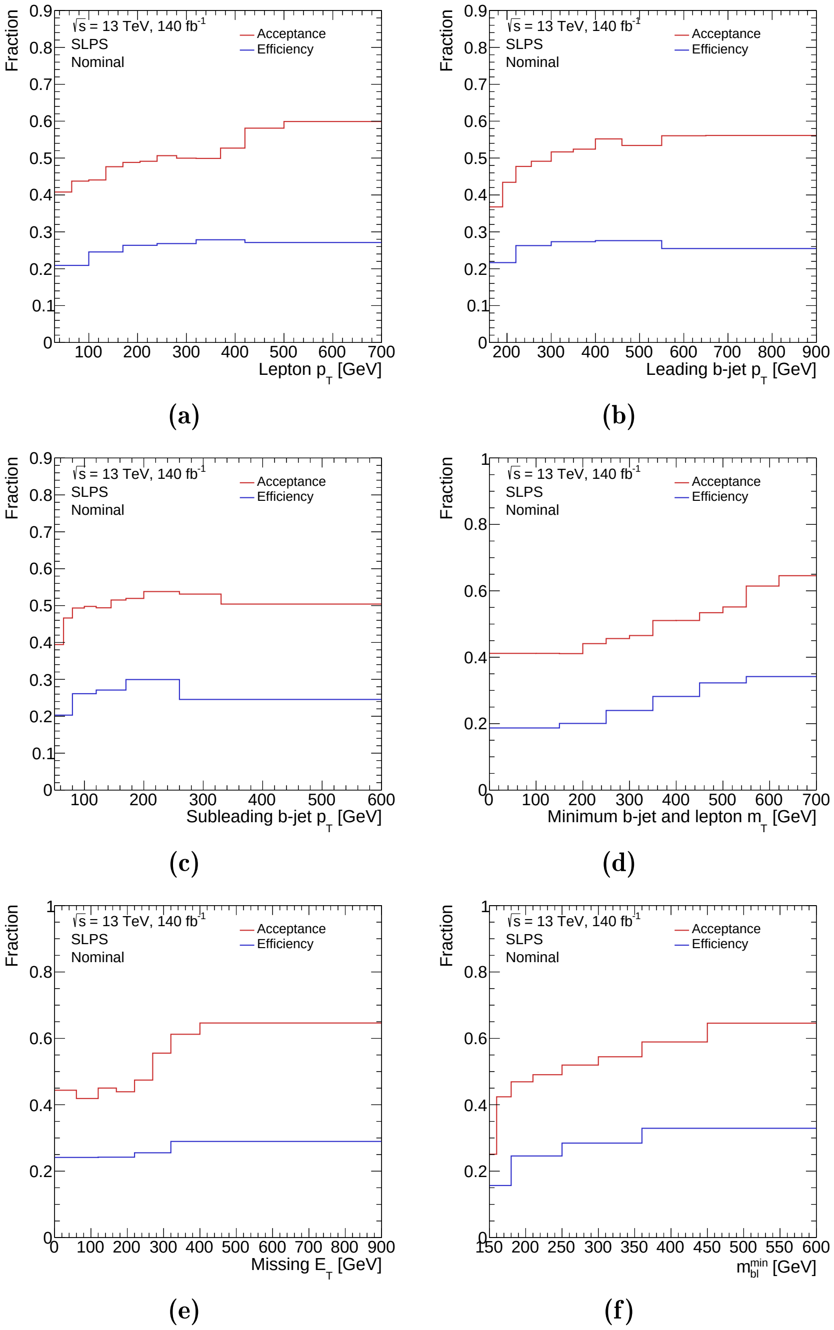

Figure 7.4: Acceptance (in red) and efficiency (in blue) for the search-like phase space: a lepton p_T distribution, b leading b-jet p_T distribution, c subleading b-jet p_T distribution, d $m_T^{min}(bl)$ distribution, e E_T^{miss} distribution, f m_{bl}^{min} distribution.

a Poisson distribution and often do not perfectly match the expected values. When Eq. 7.2 is solved by matrix inversion, these statistical fluctuations in $\vec{y'}$ can introduce significant statistical uncertainties. A more physically motivated approach to derive $\vec{x}$ from Eq. 7.2 is to impose the condition that $\vec{x}$ has to exhibit sufficient smoothness, which is achieved by a technique known as *regularisation.* This regularisation still uses the redefinition $\vec{y} \rightarrow \vec{y'} := \vec{y} - \vec{b}$, although the strict equality between M_x and M_y isn't mandatory. Regularisation reduces the effect of statistical fluctuations in the measured distribution $\vec{y'}$ on the unfolded result $\vec{x}$. A common approach to regularisation is Tikhonov regularisation unfolding [160], which is the method used in the analysis presented in this thesis. Alternative regularisation methods include for example Bayesian regularisation [161], iterative dynamically stabilised unfolding [162] and Gaussian process unfolding [163].

In the context of the analysis presented in this thesis, the unfolding procedure works as follows: starting with the observed number of events in the data (N_d), the procedure first subtracts the background contribution N_b (described in Chapter 6). Acceptance, migration and efficiency corrections are then applied, all of which are determined by Monte Carlo simulation of the signal sample. The acceptance correction A is applied first. The resulting distribution is then unfolded to the particle level. Validation of the optimised binning unfolding procedure is ensured by requiring that closure tests (see Section 7) are satisfied without introducing bias. An important application of the unfolding method is the measurement of the differential cross section $d\sigma$ of a process. The differential cross section of interest is a function of a kinematic variable X, and the procedure for measuring it can be summarised as follows:

$$\frac{d\sigma_{\text{fid}}}{dX_i} = \frac{1}{\mathrm{L} \cdot \Delta X_i} \cdot \frac{1}{\epsilon_i} \cdot \sum_j M^{-1}_{i,j} \mathrm{A}^j (N_{d,j} - N_{b,j}) \tag{7.4}$$

where ΔX_i is the bin width, L is the integrated luminosity, ϵ_i, A^j are obtained from MC as described above, $N_{d,j}$ and $N_{b,j}$ represent the data measured by the detector and the backgrounds, respectively. The inverted migration matrix as obtained with the iterative unfolding procedure is symbolised by M^{-1}. The index i runs over the particle-level bins and j on the detector-level bins.

The performance and the stability of the unfolding procedure has to be tested. Important tests are detailed in the following.

Closure tests

A closure test checks a fundamental property of unfolding: whether unfolding the Monte Carlo distribution of the reconstruction-level signal returns the Monte Carlo distribution of the particle-level.

In the *simple* closure test, the signal Monte Carlo reconstruction-level distribution is unfolded and compared to the Monte Carlo particle-level distribution. The Monte Carlo used to construct the migration matrix, efficiency, acceptance is exactly the same Monte Carlo which is used for the unfolding inputs. The following expression is evaluated, where $N_{T,i}$ is the unfolded signal Monte Carlo particle-level distribution in bin i and $U(N_{R,i})$ is the unfolded signal Monte Carlo reconstructed-level distribution in bin i.

$$\Delta_i = U(N_{r,i}) - N_{t,i}$$

If Δ_i is less than the statistical uncertainty calculated after the unfolding, the simple closure test is said to be successful. In the simple closure test, no statistical fluctuation are expected, because used the Monte Carlo samples are same in the matrix and in the inputs, such that they compensate. The result, for the measurement-like and searches-like phase space are shown in Figures 7.5 and 7.6, respectively, for simple and compound variables of the analysis. The particle-level distribution is shown with a solid black line and the unfolded data is shown with a solid blue line. All the closure tests are successful in both analysis regions.

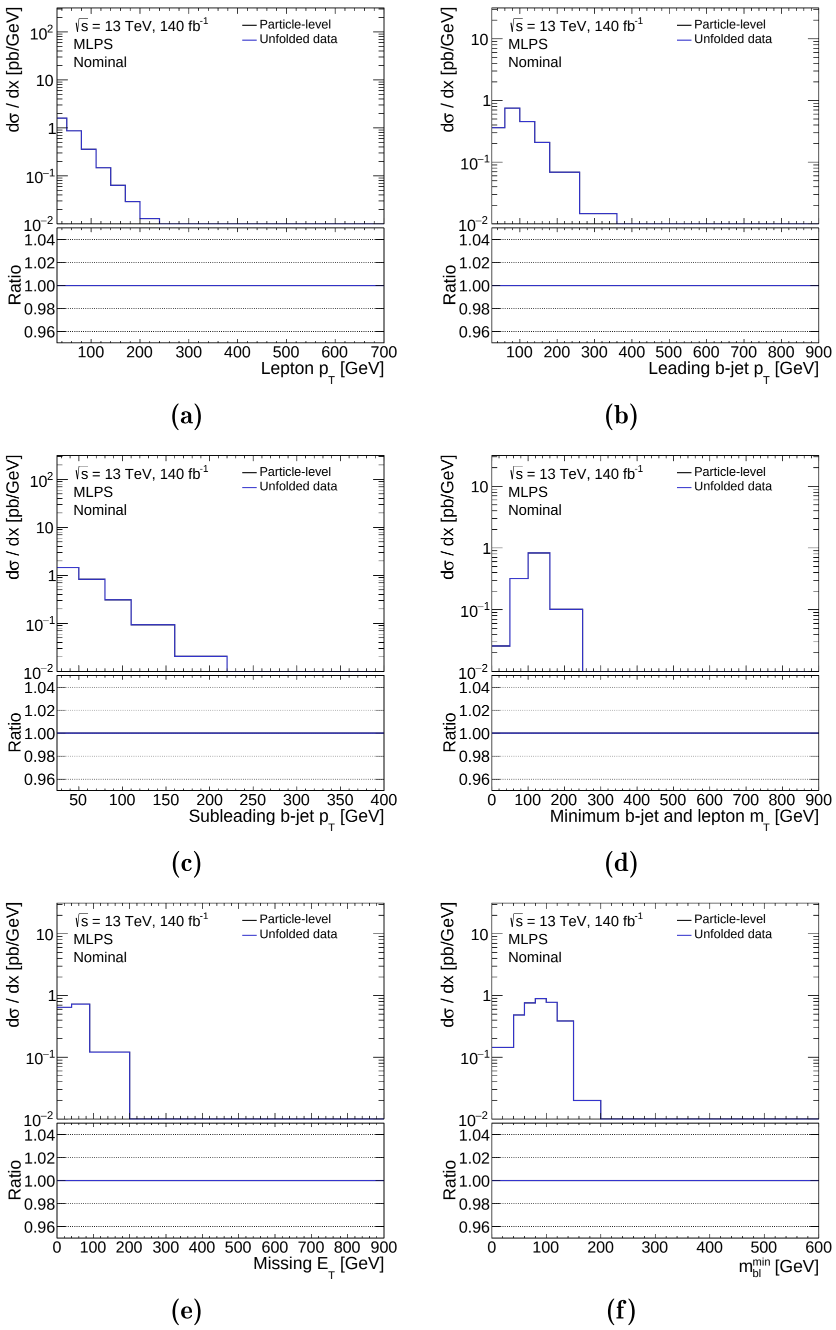

Figure 7.5: Closure test for the measurement-like phase space: a lepton p_T distribution, b leading b-jet p_T distribution, c subleading b-jet p_T distribution, d $m_T^{min}(bl)$ distribution, e E_T^{miss} distribution, f m_{bl}^{min} distribution.

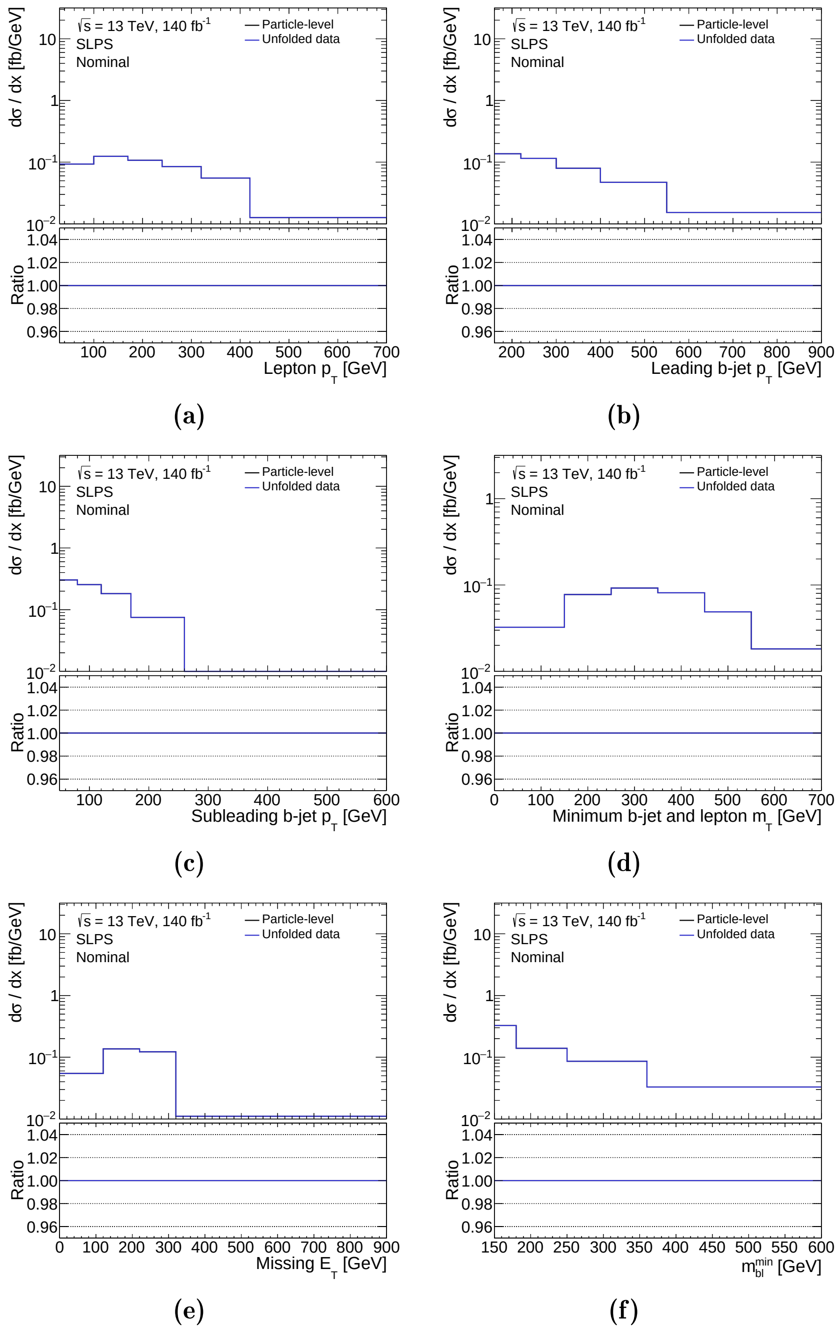

Figure 7.6: Closure test for the search-like phase space of the analysis: a lepton p_T distribution, b leading b-jet p_T distribution, c subleading b-jet p_T distribution, d $m_T^{min}(bl)$ distribution, e E_T^{miss} distribution, f m_{bl}^{min} distribution.

Stress tests

Ideally, the unfolding should be independent on the input distribution and a perfect closure should always be achieved. However, discrepancies in the shape of the distributions of the unfolded observables can lead to a bias of the result. Similarly, information is lost as the unfolding is only performed in one observable. Discrepancies in the shape of distributions in variables that are not unfolded (hidden variables) can also lead to a bias of the result. Stress tests are bias tests which evaluate how well the unfolding reproduces the particle-level distribution, or more specifically, whether both shape and normalisation are significantly different from the nominal signal for an input which is significantly different from the Monte Carlo simulation used to define the migration matrix.

The stress test uses a different input distribution from the standard Monte Carlo, either by using a different generator with a different model or by reweighting the input distribution. The latter method is used for the analysis and is explained in the following. Generally, stress tests define a weight per particle-level bin. This weight is then applied to all events that fall into the corresponding particle-level bin, as well as to the corresponding reconstruction-level event. The number of truth bins is denoted by n_t. First, n_t weights w_i are defined. Each truth event e_t falling into bin i is weighted with w_i. The corresponding reconstruction-level event e_r is weighted with w_i, too. Given these modified event-weights, the reconstruction- and particle-level distributions are calculated. The resulting distributions are denoted by T_i^{rw} and R_j^{rw} respectively. The weight of reconstruction-level events is not changed if their corresponding particle-level event is not contained in any of the particle-level distribution bins. However a reconstruction-level event is reweighted even if the particle-level event does not pass the fiducial criteria.

Stress tests compare the unfolded reweighted reconstruction-level $N_{r,j}^{rw}$ to the particle-level $N_{t,i}^{rw}$, that is, the bias

$$\Delta_i = U(N_{r,j}^{rw})_i - N_{t,i}^{rw}$$

is considered. If this difference is within the statistical uncertainties of the unfolding, no bias is assumed.

The weights to be used depend on the bias to be assessed. Several possibilities are evaluated in this analysis:

- In the *linear stress test* the weights are chosen such that $w_0 = -0.5$ and $w_{n_t} = 0.5$, with the weight increasing linearly across the truth bins. That is

$$w_i = \frac{2\beta}{n_t} i - \beta, \beta = 0.5.$$

  The linear stress test tests the bias with respect to large shape differences.

- In the *data-driven stress test*, the weights w_i are defined such that the difference $|N_{d,i} - N^{rw}_{r,j}|$ between the data and the reweighted reconstruction-level distribution is small. In this analysis, the weights are obtained by first unfolding the data with the matrix-inversion method, that is without any regularisation term by using the inverse migration matrix. A smooth function is then fit to the ratio $\frac{U_{\mathrm{MI}}(N_{d,i})}{N_{T,i}}$ of the matrix-inversion unfolded data and the particle-level Monte Carlo prediction (U_{MI} denotes the unfolding function for the matrix-inversion method). The weights w are then defined as the value of this smooth function. If $|N_{d,i} - N^{rw}_{R,i}|$ is small, the data-driven stress test evaluates the bias for a distribution that is similar to the data.

  If the difference Δi is smaller than the statistical uncertainties, the data-driven stress test is said to close. If it does not close, Δi is used as an additional uncertainty.

  The weights of the data-driven stress tests described here are calculated at particle-level.

In this analysis, a small modification to the stress test is applied to account for the fact that events that pass the event selection at reconstruction level, but not at the truth level, are not reweighted in the stress test. These events are treated as background at reconstruction level (only consider matched events in the unfolding process and no acceptance correction is carried out in the unfolding process.

The results for the linear stress test are shown in Figure 7.7 and 7.8 for the measurement-like and the search-like phase space, respectively. The uncertainties are statistical data uncertainties only. The unfolded reweighted reconstruction-level distribution and the reweighted particle-level distribution either agree within uncertainties, or the reweighted reconstruction-level distribution is just outside of the uncertainty band, such that the difference would be covered by the not shown uncertainties.

Results for the data-driven stress tests are shown in Figure 7.9 and 7.10, for the measurement-like and the search-like phase space, respectively. The agreement between the data and the reweighted detector-level distribution can not always be achieved to be within the statistical uncertainties from the data due to the demanding reweighting of some variables. Nevertheless, the unfolded reweighted detector-level distribution and the reweighted particle-level distribution agree within the Monte Carlo statistical uncertainties. Non-closure, if observed, yields an uncertainty that is well below the uncertainty observed from other sources as seen in Chapter 8.

The implementation of the systematic uncertainties in the unfolding procedure is shown in the next chapter, while the results of the unfolding procedure are presented in Chapter 9.

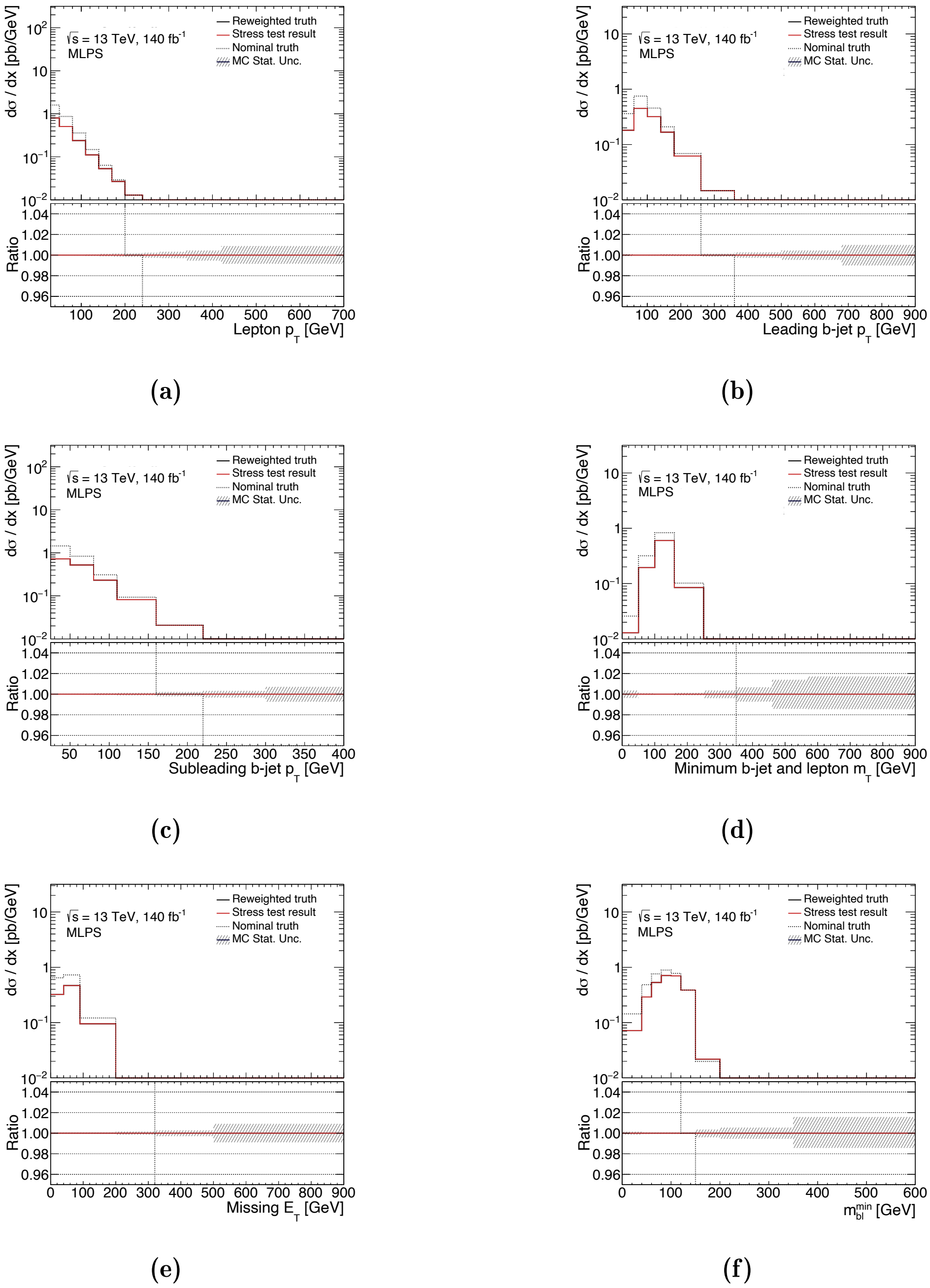

Figure 7.7: Linear test for the measurement-like phase space: a lepton p_T distribution, b leading b-jet p_T distribution, c subleading b-jet p_T distribution, d $m_T^{min}(bl)$ distribution, e E_T^{miss} distribution, f m_{bl}^{min} distribution.

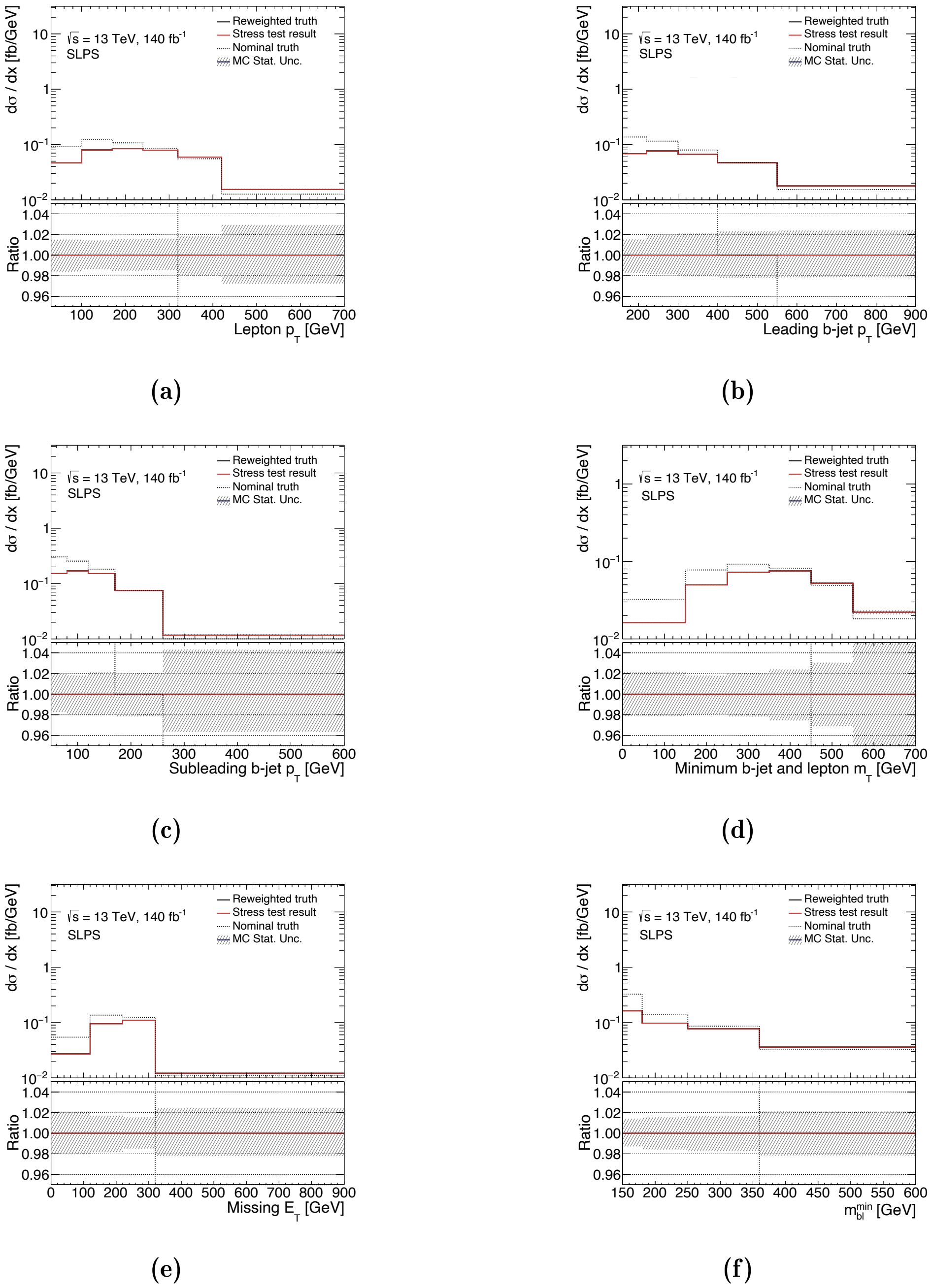

Figure 7.8: Linear test for the search-like phase space of the analysis: a lepton p_T distribution, b leading b-jet p_T distribution, c subleading b-jet p_T distribution, d $m_T^{min}(bl)$ distribution, e E_T^{miss} distribution, f m_{bl}^{min} distribution.

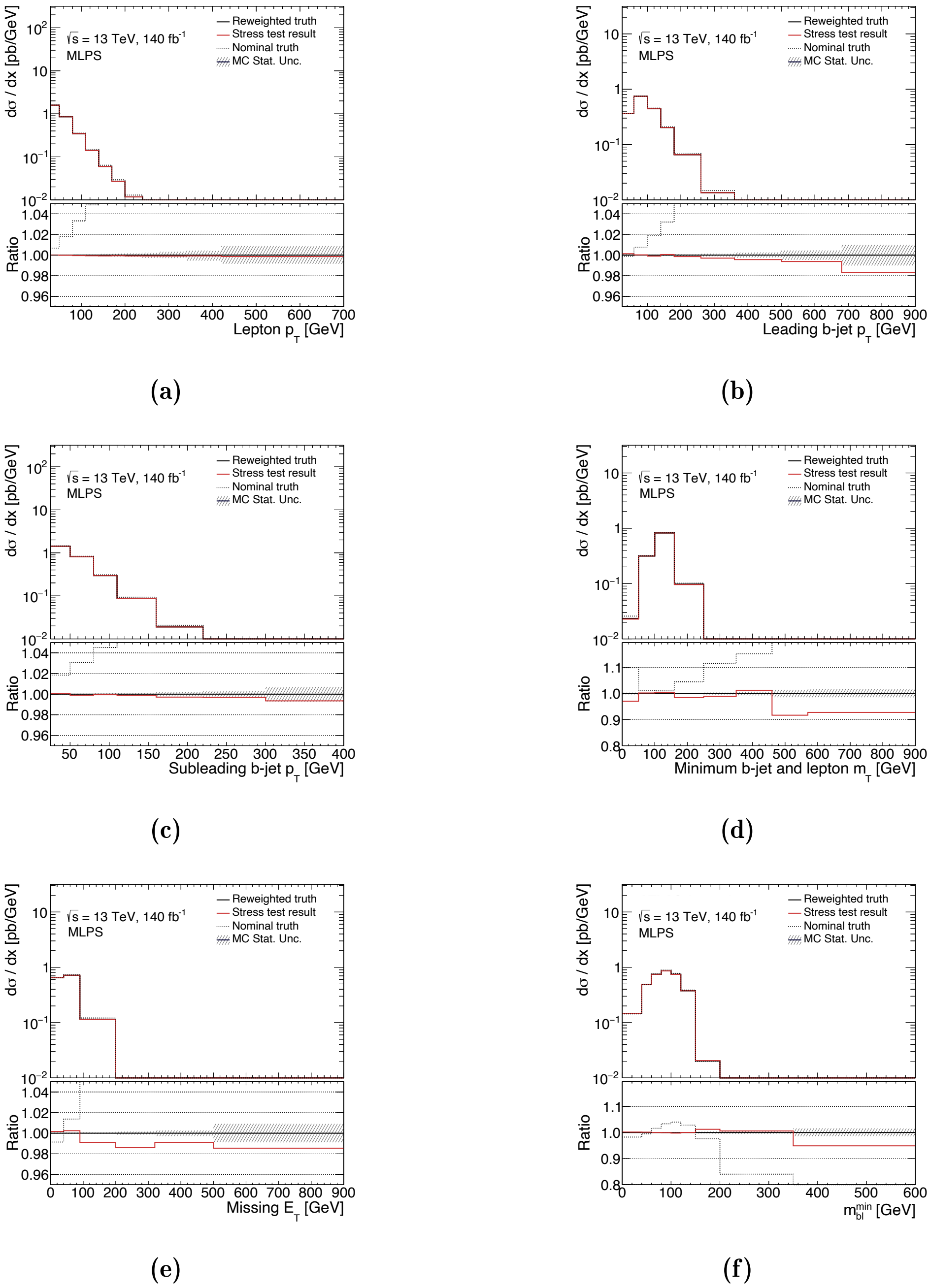

Figure 7.9: Data stress test for the measurement-like phase space: a lepton p_T distribution, b leading b-jet p_T distribution, c subleading b-jet p_T distribution, d $m_T^{min}(bl)$ distribution, e E_T^{miss} distribution, f m_{bl}^{min} distribution.

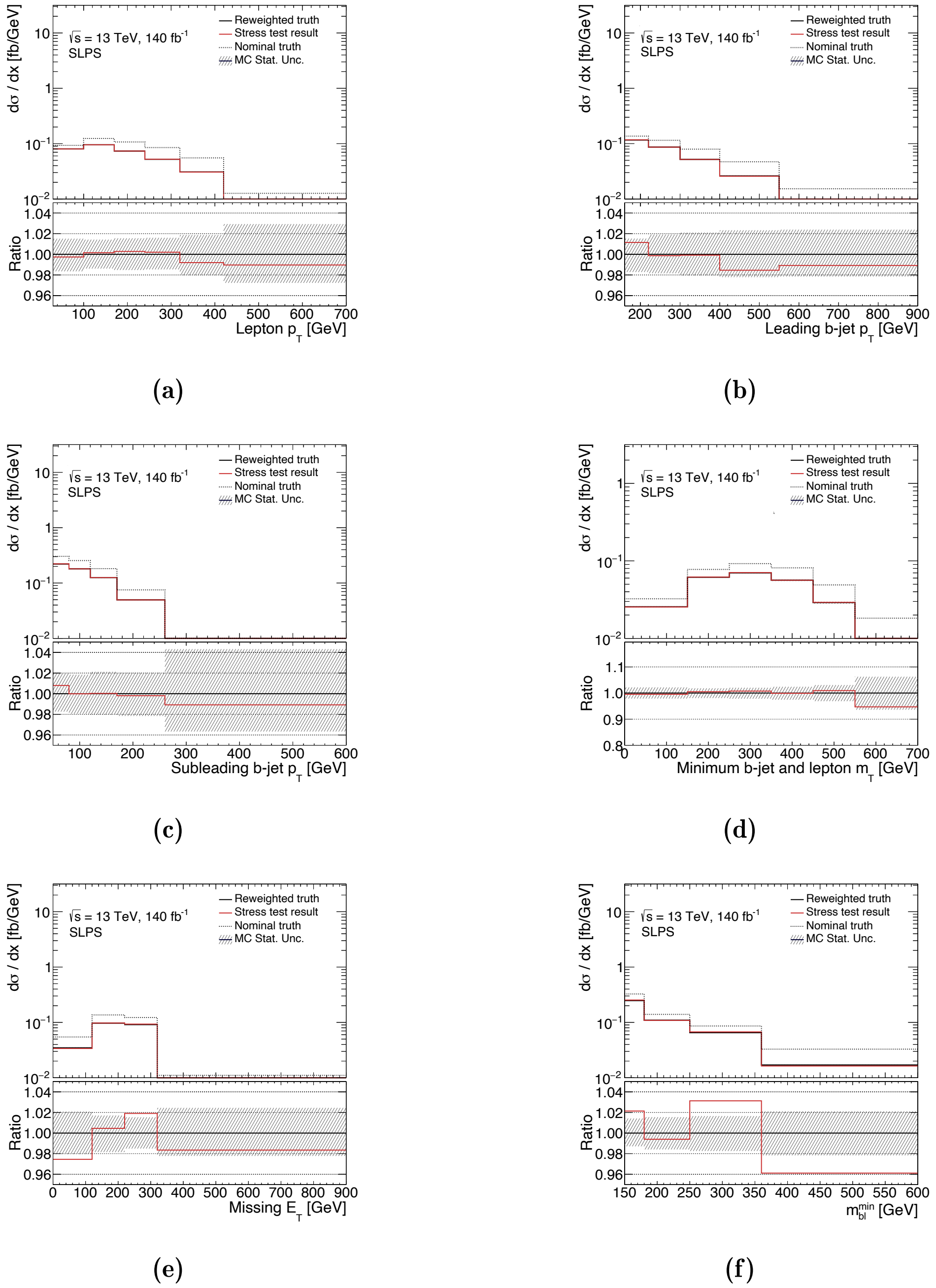

Figure 7.10: Data stress test for the search-like phase space of the analysis: a lepton p_T distribution, b leading b-jet p_T distribution, c subleading b-jet p_T distribution, d $m_T^{min}(bl)$ distribution, e E_T^{miss} distribution, f m_{bl}^{min} distribution.

8

Systematic Uncertainties

There are several sources of systematic uncertainties that can affect the measured unfolded differential cross-sections. The experimental systematics are briefly explained in Section 8.1, while the uncertainties associated with the modelling of the signal and background are discussed in Section 8.2. The uncertainties related to the background and to data and Monte Carlo statistics are discussed in Sections 8.3 and 8.4, respectively. The recommendations for these uncertainties are provided by ATLAS performance groups, which suggest a proper treatment for each uncertainty. Finally, the propagation of these uncertainties through the unfolding procedure is discussed in Section 8.5.

8.1 Experimental systematics uncertainties

The detector uncertainties considered in the analysis presented in this thesis are: leptons, jets, b-tagging, missing transverse energy and pile-up modelling. These uncertainties are appliedmas a re-scaling factor in the energy and momentum of the selected physics objects.

8.1.1 Leptons

Both electrons and muons have uncertainties associated with the energy and momentum scale and resolution, as outlined in Sections 5.2 and 5.3. These variations modify the momentum of the leptons. The calibration of lepton momentum reconstruction and identification introduces uncertainties, which are then propagated changing the scale factors of the leptons. In a similar way, the scale factors for the trigger efficiencies are varied to account for uncertainties in the measurements of the trigger efficiencies of the lepton triggers [137] [138].

8.1.2 Jets

The impact of the systematic uncertainties related to jets [140] arise from the calibration of the jet energy scale [164] and resolution [164], as detailed in Section 5.4. The uncertainties are estimated by varying the jet energies according to the uncertainties derived from Monte Carlo simulation and in-situ calibration measurements [165].

8.1.3 *b*-tagging

The calibration of b-tagging efficiency and mis-tagging rates derived from the simulation is modified to match the values observed in the real data [166]. Uncertainties resulting from this procedure are taken into account in the presented analysis. The primary sources of uncertainty in the calibration procedure are attributed to the modelling of the Standard Model processes, the limited number of simulated and observed events, and the calibration of the jet energy scale.

8.1.4 Missing transverse energy

The uncertainties on the energy scales and resolutions of the reconstructed leptons and jets are propagated in a correlated way to the missing transverse momentum [155]. In addition, there are scale and resolution uncertainties associated with the soft term [167]. These uncertainties introduce modifications to both the magnitude and direction of the missing transverse momentum vector.

8.1.5 Luminosity and pile-up

Further sources of experimental uncertainties arise from the measurement of the integrated luminosity and the correction of the number of pile-up collisions to data in simulated events. The uncertainty on the full Run-2 integrated luminosity is 0.82% [168], obtained using the LUCID-2 detector [169] for the primary luminosity measurements, complemented by measurements using the inner detector and calorimeters. The uncertainty on the re-weighting procedure is used to correct the Monte Carlo pile-up profile to match the data.

8.1.6 Detector-level breakdown

Figures 8.1 and 8.2 show a detailed breakdown of the detector systematic uncertainties for the measurement-like and search-like phase spaces, respectively. The figures show the relative uncertainties for lepton p_T (top left), leading b-jet p_T (top right), E_T^{miss} (bottom left) and m_{bl}^{min} (bottom right). Each type of uncertainty is represented by a different colour, while the total uncertainty represented by a solid black line. The total uncertainty is calculated as the sum in squares of the individual contributions. In both phase spaces the uncertainties do not exceed 12%, at most. The main contribution to the total uncertainty is given by the Jet Energy Scale uncertainty (solid red line), for both the measurement-like and the search-like phase spaces. In both cases, the uncertainty is of the order of 4%, except for the m_{bl}^{min} variable, where it reaches 10%. In addition, the b tagging efficiency (solid green line) also makes a significant contribution, for the lepton p_T and the leading b jet p_T in the measurement-like phase space.

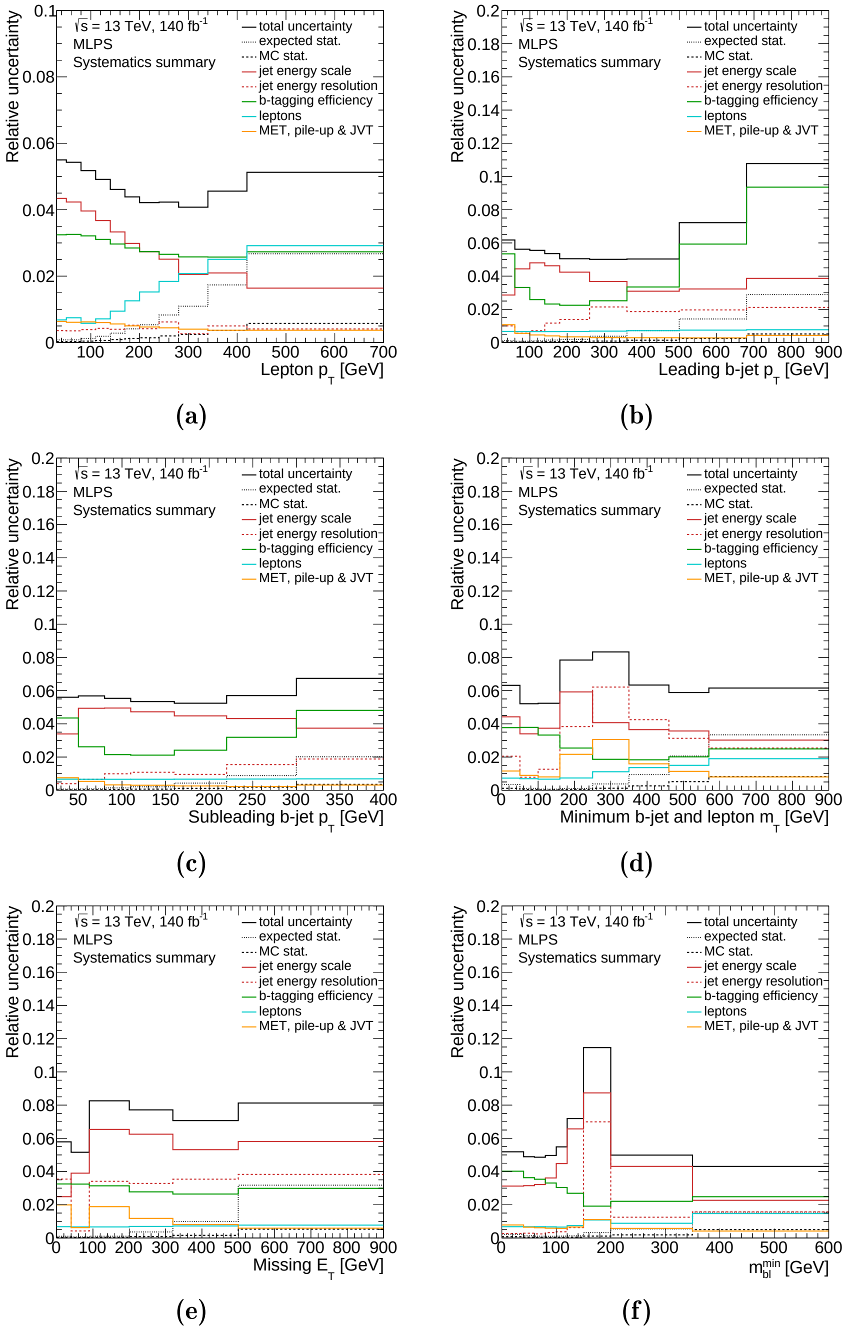

(a) (b) (c) (d) (e) (f)

Figure 8.1: Breakdown of detector uncertainties for the measurement-like phase space: a lepton p_T distribution, b leading b-jet p_T distribution, c subleading b-jet p_T distribution, d $m_T^{min}(bl)$ distribution, e E_T^{miss} distribution, f m_{bl}^{min} distribution. The total uncertainties is shown in black and the single contributions are shown in different colors.

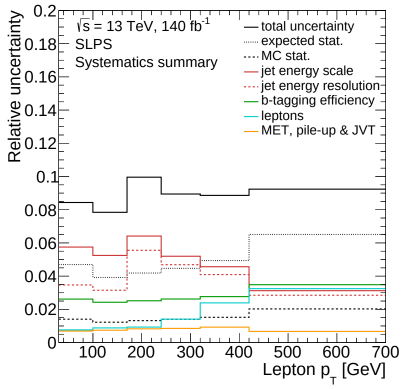

(a)

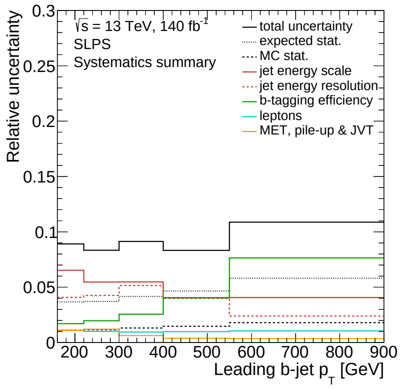

(b)

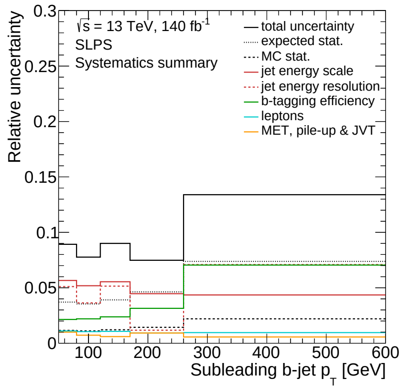

(c)

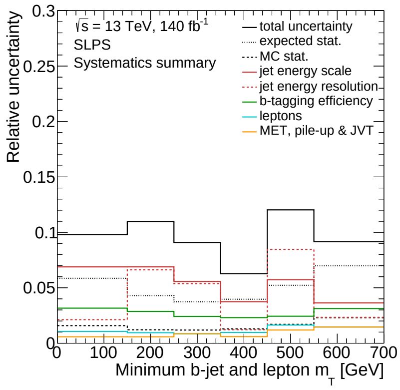

(d)

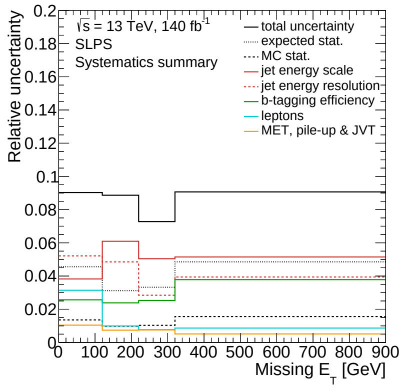

(e)

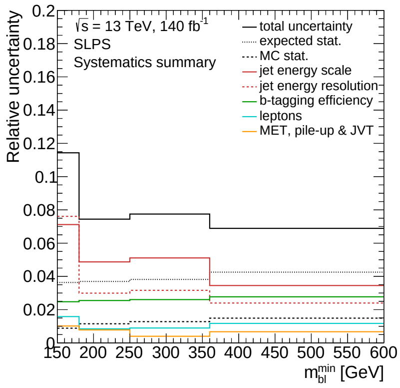

(f)

Figure 8.2: Breakdown of detector uncertainties for the search-like phase space: a lepton p_T distribution, b leading b-jet p_T distribution, c subleading b-jet p_T distribution, d $m_T^{min}(bl)$ distribution, e E_T^{miss} distribution, f m_{bl}^{min} distribution. The total uncertainties is shown in black and the single contributions are shown in different colors.

8.2 Modelling systematic uncertainties

The limited understanding of how the generators model the signal processes is a significant source of uncertainty. The impact of this type of uncertainty has been assessed using alternative predictions described in Section 4.4.2.

8.2.1 Cross-section

In this analysis the $t\bar{t}$ and tWb samples are combined together with their independent normalisations. To account for possible fractional differences due to cross-section uncertainties, the $t\bar{t}$ and tW cross sectional uncertainties are anti-correlated and this is applied as the uncertainty.

8.2.2 Hadronisation model

The uncertainty due to the choice of the hadronisation model and other non-perturbative aspects of the parton shower is evaluated using the `Powheg+Herwig7` sample.

8.2.3 Renormalisation and Factorisation Scales

Production cross-sections are computed with perturbation expansions as an approximation. This implies that the cross-section depends on the choice of the renormalisation and factorisation scales μ_R and μ_F, respectively, for both the hard-scatter and showering processes. This is taken as an uncertainty by varying the default scales ($\mu_R = 0.5(2.0)$ and $\mu_F = 0.5(2.0)$) using the nominal generator and taking the differences of the obtained cross-section [170].

8.2.4 h_{damp}

The h_{damp} parameter controls the Matrix Element/Parton Shower matching in `Powheg` and regulates the high p_T radiation. The estimation of this uncertainty is performed using a dedicated sample generated with `Powheg+Pythia8`, where the parameter h_{damp} is multiplied by a factor of $2 \cdot m_{top}$ compared to its nominal value ($h_{damp} = 1.5 \cdot m_{top}$) [171].

8.2.5 Matrix-element Matching

This uncertainty accounts for the fact that the modelling of the top-quark processes involves the matching of the next-to-leading order Monte Carlo calculation of the hard-scatter provided by `Powheg` to the parton shower provided by `Pythia`. The matching procedure connects the hard-scatter generator to the parton shower such that it includes the full evolution of the event, without leaving holes or double counting in the regions of the radiation phase space. The estimation of this uncertainty is based on the p_T^{hard} parameter, which regulates how the `Pythia` phase space is determined. The approach used in the matching between `Powheg` and `Pythia` is called *vetoed shower*, where `Pythia` generates emissions in the full phase space but vetoes the emissions in regions of the phase space already covered by `Powheg` [172]. This uncertainty is assessed by comparing an alternative sample obtained setting the p_T^{hard} parameter in `Pythia` to 1 and comparing it to the nominal sample, in which the parameter is set to 0.

8.2.6 Recoil to top

As the top quark decays to a b-quark and a W-boson, gluon emission can occur. The modelling of the subsequent showers determines how accurately the original top quark can be reconstructed, therefore the changes in the gluon emission modelling impact all coloured resonance decays. Gluon emission results in a change in energy-momentum of the decay products, however this has to be distributed to other particles in the system to ensure that conservation laws are preserved. For this reason, the choice of the gluon's particle of origin is important, as it affects the emission phase space. The default samples uses the recoiling against b-quarks, deciding how the momentum is re-arranged between the W-boson and the b. This uncertainty compares the nominal sample with the sample in which the top-quark itself acts as a recoiling object for the second and subsequent emissions. This is the modelling uncertainty in which only the top pair component of the signal is modified.

8.2.7 Top-quark mass

The top-quark mass is known with a precision of about 0.5 GeV [173]. This has implications for the analysis as the kinematics of the decay products, and hence the probability of passing the selection requirements, depend on the top-quark mass. To estimate the uncertainty, two additional simulated samples are used with varied top-quark mass values of 169 GeV and 176 GeV. Except for the top-quark mass, these samples have the same setup as the nominal $t\bar{t}$ and tW samples. The final uncertainty is then scaled by 1/7 to match the effect of a ± 0.5 GeV shift in the top-quark mass. The uncertainty of 0.5 GeV is determined from events in the full phase space. Since the top-quark mass is Lorentz invariant, it is appropriate to apply this top-quark mass value and uncertainty to the limited phase space used in the analysis.

8.2.8 PDF

The efficiency, acceptance, and possibly the response matrix are modified by selecting a different PDF. To evaluate the influence of different PDF sets, a re-weighting procedure is applied to the nominal `Powheg+Pythia8` $t\bar{t}$ and tW samples. This procedure follows the `PDFforLHC15` prescription [174] and uses the `LHAPDF` tool [175].

8.2.9 tW Diagram Removal and Diagram Subtraction

Another component of the uncertainty is represented by the difference between the diagram removal (DR) and diagram subtraction (DS) schemes, used to remove the overlap between the $t\bar{t}$ and tW productions, as explained in Section 2.3.3. This uncertainty specifically affects the tW component of the signal. The uncertainty estimate is derived by considering the envelope of all the alternative tW DR/DS samples, while keeping the $t\bar{t}$ component fixed at its nominal value.

8.2.10 Modelling Breakdown

Figures 8.3 and 8.4 show a detailed breakdown of the theory systematic uncertainty for the measurement and search phase spaces, respectively. The figures show the relative uncertainties for lepton p_T (top left), leading b-jet p_T (top right), E_T^{miss} (bottom left) and m_{bl}^{min} (bottom right). Each type of uncertainty is represented by a different colour, while the total uncertainty represented by a solid black line. The total uncertainty is calculated as the sum in squares of the individual contributions. In the measurement-like phase space the total uncertainty doesn't exceed 50%, while in the search-like phase space it reaches 80%. The largest contribution to the theory uncertainties comes from the factorisation and renormalisation scales (dashed green line) in the measurement-like phase space and from the tW DR vs DS uncertainty (solid red line), for the search-like phase space.

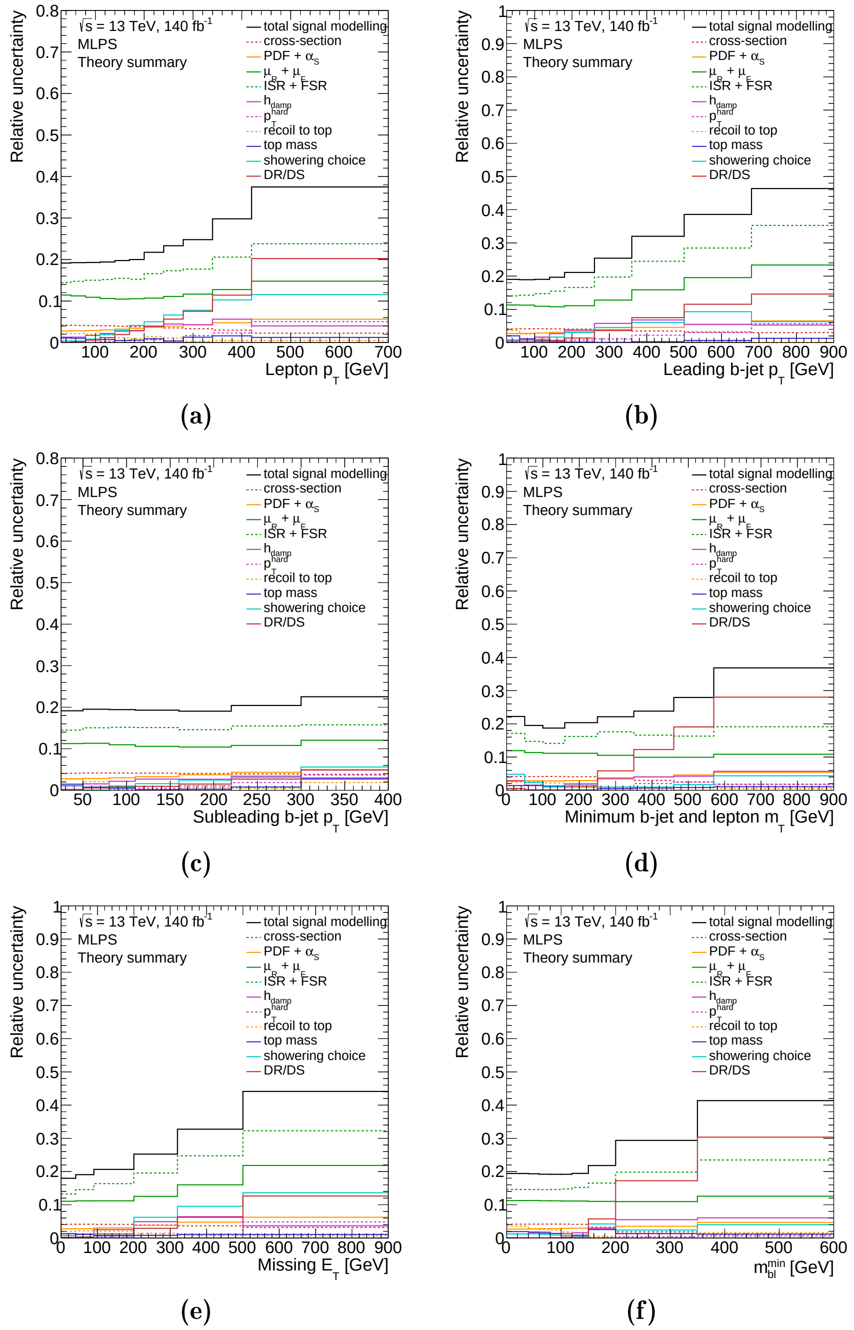

Figure 8.3: Theory uncertainty breakdown for the measurement-like phase space: a lepton p_T distribution, b leading b-jet p_T distribution, c subleading b-jet p_T distribution, d $m_T^{min}(bl)$ distribution, e E_T^{miss} distribution, f m_{bl}^{min} distribution. The total uncertainties is shown in black and the single contributions are shown in different colors.

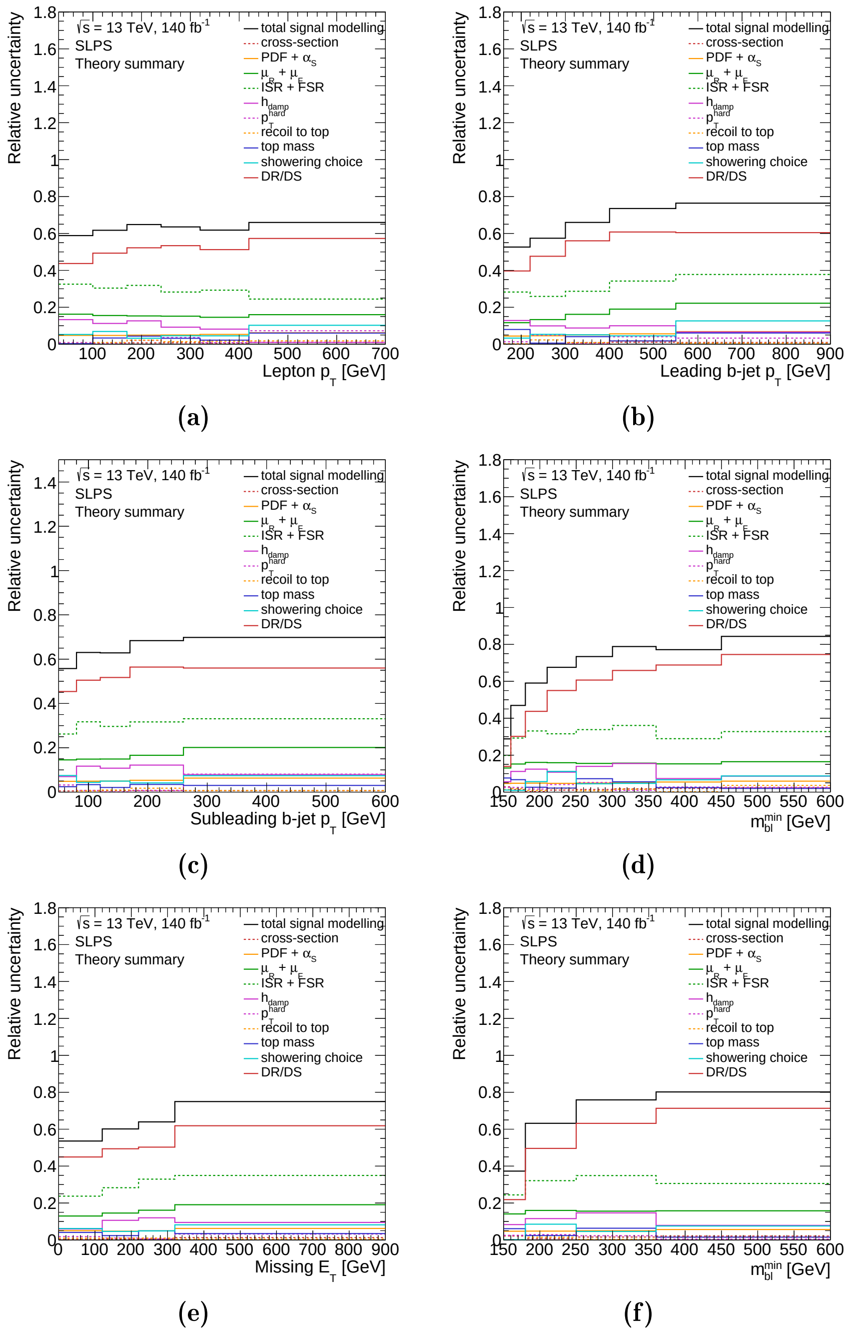

Figure 8.4: Theory uncertainty breakdown for the search-like phase space: a lepton p_T distribution, b leading b-jet p_T distribution, c subleading b-jet p_T distribution, d $m_T^{min}(bl)$ distribution, e E_T^{miss} distribution, f m_{bl}^{min} distribution. The total uncertainties is shown in black and the single contributions are shown in different colors.

8.3 Uncertainties on the background processes

Multiple backgrounds affect the measurement, resulting in the presence of multiple associated uncertainties.

8.3.1 W+jets

The full detector uncertainties and the modelling uncertainties on PDFs, scales and electroweak corrections are applied similarly to the signal sample. A likelihood fit is then performed in a dedicated control region to constrain the normalisation effects of each uncertainty and to split the shape and normalisation effects. Further details are described in Section 6.5.1.

8.3.2 Background from fake and non-prompt leptons

Two uncertainties are assigned to the fake and non-prompt lepton background, separately for electrons and muons. They are derived from variations in the selection of fake estimates and are described in more detail in Section 6.5.2.

8.3.3 Other background processes

Additional background processes collectively contribute less than 5% of the total yield in the regions and have a minimal impact on the overall uncertainty. Scale, PDF and electroweak uncertainties are applied to the *Other-V* samples (described in Ch. 4), while only a conservative 25% normalisation uncertainty is applied to the *Other-t* samples (described in Ch. 4).

8.4 Finite MC and data sample statistics

To account for the limited statistics of the Monte Carlo and data samples, pseudo-experiments are used to evaluate the impact of finite statistics. Figures 8.5 and 8.6 show the Monte Carlo (dotted black line) and expected data statistical (dotted black line) uncertainties, respectively. Overall, the total uncertainty is of the order of 3% and 6% at most, for the measurement-like and search-like phase space. The major contribution to the total uncertainty, in both regions, is given by the expected data statistical uncertainty.

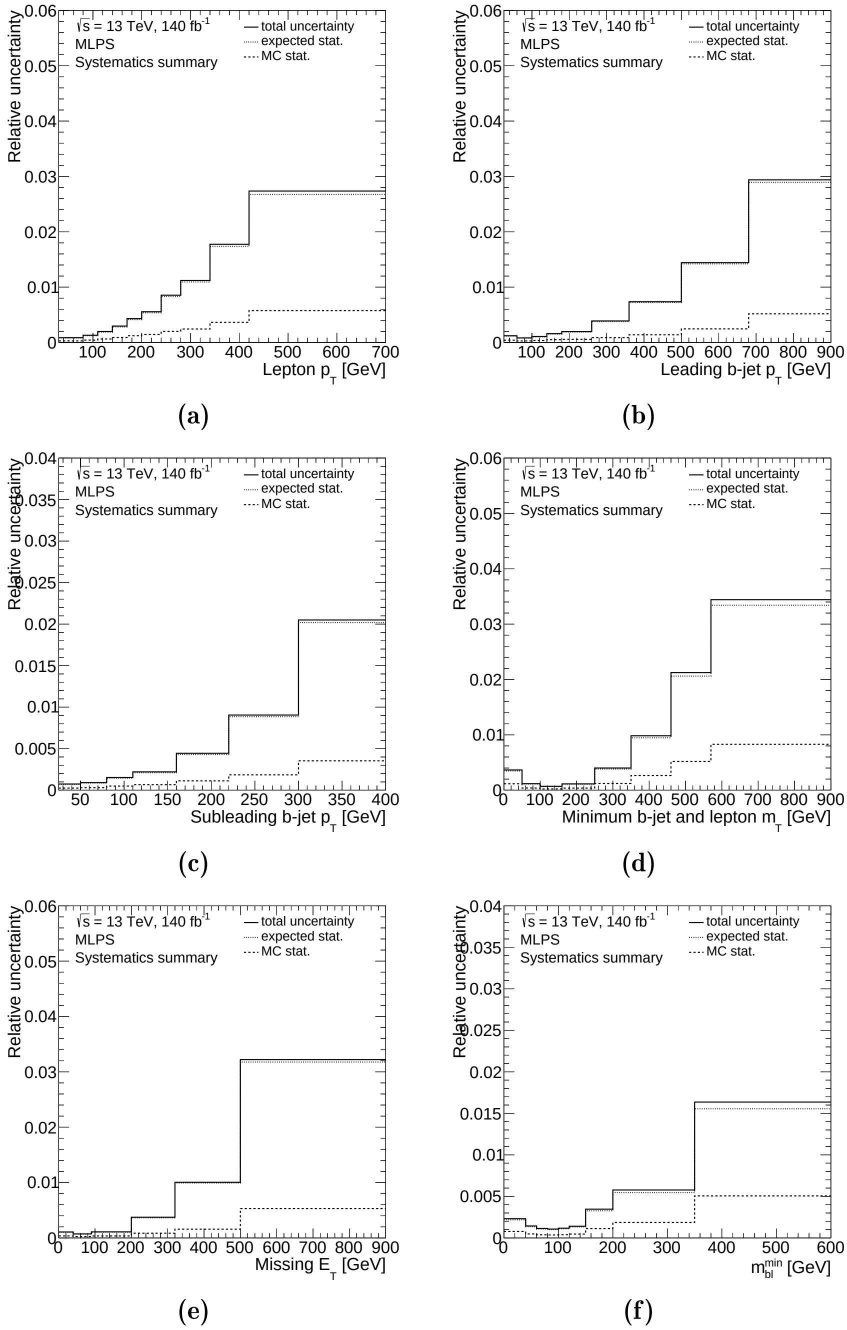

Figure 8.5: Statistical uncertainty breakdown for the measurement-like phase space: a lepton p_T distribution, b leading b-jet p_T distribution, c subleading b-jet p_T distribution, d $m_T^{min}(bl)$ distribution, e E_T^{miss} distribution, f m_{bl}^{min} distribution. The total uncertainty is represented by the full black line, the expected statistical uncertainty by the black dotted line and the Monte Carlo statistical uncertainty is represented by the dashed black like.

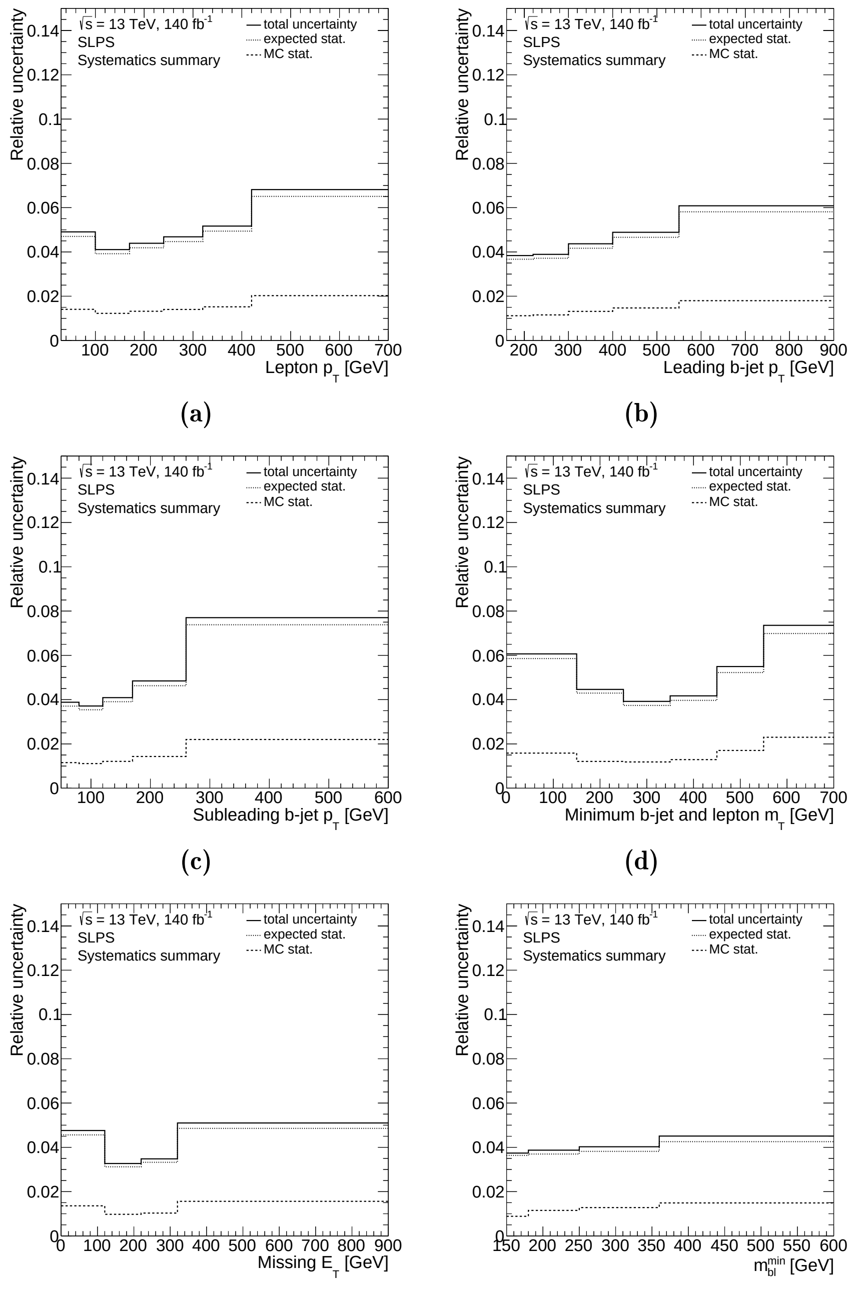

Figure 8.6: Statistical uncertainty breakdown for the search-like phase space: a lepton p_T distribution, b leading b-jet p_T distribution, c subleading b-jet p_T distribution, d $m_T^{min}(bl)$ distribution, e E_T^{miss} distribution, f m_{bl}^{min} distribution. The total uncertainty is represented by the full black line, the expected statistical uncertainty by the black dotted line and the Monte Carlo statistical uncertainty is represented by the dashed black like.

8.5 Uncertainty propagation through unfolding

Each systematic uncertainty is evaluated at detector-level and then propagated through the unfolding procedure (described in Chapter 7). Deviations from the nominal predictions are evaluated separately for the upward and downward variations for each bin of each observable, combining the electron and muon channels.

Pre-unfolding shifts are used to propagate uncertainties associated with the limited amount of data and Monte Carlo statistics, detector systematics and background modelling.

As described in Chapter 7, the unfolded spectrum $N_{t,i}$ can be expressed as

$$N_{t,i} = \frac{1}{\epsilon_{k,i}} \cdot \sum_j M^{-1}_{i,j} \mathrm{A}^{k,j} (N_{d,j} - N_{b,j}) \tag{8.1}$$

The variables $\epsilon_{k,i}$, $M_{i,j}$, and $\mathrm{A}^{\mathrm{k,j}}$ correspond to the unfolding corrections. $N_{d,j}$ and $N_{b,j}$ represent the data and the backgrounds, respectively.

The experimental and theoretical systematic uncertainties are evaluated using up and down variations at detector level, which are propagated to particle level. The up and down uncertainties resulting from individual uncertainties are then combined at particle level, by adding them in quadrature, assuming no correlation:

$$\sigma^{\mathrm{up/down}}_{\mathrm{tot}} = \sqrt{\sum_{\mathrm{sys}} (\sigma^{\mathrm{up/down}}_{\mathrm{sys,rel}})^2} \tag{8.2}$$

If an uncertainty is one-sided, it is symmetrized at the reconstruction level and the two resulting up/down variations are propagated to the particle level.

Depending on the type of uncertainty, different propagation procedures are used, as described in the following sections.

8.5.1 Experimental systematic uncertainties

The propagation of the detector systematic uncertainties is based on the shift of the unfolding corrections (acceptance, efficiency and migration matrix) and the expected background, while keeping the data constant:

$$N'_{t,i} = \frac{1}{\epsilon'_{k,i}} \cdot \sum_j {M^{-1}}'_{i,j} A'^{k,j} \left(N_{d,j} - N'_{b,j}\right), \tag{8.3}$$

In the equation, primed quantities indicate varied quantities.

The data is then unfolded with these varied corrections and the difference to the nominal unfolded data defines the uncertainty σ:

$$\sigma_{\text{exp.sys.}} = N_{t,i} - N^{'}_{t,i} \tag{8.4}$$

The described technique has been used for the evaluation of systematic uncertainties in this thesis. Other techniques have been considered, but the results are consistent within the different techniques.

Figures 8.7 and 8.8 show a detailed breakdown of the detector systematics for the measurement-like and search-like phase spaces, respectively, after the unfolding procedure. The figures show the relative uncertainties for lepton p_T (top left), leading b-jet p_T (top right), E_T^{miss} (bottom left) and m_{bl}^{min} (bottom right). Each type of uncertainty is represented by a different colour, with the total uncertainty represented by the black line. The total uncertainty is calculated as the sum of the squares of the individual contributions. In both phase spaces the uncertainties do not exceed 15% at most, except for the variable m_{bl}^{min}. This is attributed to the transition region between the resonant $t\bar{t}$ and resonant tW diagrams in the bin between 150 GeV and 200 GeV, where m_{bl}^{min} shows sensitivity. The main source of uncertainty in the detector uncertainties is still the Jet Energy Scale uncertainty (full red line) for the measurement-like phase space. For the search-like phase space the major contribution is the data statistics (black dotted line).

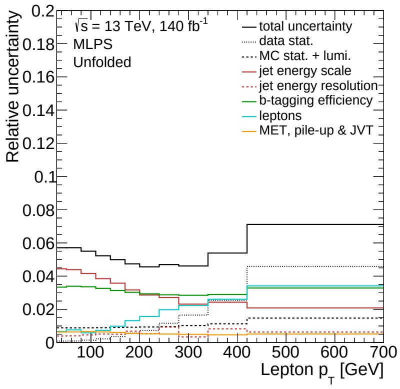

(a)

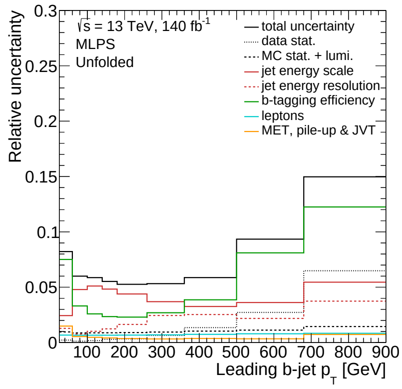

(b)

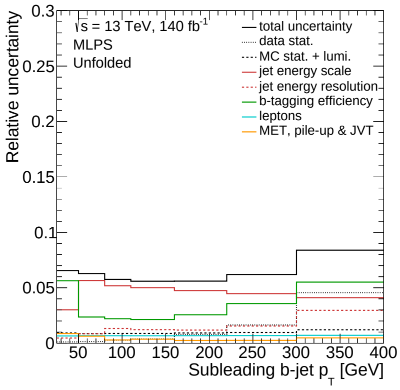

(c)

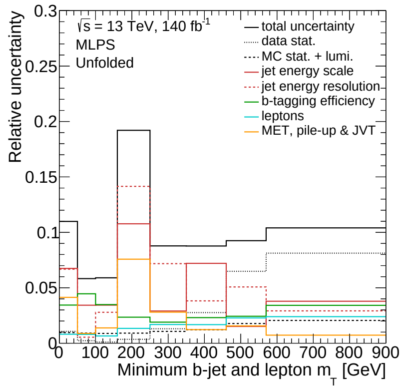

(d)

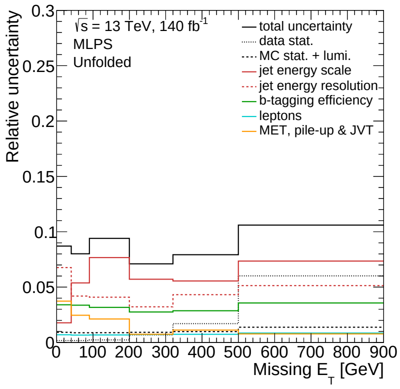

(e)

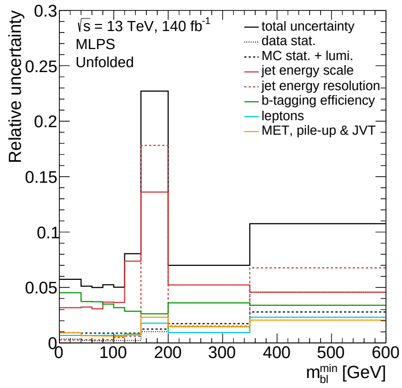

(f)

Figure 8.7: Post-unfolding detector systematic breakdown for the measurement-like phase space: a lepton p_T distribution, b leading b-jet p_T distribution, c subleading b-jet p_T distribution, d $m_T^{min}(bl)$ distribution, e E_T^{miss} distribution, f m_{bl}^{min} distribution. The total uncertainties is shown in black and the single contributions are shown in different colors.

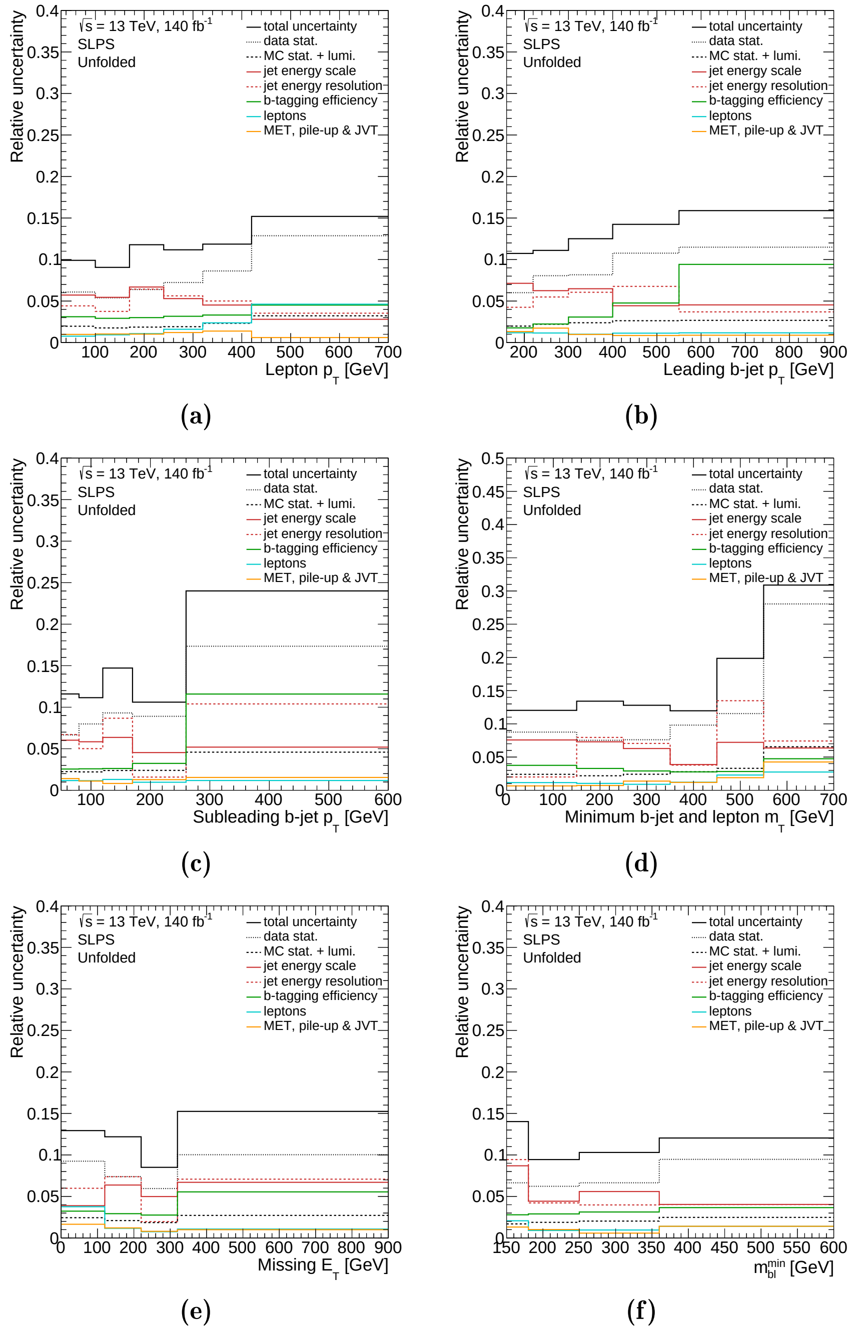

Figure 8.8: Post-unfolding detector systematic breakdown for the search-like phase space: a lepton p_T distribution, b leading b-jet p_T distribution, c subleading b-jet p_T distribution, d $m_T^{min}(bl)$ distribution, e E_T^{miss} distribution, f m_{bl}^{min} distribution. The total uncertainties is shown in black and the single contributions are shown in different colors.

8.5.2 Modelling systematic uncertainties

The propagation of the signal modelling uncertainties is also based on the upwards/downwards variations.

The modelling uncertainties are implemented as follows:

- Unfold nominal *pseudo-data* $N_{pd,j}$, where $N_{pd,j} = N_{r,j} + N_{b,j}$, calculated using Monte Carlo quantities, using varied migration matrix, acceptance and efficiency

$$N'_{t,i} = \frac{1}{\epsilon'_i} \cdot \sum_j {M^{-1}}'_{i,j} A'^{k,j} \left[N_{pd,j} - N'_{b,j}\right] \tag{8.5}$$

- Compare the result with Monte Carlo nominal truth, N_t

$$\sigma_{\text{sig.mod.}} = N_t - N'_t \tag{8.6}$$

- Use this uncertainty as uncertainty on the unfolded data.

Figures 8.9 and 8.10 show a detailed breakdown of the theory systematics for the measurement-like and search-like phase spaces, respectively, after the unfolding. The figures show the relative uncertainties for lepton p_T (top left), leading b-jet p_T (top right), E_T^{miss} (bottom left) and m_{bl}^{min} (bottom right). Each type of uncertainty is represented by a different colour, while the total uncertainty represented by the solid black line. The total uncertainty is calculated as the sum in squares of the individual contributions. In the measurement-like phase space the main contributions to the total uncertainty are the showering choice (solid cyan line) and the tW DR vs DS uncertainty (solid red line), whereas for the search-like phase space the total uncertainty comes only from the tW DR vs DS uncertainty.

The uncertainty in the DR vs DS comparison is significant due to the fact that the unfolding process not only corrects for detector effects, but also for the out of acceptance contributions in the unfolding phase space. To address this issue, a Monte Carlo simulation is required to estimate the out-of-acceptance migrations, which are then corrected during the unfolding process. When implementing a cut at $m_{bl}^{min} > 150\,\text{GeV}$, there is a risk of $t\bar{t}$ events moving from the on-shell to the off-shell regime due to resolution effects, and this effect needs to be accounted for using Monte Carlo modelling. However, the Monte Carlo simulations do not accurately represent the data, resulting in a high sensitivity of the unfolding process to the Monte Carlo modelling and the off-shell migrations. This sensitivity is particularly relevant in the context of the DR vs DS comparison, as the choice to rely on a particular Monte Carlo simulation, in this case the DR simulation, can have a significant impact on the results.

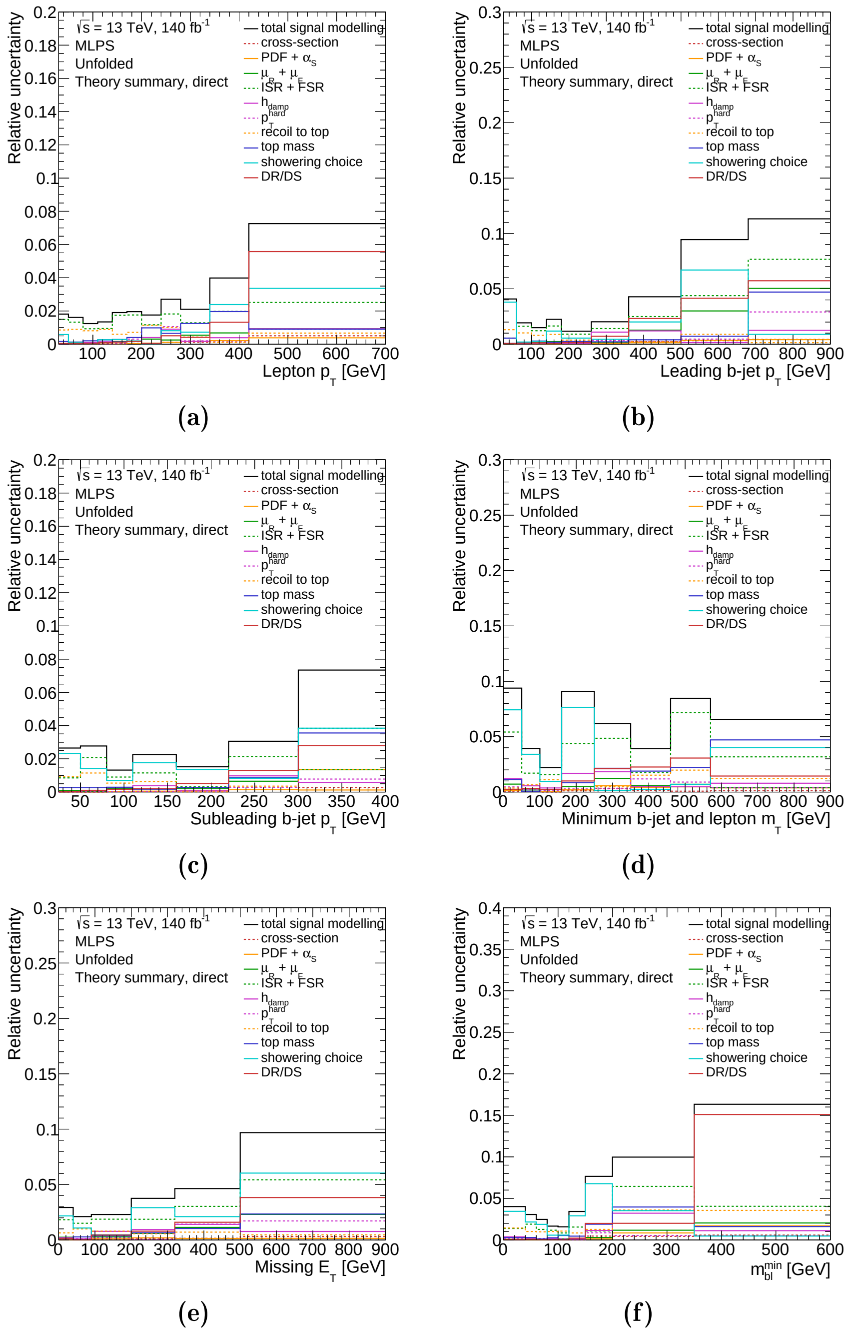

Figure 8.9: Post-unfolding theory systematic breakdown for the measurement-like phase space: a lepton p_T distribution, b leading b-jet p_T distribution, c subleading b-jet p_T distribution, d $m_T^{min}(bl)$ distribution, e E_T^{miss} distribution, f m_{bl}^{min} distribution. The total uncertainties is shown in black and the single contributions are shown in different colors.

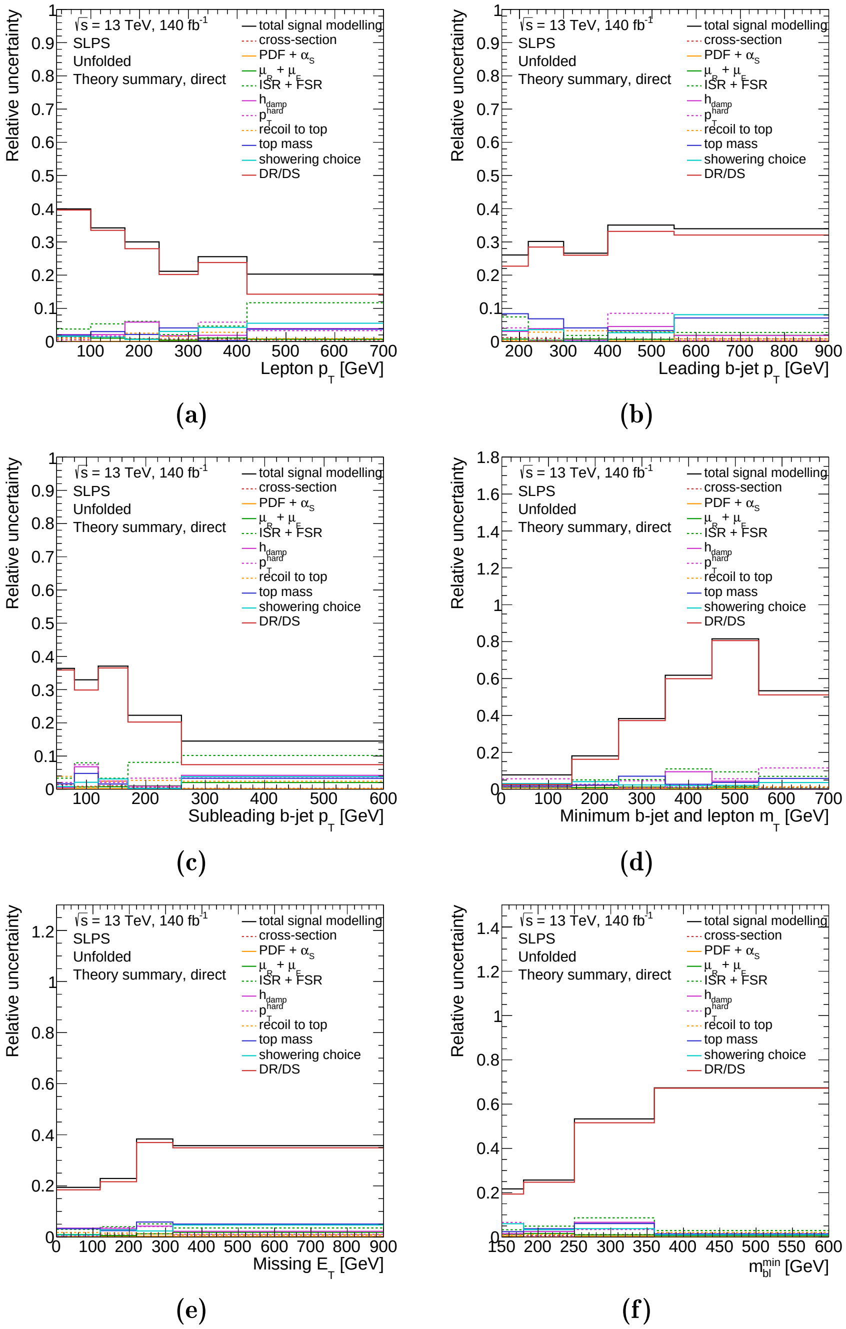

Figure 8.10: Post-unfolding theory systematic breakdown for the search-like phase space: a lepton p_T distribution, b leading b-jet p_T distribution, c subleading b-jet p_T distribution, d $m_T^{min}(bl)$ distribution, e E_T^{miss} distribution, f m_{bl}^{min} distribution. The total uncertainties is shown in black and the single contributions are shown in different colors.

8.5.3 Background modelling

Uncertainties affecting the modelling of the background are propagated to the unfolded result by varying the background prediction, while preserving all other unfolding corrections and unfolding the data:

$$N'_{t,i} = \frac{1}{\epsilon_{k,i}} \cdot \sum_j M^{-1}{}_{i,j} A_{k,j} \left(N_{d,j} - N'_{b,j} \right) \tag{8.7}$$

Such that

$$\sigma_{\text{bkg.mod.}} = N_{t,i} - N'_{t,i} \tag{8.8}$$

8.5.4 Data and Monte Carlo statistical uncertainty

Data The uncertainty due to the data statistics is propagated through the unfolding by creating $N_{pseudo-exp} = 10000$ Poisson smeared pseudo-experiments, which undergo through the unfolding procedure.

The shifting of data is defined as:

$$X_{\text{shift}} = X + \sigma_X \cdot x_{\text{pois}} \tag{8.9}$$

X is the number of events in the bin, σ_X is the standard deviation and x_{pois} is a Poisson random number. The final statistical uncertainty is evaluated from the standard deviation over all the toy distributions.

Monte Carlo The number of events in each bin is smeared by a Gaussian shift with mean equal to the yield of the bin, and standard deviation equal to the uncertainty of the bin. Then, the smeared spectrum is unfolded. The procedure is replicated for $N_{pseudo-exp} = 10000$ times, then the final statistical uncertainty is evaluated from the standard deviation over all the toy distributions.

Figures 8.11 and 8.12 show the Monte Carlo and expected data statistical uncertainties for the measurement-like and the search-like phase space, respectively, after unfolding. The resulting statistical uncertainty is found to be below 6%, for both analysis regions.

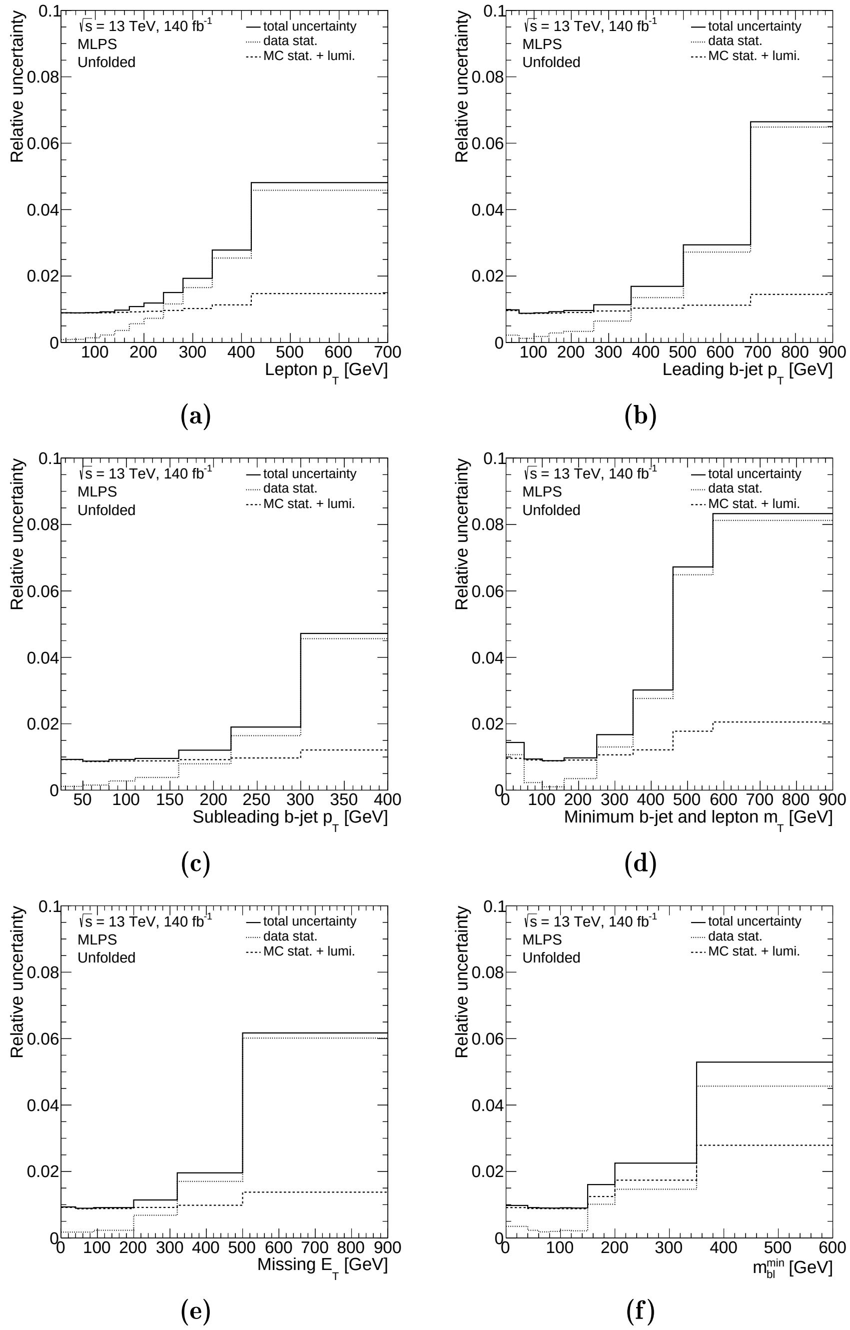

Figure 8.11: Post-unfolding statistical breakdown for the measurement-like phase space: a lepton p_T distribution, b leading b-jet p_T distribution, c subleading b-jet p_T distribution, d $m_T^{min}(bl)$ distribution, e E_T^{miss} distribution, f m_{bl}^{min} distribution. The total uncertainty is represented by the full black line, the expected statistical uncertainty by the black dotted line and the Monte Carlo statistical uncertainty is represented by the dashed black like.

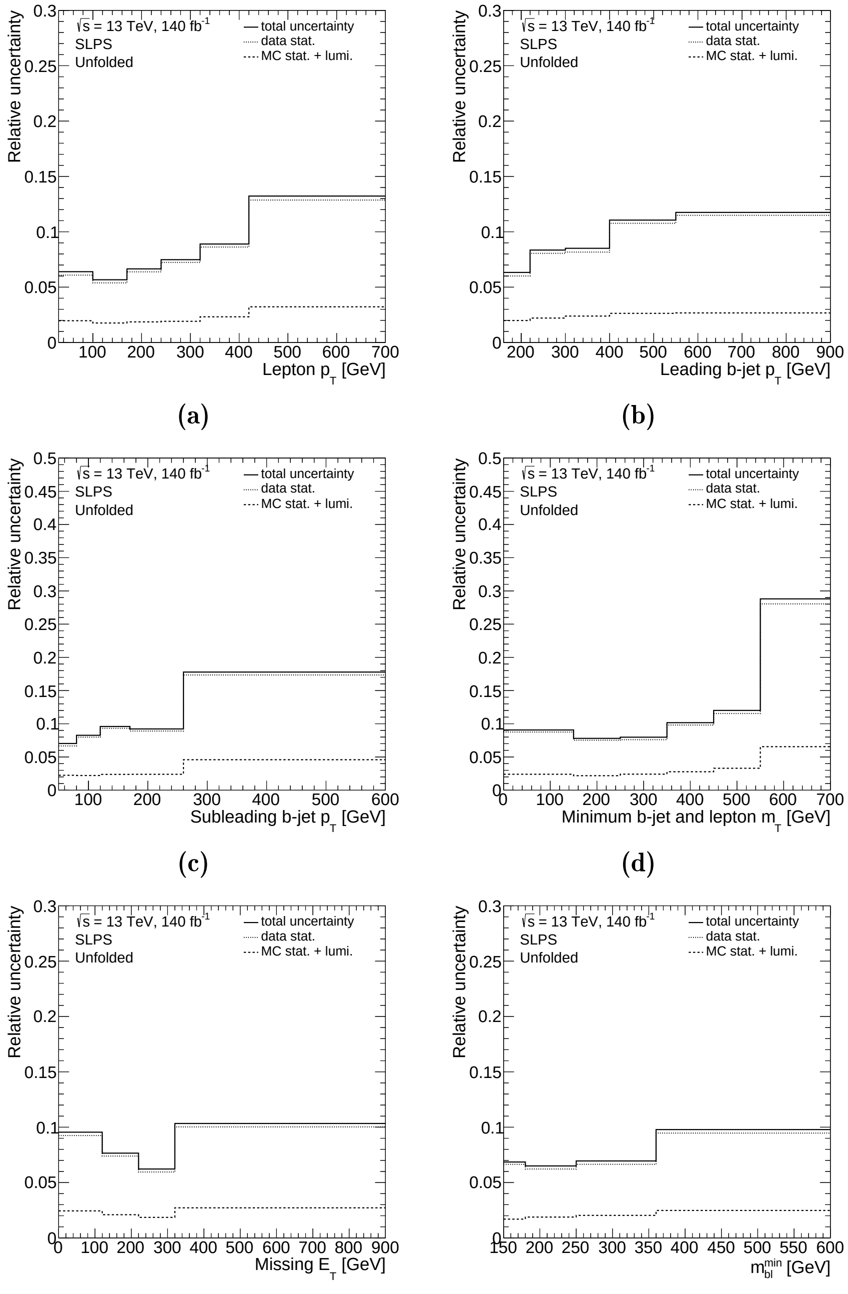

Figure 8.12: Post-unfolding statistical breakdown for the search-like phase space: a lepton p_T distribution, b leading b-jet p_T distribution, c subleading b-jet p_T distribution, d $m_T^{min}(bl)$ distribution, e E_T^{miss} distribution, f m_{bl}^{min} distribution. The total uncertainty is represented by the full black line, the expected statistical uncertainty by the black dotted line and the Monte Carlo statistical uncertainty is represented by the dashed black like.

8.6 Total Systematics Breakdown

Figures 8.13 and 8.14 show the total systematic breakdown post-unfolding procedure for the measurement-like and searches-like phase space. The total uncertainty is calculated as the sum in squares of the single contributions. As in the figures shown in the previous sections, the total uncertainty is represented by a solid black line and the individual uncertainty contributions by different colours. For the measurement-like phase space the major contribution to the total uncertainty is given by the Jet Energy Scale (solid red line) uncertainty in the first bins of the distributions and by the signal modelling (solid blue line) uncertainty in the tails. Significant contributions are also given by fake factors (dotted yellow line) in the last bin of the lepton p_T and by the b-tagging efficiency (solid green line) in the last bins of the leading b-jet p_T variable. In the search-like phase space, the largest contribution to the total uncertainty comes from the signal modelling (solid blue line).

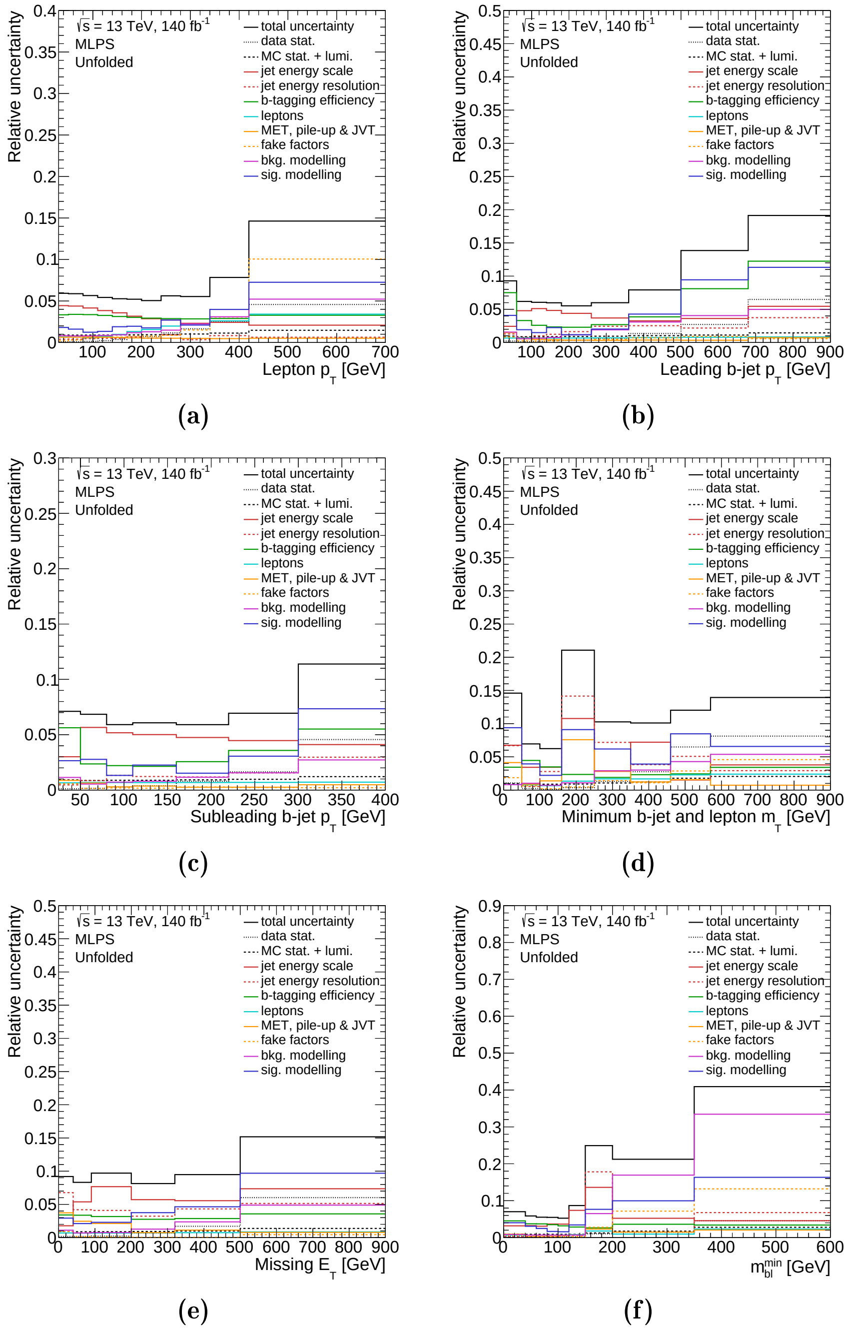

(a) (b) (c) (d) (e) (f)

Figure 8.13: Total uncertainties breakdown post-unfolding for the measurement-like phase space: a lepton p_T distribution, b leading b-jet p_T distribution, c subleading b-jet p_T distribution, d $m_T^{min}(bl)$ distribution, e E_T^{miss} distribution, f m_{bl}^{min} distribution.

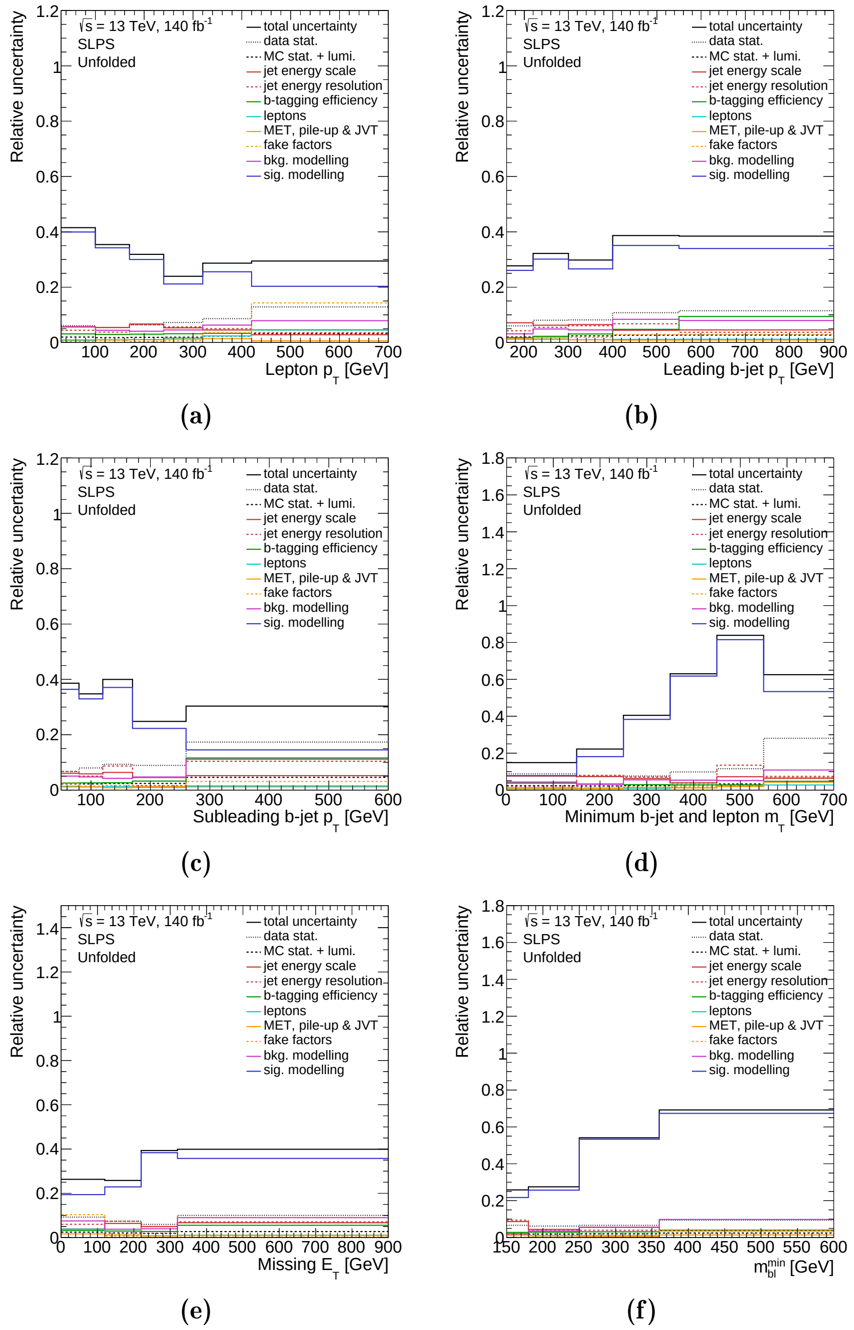

Figure 8.14: Total uncertainties breakdown post-unfolding for the search-like phase space: a lepton p_T distribution, c subleading b-jet p_T distribution, d $m_T^{min}(bl)$ distribution, b leading b-jet p_T distribution, e E_T^{miss} distribution, f m_{bl}^{min} distribution.

9
Results

This chapter presents the unfolded differential cross-sections in the measurement-like and search-like phase spaces, for the simple and compound variables, presented in Chapter 6. The unfolding procedure used to obtain the unfolded cross section is detailed in Chapter 7, and the associated uncertainties are determined according to the methodology outlined in Chapter 8. The unfolded data are then compared with the theoretical predictions discussed in Chapter 4. The data were collected by the ATLAS detector, described in Chapter 3, at the Large Hadron Collider (LHC) during LHC Run-2, covering the period from 2015 to 2018, at a centre-of-mass energy of $\sqrt{s} = 13\,\text{TeV}$.

The unfolded differential cross-sections are presented in Figure 9.1 and 9.2, for the measurement-like (MLPS) and search-like phase spaces (SLPS) respectively. The top panel in the figures shows the unfolded differential cross section of data (black dots) and generated Standard Model prediction (green and violet crosses) with their respective total uncertainties, displayed as a colored shaded area. There are two shaded areas: the dark grey shows the total uncertainty and the yellow comprises all the uncertainties except for the DR/DS systematic. The reason for excluding this systematic is due to its significant influence and dependence on the single top model (DR or DS), which is not ideal for accurate measurement purposes. As described in 8, in certain phase space the dominant modelling uncertainty of the measurement is the DR/DS uncertainty. The presence of this uncertainty in the dominant set indicates that the unfolding procedure implemented in the measurement is sensitive to the underlying modelling of the single-top process, and in particular to the underlying modelling of its interference with top-pair processes. This can be expected, as the measurement is designed to have maximum sensitivity to the interference as well as because the single-top and top-pairs are treated simultaneously as the signal and unfolded together. It is also important to emphasise that many attempts have been made in the design of this analysis to reduce the DR/DS uncertainty as much as possible, although considering this uncertainty is necessary as it is a real dependence of the measurement on the Monte Carlo modelling assumptions. This uncertainty will be easily removed once the new Monte Carlo samples modelling interference will become available [38]. For this reason the measurement is also shown excluding DS/DR, expecting that future measurements in this field will be able to significantly reduce this systematic uncertainty in the measurement.

The total uncertainty is the quadrature sum of experimental and theoretical systematic and statistical uncertainties. The bottom panel shows the ratio of generated SM prediction to the unfolded data. The figures in the left column show results for the measurement-like phase space and the right one the results for the search-like phase space. The rows show the different variables: lepton p_T in the first row, leading b-jet p_T in the second row and subleading b-jet p_T in the third row in Figure 9.1. While Figure 9.2 shows E_T^{miss} in the first row, m_{bl}^{min} in the second row and $m_T^{min}(bl)$ in the third row.

The first variable to be discussed in this chapter will be m_{bl}^{min}, shown in figures 9.2c and 9.2d, as it is the most sensitive to interference.

As detailed in Chapter 6, this variable is the invariant mass of a b-jet and a lepton [10] and it can discriminates very well between resonant and non-resonant $WbWb$ production. It is designed to exhibit an endpoint at 150 GeV for a b-jet and a lepton originating from the decay of an on-shell top quark.

The m_{bl}^{min} variable effectively constrains one of the $t\bar{t}$ quark decays, since it is expected that m_{bl} will always be below m_{top}, whereas in non-resonant Wb systems m_{bl} can take any value. Therefore, events with $m_{bl} > m_{top}$ indicate that at least one of the two Wb pairs was produced non-resonantly. Consequently, the suppression of the on-shell $t\bar{t}$ contribution for high values of m_{bl}^{min} results in an increased sensitivity to Wb systems with a higher invariant mass, exceeding the one expected from resonantly decaying top quarks.

For the measurement-like phase space (MLPS), Figure 9.2c, the Diagram Removal and Diagram Subtraction predictions are in agreement with the unfolded data in the first bins of the distributions. However, beyond the 150 GeV cut-off, there are discrepancies between the two predictions: the DR prediction shows an upward trend compared to the data, making it incompatible with the unfolded data. Conversely, the DS prediction remains consistent with the data within the uncertainties.

In the search-like phase (SLPS), Figure 9.2d, space the DR and DS predictions envelope the data, suggesting that the overall normalisation in this phase space is not properly predicted. In particular, in this phase space characterised by extreme conditions, the acceptances of the DR and DS samples show significant differences due to variations in the tW fraction present in the DR/DS Monte Carlo samples.

The remaining sensitive variables are shown in the rest of the figures and show a behaviour very similar to m_{bl}^{min}.

In the measurement-like phase space (MLPS), the Diagram Removal and Diagram Subtraction predictions are in agreement with the unfolded data in the first bins of the distributions. From the middle bins to the tails the two predictions behave differently: the DR predictions has a slope with upward trend with respect to data and are not compatible with the unfolded data, on the other hand the DS predictions are, for most of the variables, compatible with data within the uncertainties. In the search-like phase space (SLPS), both the DR and DS predictions envelope the data indicating that the overall normalisation in this phase space is not accurately predicted for all variables considered. In general, neither of the two predictions is compatible with unfolded data within the uncertainties.

For the lepton transverse momentum, the discrepancy between data and Monte Carlo simulated samples is attributed the mismodelling of the top quark p_T spectrum in the $t\bar{t}$ simulation. This effect has been observed in different differential cross-section measurements [176, 177]. The mismodelling occurs at the high-p_T tail, where the MC prediction is typically overestimated, and there is an additional effect for high jet multiplicity events, where the MC prediction is typically underestimated. This mismodelling affects kinematic variables which are constructed based on the p_T of all physics objects and it depends on the number of jets in the event. Better agreement of the distributions

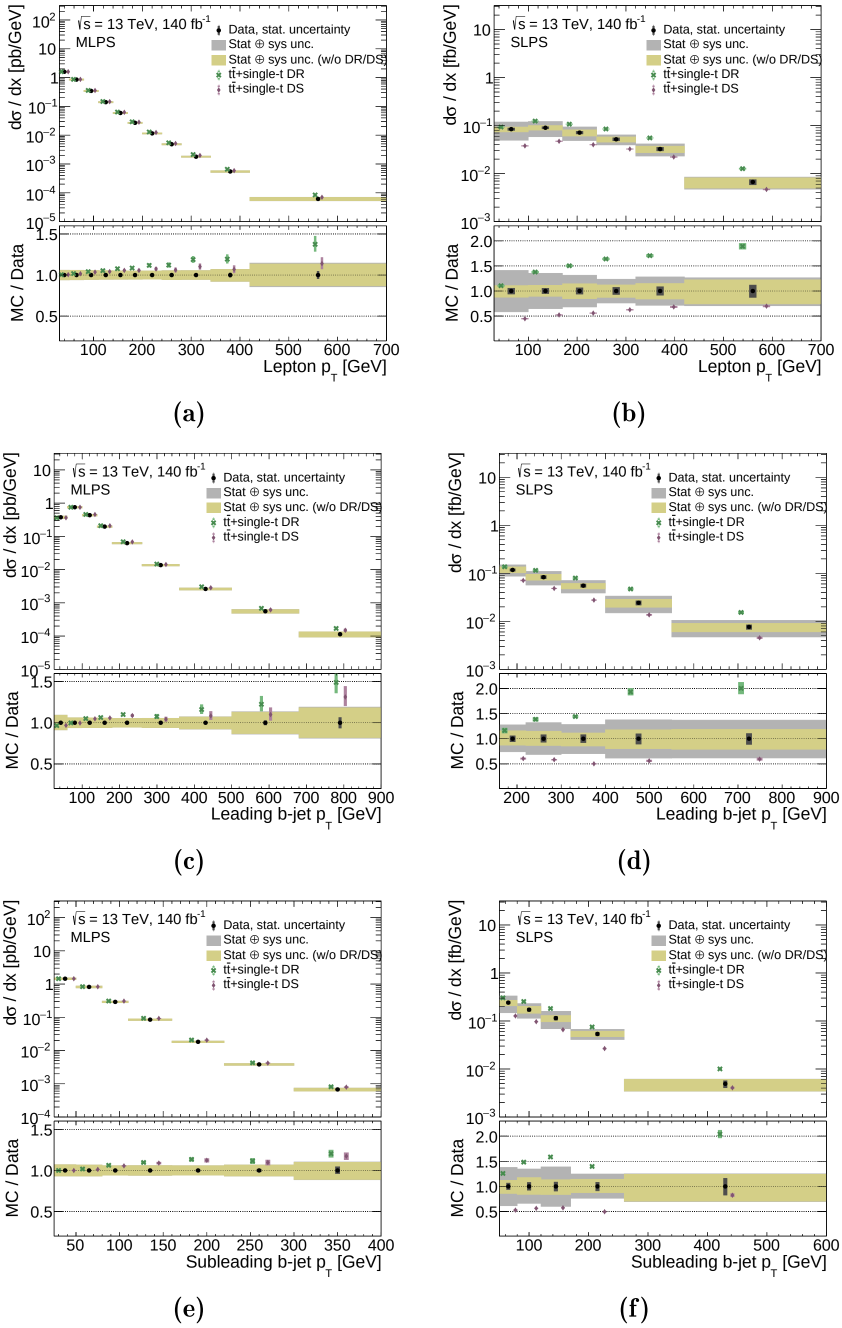

Figure 9.1: Absolute differential cross-section measurement as a function of: lepton p_T (a, b), leading b-jet p_T (c, d) and subleading b-jet p_T (e, f) for the measurement-like (a, c, e) and search-like (b, d, f) phase space, compared to DR and DS interference generators. The cross-section is unfolded at particle-level in the fiducial phase space. The unfolded data are shown as black points, while coloured points indicate the MC predictions. Data points are placed at the centre of each bin while predictions are shifted for clarity. Uncertainties are shown by the shaded bands. The lower panel shows the ratio of the MC predictions to the unfolded data.

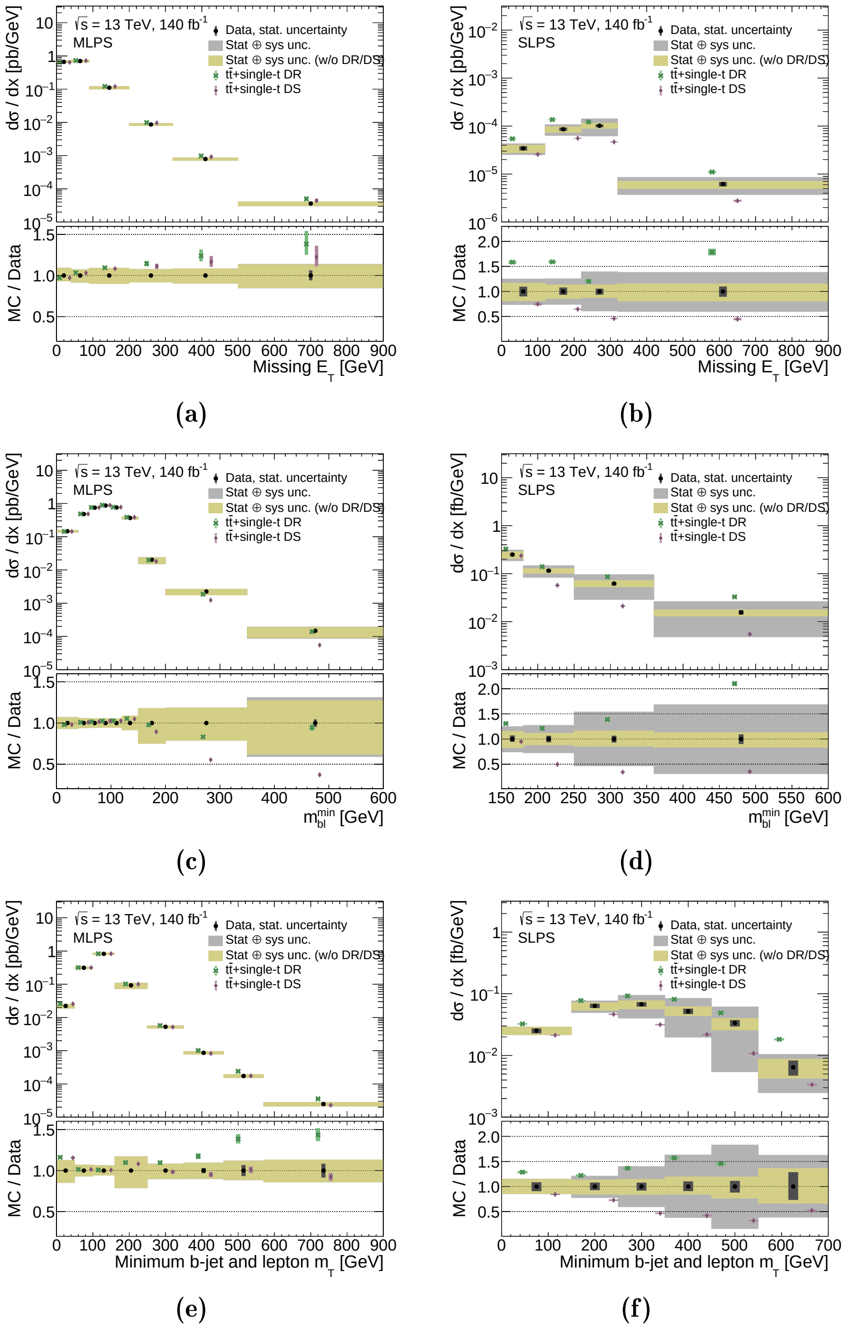

Figure 9.2: Absolute differential cross-section measurement as a function of: E_T^{miss} (a, b), m_{bl}^{min} (c, d) and m_{T2} (e, f) for the measurement-like (a, c, e) and search-like (b, d, f) phase space, compared to DR and DS interference generators. The cross-section is unfolded at particle-level in the fiducial phase space. The unfolded data are shown as black points, while coloured points indicate the MC predictions. Data points are placed at the centre of each bin while predictions are shifted for clarity. Uncertainties are shown by the shaded bands. The lower panel shows the ratio of the MC predictions to the unfolded data.

are obtained by reweighting the $t\bar{t}$ sample based on NNLO corrections to the top-quark p_T spectrum.

Figures 9.3a and 9.3c show the difference between the Monte Carlo predictions without correcting for the $t\bar{t}$ mismodelling, while figures 9.3b and 9.3d show the reweighted distributions. From the ratio plot it can be seen that both the DR and DS predictions, especially the DS prediction, are in almost perfect agreement with the data.

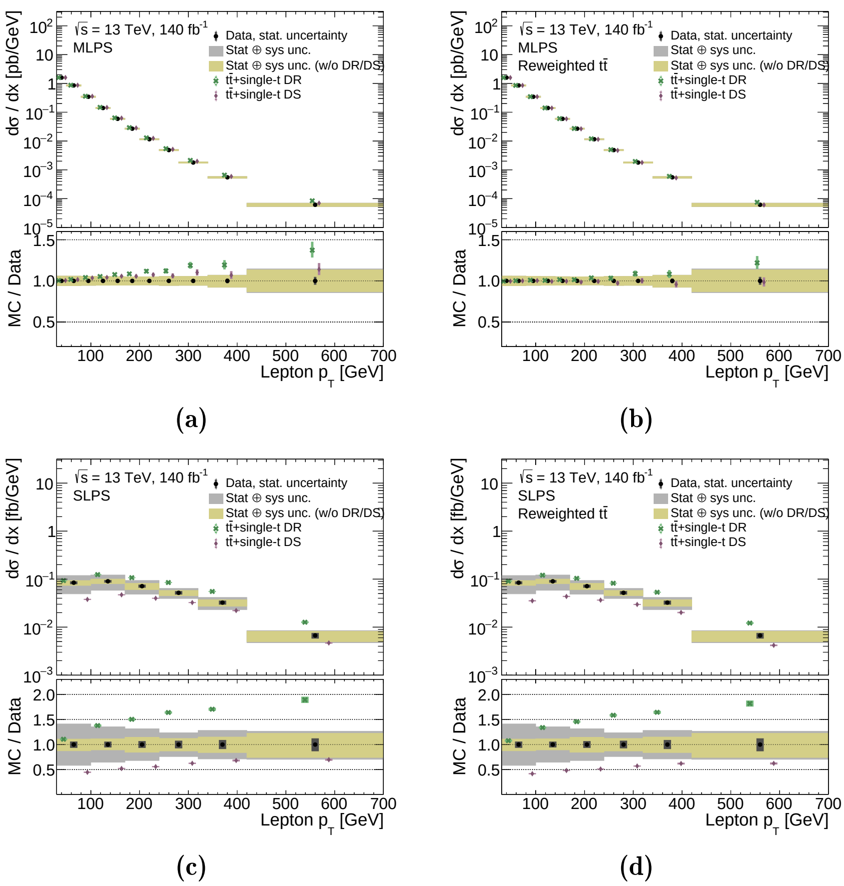

Figure 9.3: Absolute differential cross-section measurement as a function of the lepton p_T, for the measurement-like (a, b) and search-like (c, d) phase space, compared to DR and DS interference generators. Figures a and c show the result without taking into account the mismodelling of the $t\bar{t}$, while figures b and d show the Monte Carlo predictions considering the $t\bar{t}$ reweighting. The cross-section is unfolded at particle-level in the fiducial phase space. The unfolded data are shown as black points, while coloured points indicate the MC predictions. Data points are placed at the centre of each bin while predictions are shifted for clarity. Uncertainties are shown by the shaded bands. The lower panel shows the ratio of the MC predictions to the unfolded data.

It has to be noticed that for the measurement-like phase space the uncertainty band doesn't show any difference if DR/DS modelling uncertainty is considered while for the search-like phase space the uncertainty band without DR/DS is smaller, reducing from 50% to 20%. The size and shape of the DR/DS systematics is different then the difference to the data as well, even if there is a 50% systematics in some bins, this shows that the measurement is relevant even with significant systematics.

The agreement of the different models with the measured differential cross-sections is assessed by computing the χ^2, and corresponding p-values, of the unfolded data with respect to the theoretical predictions. The tables are shown in the next section.

To summarize, while there is reasonable agreement between models and data for the measurement phase space, especially for the Diagram Subtraction prediction, the models have some difficulty in describing the search-like phase space. In the latter phase space, the interference between the production of two on-shell tops and at least one off-shell Wb system is more important. This difference is expected because DR and DS interference schemes are designed to describe tWb events and only approximate the interference between top pairs and single tops.

9.1 χ^2 calculation

The level of agreement between the unfolded cross-sections and the different predictions is evaluated by using a χ^2 test-statistic. The results of the χ^2 test are presented in Section 9.1.1. The thresholds for the p-value, obtained from the χ^2 test, are:

- p-value $\lesssim 0.0455$: 2σ
- p-value $\lesssim 0.027$: 3σ
- p-value $\lesssim 5.7 \cdot 10^{-7}$: 5σ

The χ^2 are computed using the formula:

$$\chi^2 = \mathcal{V}^T \times \mathcal{C}^{-1} \times \mathcal{V} \tag{9.1}$$

where $\mathcal{V}$ represents the vector of residuals, defined as the difference between the unfolded differential cross-section and the different predictions. $\mathcal{C}$ is the covariance matrix of $\mathcal{V}$.

The covariance matrix $\mathcal{C}$ is computed for each source of systematic uncertainty as:

$$c_{ij} = \begin{pmatrix} c_{11} & c_{12} & \cdots & c_{1n} \\ c_{21} & c_{22} & \cdots & c_{2n} \\ \vdots & \vdots & \ddots & \vdots \\ c_{n1} & c_{n2} & \cdots & c_{nn} \end{pmatrix} \tag{9.2}$$

where $c_{ij} = \sigma_i \cdot \sigma_j$.

The σ_i are defined as:

$$\sigma_i = \frac{\sigma_i^{\mathrm{up}} + \sigma_i^{\mathrm{down}}}{2} \tag{9.3}$$

$\sigma_i^{up,down}$ represent respectively the up and down variation in i-th bin. The σ_j are defined in the same way, considering the j-th bin.

The systematic component of the covariance matrix is defined as the sum of each covariance matrix for each systematic and the total covariance matrix is defined as the sum of the systematic and the statistical components.

9.1.1 χ^2 Tables

This section shows the χ^2 values and the correspondent p-value for the unfolded simple and compound variables in the two phase spaces of the analysis.

Table **??** shows, for the measurement-like phase space, compatibility between data and Monte Carlo predictions. The leading b-jet p_T, subleading b-jet p_T and $m_T^{min}(bl)$ show a discrepancy of 2σ for the DR predictions, which is not significant. There is an exception for the lepton transverse momentum, which is motivated by the mismodelling of the $t\bar{t}$ samples detailed in the previous section.

For the search-like phase space the table is not shown as the p-value < 0.001, corresponding to a value of 5σ for all the variables, except for the E_T^{miss} which for the DR prediction shows a 2σ disagreement. For both the phase spaces the χ^2 and p-values are calculated for the Diagram Removal and Diagram Subtraction predictions.

Observable	PH+Pythia8 (DR)		PH+Pythia8 (DS)	
	χ^2 / NDF	p-value	χ^2 / NDF	p-value
Missing E_T	11.08 / 6	0.086	5.30 / 6	0.506
m_{bl}^{min}	7.50 / 9	0.585	10.48 / 9	0.313
Minimum b-jet and lepton m_T	22.21 / 8	0.005	7.54 / 8	0.479
Lepton p_T	32.26 /11	0.001	19.06 /11	0.060
Leading b-jet p_T	22.19 / 9	0.008	19.88 / 9	0.019
Subleading b-jet p_T	17.62 / 7	0.014	16.67 / 7	0.020

Table 9.1: χ^2 and p-values for the simple and compound variables in the measurement-like phase space. Both χ^2 and $p - values$ are calculated for both the Diagram Removal and Diagram Subtraction schemes.

10
Summary and outlook

This thesis presented the first measurement of the differential production cross sections of the $pp \to WbWb$ process in the l+jets decay channel. The data used in this thesis were collected by the ATLAS detector at the Large Hadron Collider (LHC) during LHC Run-2, spanning the years 2015 to 2018, at a centre-of-mass energy of $\sqrt{s} = 13\,\text{TeV}$ [12].

$WbWb$ is a common final state for both top quark pair production ($t\bar{t}$) and single top quark production at Next-to-Leading Order (NLO) in α_S (tWb). Since these two processes share the same final state, there is interference between them. Various theoretical models, such as Diagram Removal, Diagram Subtraction and more recently the bb4l schemes, have been developed to accurately represent this interference. The intricate nature of modelling this interference presents a challenge to theorists, requiring the inclusion of higher order corrections.

A comprehensive measurement of this process is therefore essential to compare with theoretical predictions and improve their accuracy. In particular, the interference between top-quark pair production and single-top production in higher-order perturbative QCD introduces considerable uncertainty in BSM physics.

During Run-1, a previous measurement revealed inconsistencies between the modelling of the interference and the collected data. The novelty of the measurement presented in this thesis lies in its novel nature, as it marks the first instance of performing the interference measurement in the single lepton channel.

The decay channel refers to the decay of the two W bosons, where one W boson decays leptonically into a charged lepton (muon or electron, $\mu^{\pm}$ or $e^{\pm}$) and a neutrino ν, while the other decays hadronically and can be identified by jets.

Two different phase spaces have been defined for this measurement. The first, known as the measurement phase space, is very similar to the phase spaces commonly used in Standard Model measurements. The second, known as the search-like phase space, is tailored for Beyond Standard Model (BSM) searches. Variables which are particularly sensitive to the interference have been identified, and the differential cross section is measured using an unfolding procedure to correct for limited geometric acceptance and detector efficiency. Discrepancies between the data and the Monte Carlo generator in the unfolded cross section have been found.

This thesis provided a thorough investigation of the interference between tW and $t\bar{t}$, providing valuable insights into top quark physics. It contributes to ongoing efforts to improve theoretical predictions and reduce uncertainties in the search for new physics at high masses.

The important contribution of the thesis comes from the fact that the interference measurement has been made for the first time in the single lepton channel, both for the ATLAS and CMS experiments. Several variables sensitive to the interference have been found and different theoretical predictions have been compared. For the measurement-like phase space significant discrepancies have been found between unfolded data and predictions, indicating that the interference is not well modelled by any of the existent generators.

The results of this thesis are important since unfolded data can be further used by the scientific community without the limitation of needing a detector simulation to tune and validate the theoretical predictions.

The sensitivity of the analysis is currently limited by statistical limitations and uncertainties related to the interference. Therefore, further improvements can be achieved with data from Run 3 and by using new Monte Carlo samples, which can be optimised based on these results.

References

[1] Steven Weinberg. "A Model of Leptons". In: *Phys. Rev. Lett.* 19 (21 Nov. 1967), pp. 1264–1266. URL: `https://link.aps.org/doi/10.1103/PhysRevLett.19.1264`.

[2] S. L. Glashow. "Partial Symmetries of Weak Interactions". In: *Nucl. Phys.* 22 (1961), pp. 579–588.

[3] "LHC Machine". In: *JINST* 3 (2008). Ed. by Lyndon Evans and Philip Bryant, S08001.

[4] R. L. Workman et al. "Review of Particle Physics". In: *PTEP* 2022 (2022), p. 083C01.

[5] Andrea Giammanco. "Single top quark production at the LHC". In: *Reviews in Physics* 1 (Nov. 2016), pp. 1–12. URL: `https://doi.org/10.1016%2Fj.revip.2015.12.001`.

[6] Alexandre Deur, Stanley J. Brodsky, and Guy F. de Teramond. "The QCD Running Coupling". In: *Nucl. Phys.* 90 (2016), p. 1. arXiv: `1604.08082 [hep-ph]`.

[7] Stefano Frixione et al. "Single-top hadroproduction in association with aiW/iboson". In: *Journal of High Energy Physics* 2008.07 (July 2008), pp. 029–029. URL: `https://doi.org/10.1088%2F1126-6708%2F2008%2F07%2F029`.

[8] Georges Aad et al. "Search for new phenomena with top quark pairs in final states with one lepton, jets, and missing transverse momentum in pp collisions at $\sqrt{s} = 13$ TeV with the ATLAS detector". In: *JHEP* 04 (2021), p. 174. arXiv: `2012.03799 [hep-ex]`.

[9] ATLAS Collaboration. "Search for dark matter produced in association with a single top quark and an energetic W boson in $\sqrt{s} = 13\,\text{TeV}$ pp collisions with the ATLAS detector". In: *Eur. Phys. J. C* 83 (2022), p. 603. arXiv: `2211.13138 [hep-ex]`.

[10] Morad Aaboud et al. "Probing the quantum interference between singly and doubly resonant top-quark production in pp collisions at $\sqrt{s} = 13$ TeV with the ATLAS detector". In: *Phys. Rev. Lett.* 121.15 (2018), p. 152002. arXiv: `1806.04667 [hep-ex]`.

[11] Armen Tumasyan et al. "Measurement of inclusive and differential cross sections for single top quark production in association with a W boson in proton-proton collisions at $\sqrt{s} = 13$ TeV". In: *JHEP* 07 (2023), p. 046. arXiv: `2208.00924 [hep-ex]`.

[12] G. Aad et al. "The ATLAS Experiment at the CERN Large Hadron Collider". In: *JINST* 3 (2008), S08003.

[13] Alexei Deriglazov. "Transformations, Symmetries and Noether Theorem". In: 2017.

[14] Georges Aad et al. "Determination of the strong coupling constant from transverse energy−energy correlations in multijet events at $\sqrt{s} = 13$ TeV with the ATLAS detector". In: *JHEP* 07 (2023), p. 085. arXiv: `2301.09351 [hep-ex]`.

[15] Peter W. Higgs. "Broken Symmetries and the Masses of Gauge Bosons". In: *Phys. Rev. Lett.* 13 (16 Oct. 1964), pp. 508–509. URL: `https://link.aps.org/doi/10.1103/PhysRevLett.13.508`.

[16] F. Englert and R. Brout. "Broken Symmetry and the Mass of Gauge Vector Mesons". In: *Phys. Rev. Lett.* 13 (9 Aug. 1964), pp. 321–323. URL: `https://link.aps.org/doi/10.1103/PhysRevLett.13.321`.

[17] John Ellis, Mary K. Gaillard, and Dimitri V. Nanopoulos. "A Historical Profile of the Higgs Boson". In: *The standard theory of particle physics: Essays to celebrate CERN's 60th anniversary.* Ed. by Luciano Maiani and Luigi Rolandi. 2016, pp. 255–274. arXiv: `1504.07217 [hep-ph]`.

[18] Andreas Crivellin, Martin Hoferichter, and Claudio Andrea Manzari. "Fermi Constant from Muon Decay Versus Electroweak Fits and Cabibbo-Kobayashi-Maskawa Unitarity". In: *Phys. Rev. Lett.* 127.7 (2021), p. 071801. arXiv: `2102.02825 [hep-ph]`.

[19] Georges Aad et al. "Observation of a new particle in the search for the Standard Model Higgs boson with the ATLAS detector at the LHC". In: *Phys. Lett. B* 716 (2012), pp. 1–29. arXiv: `1207.7214 [hep-ex]`.

[20] Serguei Chatrchyan et al. "Observation of a New Boson at a Mass of 125 GeV with the CMS Experiment at the LHC". In: *Phys. Lett. B* 716 (2012), pp. 30–61. arXiv: `1207.7235 [hep-ex]`.

[21] Andre Sopczak. *Precision Measurements in the Higgs Sector at ATLAS and CMS.* 2020. arXiv: `2001.05927 [hep-ex]`.

[22] R. P. Feynman. *Selected papers of Richard Feynman: With commentary.* Ed. by L. M. Brown. Vol. 27. World Scientific Series in 20th Century Physics. 2000.

[23] A. D. Martin et al. "Parton distributions for the LHC". In: *Eur. Phys. J. C* 63 (2009), pp. 189–285. arXiv: `0901.0002 [hep-ph]`.

[24] Chris Blanks. *Strangeness at LHCb.* 2011. URL: `https://imperialhep.blogspot.com/2011/08/`.

[25] John C. Collins, Davison E. Soper, and George F. Sterman. "Factorization of Hard Processes in QCD". In: *Adv. Ser. Direct. High Energy Phys.* 5 (1989), pp. 1–91. arXiv: `hep-ph/0409313`.

[26] Guido Altarelli and G. Parisi. "Asymptotic Freedom in Parton Language". In: *Nucl. Phys. B* 126 (1977), pp. 298–318.

[27] Sergey Alekhin, Kirill Melnikov, and Frank Petriello. "Fixed target Drell-Yan data and NNLO QCD fits of parton distribution functions". In: *Phys. Rev. D* 74 (2006), p. 054033. arXiv: `hep-ph/0606237`.

[28] Sergey Alekhin et al. "The PDF4LHC Working Group Interim Report". In: (Jan. 2011). arXiv: `1101.0536 [hep-ph]`.

[29] A. B. Arbuzov. "Quantum Field Theory and the Electroweak Standard Model". In: (2017). Ed. by Martijn Mulders and Giulia Zanderighi, pp. 1–34. arXiv: `1801.05670 [hep-ph]`.

[30] Makoto Kobayashi and Toshihide Maskawa. "CP Violation in the Renormalizable Theory of Weak Interaction". In: *Prog. Theor. Phys.* 49 (1973), pp. 652–657.

[31] Nicola Cabibbo. "Unitary Symmetry and Leptonic Decays". In: *Phys. Rev. Lett.* 10 (12 June 1963), pp. 531–533. URL: `https://link.aps.org/doi/10.1103/PhysRevLett.10.531`.

[32] S. Abachi et al. "Observation of the top quark". In: *Phys. Rev. Lett.* 74 (1995), pp. 2632–2637. arXiv: `hep-ex/9503003`.

[33] "First combination of Tevatron and LHC measurements of the top-quark mass". In: (Mar. 2014). arXiv: `1403.4427 [hep-ex]`.

[34] LHC Top Working Group. *LHCTopWG Summary Plots*. Last accessed 05 Novemver 2023. 2023. URL: `https://twiki.cern.ch/twiki/bin/view/LHCPhysics/LHCTopWGSummaryPlots`.

[35] Izaak Neutelings. *The TikZ package for Particle Physics*. URL: `https://tikz.net/category/physics/`.

[36] Stefano Frixione et al. "Single-top hadroproduction in association with a W boson". In: *JHEP* 07 (2008), p. 029. arXiv: `0805.3067 [hep-ph]`.

[37] "Studies of $t\bar{t}/tW$ interference effects in $b\bar{b}\ell^+\ell^{-'}\nu\bar{\nu}'$ final states with Powheg and MG5_aMC@NLO setups". In: (2021).

[38] Tomáš Ježo, Jonas M. Lindert, and Stefano Pozzorini. "Resonance-aware NLOPS matching for off-shell $t\bar{t}$ + tW production with semileptonic decays". In: *JHEP* 10 (2023), p. 008. arXiv: `2307.15653 [hep-ph]`.

[39] Wei-Shu Hou. "Source of CP Violation for the Baryon Asymmetry of the Universe". In: *Chin. J. Phys.* 47 (2009), p. 134. arXiv: `0803.1234 [hep-ph]`.

[40] Q. R. et al. Ahmad. "Direct Evidence for Neutrino Flavor Transformation from Neutral-Current Interactions in the Sudbury Neutrino Observatory". In: *Phys. Rev. Lett.* 89 (1 June 2002), p. 011301. URL: `https://link.aps.org/doi/10.1103/PhysRevLett.89.011301`.

[41] Y. et al. Fukuda. "Evidence for Oscillation of Atmospheric Neutrinos". In: *Phys. Rev. Lett.* 81 (8 Aug. 1998), pp. 1562–1567. URL: `https://link.aps.org/doi/10.1103/PhysRevLett.81.1562`.

[42] Q. R. et al. Ahmad. "Measurement of the Rate of $\nu_e + d \to p + p + e^-$ Interactions Produced by ^8B Solar Neutrinos at the Sudbury Neutrino Observatory". In: *Phys. Rev. Lett.* 87 (7 July 2001), p. 071301. URL: `https://link.aps.org/doi/10.1103/PhysRevLett.87.071301`.

[43] Abhay Ashtekar. "Gravity and the quantum". In: *New J. Phys.* 7 (2005). Ed. by Gianluca Calcagni et al., p. 198. arXiv: gr-qc/0410054.

[44] Nima Arkani-Hamed, Savas Dimopoulos, and G. R. Dvali. "The Hierarchy problem and new dimensions at a millimeter". In: *Phys. Lett. B* 429 (1998), pp. 263–272. arXiv: hep-ph/9803315.

[45] Roel Aaij et al. "Test of lepton flavor universality using B0→D*-τ+$\nu\tau$ decays with hadronic τ channels". In: *Phys. Rev. D* 108.1 (2023), p. 012018. arXiv: 2305.01463 [hep-ex].

[46] B. Abi et al. "Measurement of the Positive Muon Anomalous Magnetic Moment to 0.46 ppm". In: *Phys. Rev. Lett.* 126.14 (2021), p. 141801. arXiv: 2104.03281 [hep-ex].

[47] Thomas Taylor and Daniel Treille. "The Large Electron Positron Collider (LEP): Probing the Standard Model". In: *Adv. Ser. Direct. High Energy Phys.* 27 (2017). Ed. by Christian Fabjan et al., pp. 217–261.

[48] S. Chatrchyan et al. "The CMS Experiment at the CERN LHC". In: *JINST* 3 (2008), S08004.

[49] K. Aamodt et al. "The ALICE experiment at the CERN LHC". In: *JINST* 3 (2008), S08002.

[50] Jr. Alves A.Augusto et al. "The LHCb Detector at the LHC". In: *JINST* 3 (2008), S08005.

[51] Ewa Lopienska. "The CERN accelerator complex, layout in 2022. Complexe des accélérateurs du CERN en janvier 2022". In: (2022). General Photo. URL: https://cds.cern.ch/record/2800984.

[52] I. Zurbano Fernandez et al. "High-Luminosity Large Hadron Collider (HL-LHC): Technical design report". In: 10/2020 (Dec. 2020). Ed. by I. Béjar Alonso et al.

[53] Georges Aad et al. "ATLAS data quality operations and performance for 2015–2018 data-taking". In: *JINST* 15.04 (2020), P04003. arXiv: 1911.04632 [physics.ins-det].

[54] G. Aad et al. "The ATLAS Experiment at the CERN Large Hadron Collider". In: *JINST* 3 (2008), S08003.

[55] Joao Pequenao. "Computer generated image of the whole ATLAS detector". Mar. 2008. URL: https://cds.cern.ch/record/1095924.

[56] Izaak Neutelings. *Image compiled from code made available under CC BY-SA 4.0.* URL: https://wiki.physik.uzh.ch/cms/latex:example_spherical_coordinates.

[57] *ATLAS inner detector: Technical Design Report, 1.* Technical design report. ATLAS. Geneva: CERN, 1997. URL: https://cds.cern.ch/record/331063.

[58] G. Aad et al. "The ATLAS Inner Detector commissioning and calibration". In: *Eur. Phys. J. C* 70 (2010), pp. 787–821. arXiv: 1004.5293 [physics.ins-det].

[59] Georges Aad et al. "Alignment of the ATLAS Inner Detector in Run-2". In: *Eur. Phys. J. C* 80.12 (2020), p. 1194. arXiv: 2007.07624 [hep-ex].

[60] Alessandro La Rosa. "The ATLAS Insertable B-Layer: from construction to operation". In: *JINST* 11.12 (2016). Ed. by Claudia Gemme and Leonardo Rossi, p. C12036. arXiv: 1610.01994 [physics.ins-det].

[61] G. Aad et al. "ATLAS pixel detector electronics and sensors". In: *JINST* 3 (2008), P07007.

[62] A. Ahmad et al. "The Silicon microstrip sensors of the ATLAS semiconductor tracker". In: *Nucl. Instrum. Meth. A* 578 (2007), pp. 98–118.

[63] Morad Aaboud et al. "Performance of the ATLAS Transition Radiation Tracker in Run 1 of the LHC: tracker properties". In: *JINST* 12.05 (2017), P05002. arXiv: 1702.06473 [hep-ex].

[64] A. Airapetian et al. "ATLAS calorimeter performance Technical Design Report". In: (Dec. 1996).

[65] Joao Pequenao. "Computer Generated image of the ATLAS calorimeter". Mar. 2008. URL: https://cds.cern.ch/record/1095927.

[66] "ATLAS muon spectrometer: Technical design report". In: (June 1997).

[67] Fabian Kuger. "Signal Formation Processes in Micromegas Detectors and Quality Control for large size Detector Construction for the ATLAS New Small Wheel". In: (Aug. 2017).

[68] Federico Lasagni Manghi. "LUCID: The ATLAS Luminosity Detector". In: *PoS* ICHEP2018 (2019), p. 280.

[69] Peter J. Bussey. "Overview of the ATLAS ALFA detectors, performance and physics analysis". In: (July 2023). arXiv: 2308.00110 [hep-ex].

[70] Sebastian White. "The ATLAS zero degree calorimeter". In: *Nucl. Instrum. Meth. A* 617 (2010). Ed. by Giorgio Chiarelli et al., pp. 126–128.

[71] L. Adamczyk et al. "Technical Design Report for the ATLAS Forward Proton Detector". In: (May 2015).

[72] Georges Aad et al. "Operation of the ATLAS trigger system in Run 2". In: *JINST* 15.10 (2020), P10004. arXiv: 2007.12539 [physics.ins-det].

[73] ATLAS Collaboration. *Athena*. Version 22.0.1. Apr. 2019. URL: https://doi.org/10.5281/zenodo.2641997.

[74] Iulia Georgescu. "Simulating parton showers". In: *Nature Reviews Physics* (2021). URL: https://doi.org/10.1038/s42254-021-00282-w.

[75] Andy Buckley et al. "General-purpose event generators for LHC physics". In: *Phys. Rept.* 504 (2011), pp. 145–233. arXiv: 1101.2599 [hep-ph].

[76] X. Artru and G. Mennessier. "String model and multiproduction". In: *Nuclear Physics B* 70.1 (1974), pp. 93–115. URL: https://www.sciencedirect.com/science/article/pii/0550321374903605.

[77] D. Amati and G. Veneziano. "Preconfinement as a property of perturbative QCD". In: *Physics Letters B* 83.1 (1979), pp. 87–92. URL: https://www.sciencedirect.com/science/article/pii/0370269379908967.

[78] B.R. Webber. “A QCD model for jet fragmentation including soft gluon interference”. In: *Nuclear Physics B* 238.3 (1984), pp. 492–528. URL: https://www.sciencedirect.com/science/article/pii/055032138490333X.

[79] G. Marchesini and B.R. Webber. “Monte Carlo simulation of general hard processes with coherent QCD radiation”. In: *Nuclear Physics B* 310.3 (1988), pp. 461–526. URL: https://www.sciencedirect.com/science/article/pii/0550321388900892.

[80] BRYAN R. WEBBER. “FRAGMENTATION AND HADRONIZATION”. In: *International Journal of Modern Physics A* 15.supp01b (2000), pp. 577–606. eprint: https://doi.org/10.1142/S0217751X00005334. URL: https://doi.org/10.1142/S0217751X00005334.

[81] Simone Alioli et al. “A general framework for implementing NLO calculations in shower Monte Carlo programs: the POWHEG BOX”. In: *JHEP* 06 (2010), p. 043. arXiv: 1002.2581 [hep-ph].

[82] J. Alwall et al. “The automated computation of tree-level and next-to-leading order differential cross sections, and their matching to parton shower simulations”. In: *JHEP* 07 (2014), p. 079. arXiv: 1405.0301 [hep-ph].

[83] Torbjörn Sjöstrand et al. “An introduction to PYTHIA 8.2”. In: *Computer Physics Communications* 191 (2015), pp. 159–177. URL: https://www.sciencedirect.com/science/article/pii/S0010465515000442.

[84] Johannes Bellm et al. “Herwig 7.0/Herwig++ 3.0 release note”. In: *Eur. Phys. J. C* 76.4 (2016), p. 196. arXiv: 1512.01178 [hep-ph].

[85] Stefano Catani et al. “The Dipole formalism for next-to-leading order QCD calculations with massive partons”. In: *Nucl. Phys. B* 627 (2002), pp. 189–265. arXiv: hep-ph/0201036.

[86] S. Catani et al. “QCD Matrix Elements + Parton Showers”. In: *JHEP* 11 (2001), p. 063. arXiv: hep-ph/0109231.

[87] Enrico Bothmann et al. “Event Generation with Sherpa 2.2”. In: *SciPost Phys.* 7.3 (2019), p. 034. arXiv: 1905.09127 [hep-ph].

[88] D. J. Lange. “The EvtGen particle decay simulation package”. In: *Nucl. Instrum. Meth. A* 462 (2001), p. 152.

[89] Pierre Artoisenet et al. “Automatic spin-entangled decays of heavy resonances in Monte Carlo simulations”. In: *JHEP* 03 (2013), p. 015. arXiv: 1212.3460 [hep-ph].

[90] Roland Jansky. “The ATLAS Fast Monte Carlo Production Chain Project”. In: *Journal of Physics: Conference Series* 664.7 (Dec. 2015), p. 072024. URL: https://doi.org/10.1088/1742-6596/664/7/072024.

[91] S. Agostinelli, J. Allison, and K. Amako et al. “Geant4—a simulation toolkit”. In: *Nuclear Instruments and Methods in Physics Research Section A: Accelerators, Spectrometers, Detectors and Associated Equipment* 506.3 (2003), pp. 250–303. URL: http://www.sciencedirect.com/science/article/pii/S0168900203013688.

[92] ATLAS Collaboration. "The ATLAS Simulation Infrastructure". In: *Eur. Phys. J. C* 70 (2010), p. 823. arXiv: `1005.4568 [physics.ins-det]`.

[93] T. Sjöstrand, S. Mrenna, and P. Skands. "A brief introduction to PYTHIA 8.1". In: *Comput. Phys. Commun.* 178 (2008), pp. 852–867. arXiv: `0710.3820 [hep-ph]`.

[94] NNPDF Collaboration, Richard D. Ball, et al. "Parton distributions with LHC data". In: *Nucl. Phys. B* 867 (2013), p. 244. arXiv: `1207.1303 [hep-ph]`.

[95] ATLAS Collaboration. *The Pythia 8 A3 tune description of ATLAS minimum bias and inelastic measurements incorporating the Donnachie–Landshoff diffractive model.* ATL-PHYS-PUB-2016-017. 2016. URL: `https://cds.cern.ch/record/2206965`.

[96] ATLAS Collaboration. "Measurement of the Inelastic Proton–Proton Cross Section at $\sqrt{s} = 13\,\text{TeV}$ with the ATLAS Detector at the LHC". In: *Phys. Rev. Lett.* 117 (2016), p. 182002. arXiv: `1606.02625 [hep-ex]`.

[97] Stefano Frixione, Giovanni Ridolfi, and Paolo Nason. "A positive-weight next-to-leading-order Monte Carlo for heavy flavour hadroproduction". In: *JHEP* 09 (2007), p. 126. arXiv: `0707.3088 [hep-ph]`.

[98] Paolo Nason. "A new method for combining NLO QCD with shower Monte Carlo algorithms". In: *JHEP* 11 (2004), p. 040. arXiv: `hep-ph/0409146`.

[99] The NNPDF Collaboration, Richard D. Ball, et al. "Parton distributions for the LHC run II". In: *JHEP* 04 (2015), p. 040. arXiv: `1410.8849 [hep-ph]`.

[100] ATLAS Collaboration. *Studies on top-quark Monte Carlo modelling for Top2016.* ATL-PHYS-PUB-2016-020. 2016. URL: `https://cds.cern.ch/record/2216168`.

[101] Torbjörn Sjöstrand et al. "An introduction to PYTHIA 8.2". In: *Comput. Phys. Commun.* 191 (2015), p. 159. arXiv: `1410.3012 [hep-ph]`.

[102] ATLAS Collaboration. *ATLAS Pythia 8 tunes to 7 TeV data.* ATL-PHYS-PUB-2014-021. 2014. URL: `https://cds.cern.ch/record/1966419`.

[103] M. Beneke et al. "Hadronic top-quark pair production with NNLL threshold resummation". In: *Nucl. Phys. B* 855 (2012), pp. 695–741. arXiv: `1109.1536 [hep-ph]`.

[104] Matteo Cacciari et al. "Top-pair production at hadron colliders with next-to-next-to-leading logarithmic soft-gluon resummation". In: *Phys. Lett. B* 710 (2012), pp. 612–622. arXiv: `1111.5869 [hep-ph]`.

[105] Peter Bärnreuther, Michal Czakon, and Alexander Mitov. "Percent-Level-Precision Physics at the Tevatron: Next-to-Next-to-Leading Order QCD Corrections to $q\bar{q} \to t\bar{t} + X$". In: *Phys. Rev. Lett.* 109 (2012), p. 132001. arXiv: `1204.5201 [hep-ph]`.

[106] Michal Czakon and Alexander Mitov. "NNLO corrections to top-pair production at hadron colliders: the all-fermionic scattering channels". In: *JHEP* 12 (2012), p. 054. arXiv: `1207.0236 [hep-ph]`.

[107] Michal Czakon and Alexander Mitov. "NNLO corrections to top pair production at hadron colliders: the quark-gluon reaction". In: *JHEP* 01 (2013), p. 080. arXiv: 1210.6832 [hep-ph].

[108] Michal Czakon, Paul Fiedler, and Alexander Mitov. "Total Top-Quark Pair-Production Cross Section at Hadron Colliders Through $O(\alpha_S^4)$". In: *Phys. Rev. Lett.* 110 (2013), p. 252004. arXiv: 1303.6254 [hep-ph].

[109] Michal Czakon and Alexander Mitov. "Top++: A program for the calculation of the top-pair cross-section at hadron colliders". In: *Comput. Phys. Commun.* 185 (2014), p. 2930. arXiv: 1112.5675 [hep-ph].

[110] Emanuele Re. "Single-top Wt-channel production matched with parton showers using the POWHEG method". In: *Eur. Phys. J. C* 71 (2011), p. 1547. arXiv: 1009.2450 [hep-ph].

[111] Stefano Frixione, Paolo Nason, and Carlo Oleari. "Matching NLO QCD computations with parton shower simulations: the POWHEG method". In: *JHEP* 11 (2007), p. 070. arXiv: 0709.2092 [hep-ph].

[112] Nikolaos Kidonakis. "Two-loop soft anomalous dimensions for single top quark associated production with a W^- or H^-". In: *Phys. Rev. D* 82 (2010), p. 054018. arXiv: 1005.4451 [hep-ph].

[113] Nikolaos Kidonakis. "Top Quark Production". In: *Proceedings, Helmholtz International Summer School on Physics of Heavy Quarks and Hadrons (HQ 2013)* (JINR, Dubna, Russia, July 15–28, 2013), pp. 139–168. arXiv: 1311.0283 [hep-ph].

[114] Enrico Bothmann et al. "Event generation with Sherpa 2.2". In: *SciPost Phys.* 7.3 (2019), p. 034. arXiv: 1905.09127 [hep-ph].

[115] Tanju Gleisberg and Stefan Höche. "Comix, a new matrix element generator". In: *JHEP* 12 (2008), p. 039. arXiv: 0808.3674 [hep-ph].

[116] Federico Buccioni et al. "OpenLoops 2". In: *Eur. Phys. J. C* 79.10 (2019), p. 866. arXiv: 1907.13071 [hep-ph].

[117] Fabio Cascioli, Philipp Maierhöfer, and Stefano Pozzorini. "Scattering Amplitudes with Open Loops". In: *Phys. Rev. Lett.* 108 (2012), p. 111601. arXiv: 1111.5206 [hep-ph].

[118] Ansgar Denner, Stefan Dittmaier, and Lars Hofer. "Collier: A fortran-based complex one-loop library in extended regularizations". In: *Comput. Phys. Commun.* 212 (2017), pp. 220–238. arXiv: 1604.06792 [hep-ph].

[119] Steffen Schumann and Frank Krauss. "A parton shower algorithm based on Catani–Seymour dipole factorisation". In: *JHEP* 03 (2008), p. 038. arXiv: 0709.1027 [hep-ph].

[120] Jan-Christopher Winter, Frank Krauss, and Gerhard Soff. "A modified cluster-hadronization model". In: *Eur. Phys. J. C* 36 (2004), pp. 381–395. arXiv: hep-ph/0311085.

[121] Stefan Höche et al. "A critical appraisal of NLO+PS matching methods". In: *JHEP* 09 (2012), p. 049. arXiv: 1111.1220 [hep-ph].

[122] Stefan Höche et al. "QCD matrix elements and truncated showers". In: *JHEP* 05 (2009), p. 053. arXiv: `0903.1219 [hep-ph]`.

[123] Stefan Höche et al. "QCD matrix elements + parton showers. The NLO case". In: *JHEP* 04 (2013), p. 027. arXiv: `1207.5030 [hep-ph]`.

[124] Stefan Kallweit et al. "NLO electroweak automation and precise predictions for W+multijet production at the LHC". In: *JHEP* 04 (2015), p. 012. arXiv: `1412.5157 [hep-ph]`.

[125] Stefan Kallweit et al. "NLO QCD+EW predictions for V + jets including off-shell vector-boson decays and multijet merging". In: *JHEP* 04 (2016), p. 021. arXiv: `1511.08692 [hep-ph]`.

[126] Charalampos Anastasiou et al. "High-precision QCD at hadron colliders: Electroweak gauge boson rapidity distributions at next-to-next-to leading order". In: *Phys. Rev. D* 69 (2004), p. 094008. arXiv: `hep-ph/0312266`.

[127] Rikkert Frederix, Emanuele Re, and Paolo Torrielli. "Single-top t-channel hadroproduction in the four-flavour scheme with POWHEG and aMC@NLO". In: *JHEP* 09 (2012), p. 130. arXiv: `1207.5391 [hep-ph]`.

[128] Simone Alioli et al. "NLO single-top production matched with shower in POWHEG: s- and t-channel contributions". In: *JHEP* 09 (2009), p. 111. arXiv: `0907.4076 [hep-ph]`.

[129] Stefano Frixione et al. "Angular correlations of lepton pairs from vector boson and top quark decays in Monte Carlo simulations". In: *JHEP* 04 (2007), p. 081. arXiv: `hep-ph/0702198`.

[130] Heribertus B. Hartanto et al. "Higgs boson production in association with top quarks in the POWHEG BOX". In: *Phys. Rev. D* 91.9 (2015), p. 094003. arXiv: `1501.04498 [hep-ph]`.

[131] Joao Pequenao and Paul Schaffner. "How ATLAS detects particles: diagram of particle paths in the detector". 2013. URL: `https://cds.cern.ch/record/1505342`.

[132] T. G. Cornelissen et al. "Updates of the ATLAS Tracking Event Data Model (Release 13)". In: (June 2007).

[133] R. Fruhwirth. "Application of Kalman filtering to track and vertex fitting". In: *Nucl. Instrum. Meth. A* 262 (1987), pp. 444–450.

[134] M. Aaboud et al. "Performance of the ATLAS Track Reconstruction Algorithms in Dense Environments in LHC Run 2". In: *Eur. Phys. J. C* 77.10 (2017), p. 673. arXiv: `1704.07983 [hep-ex]`.

[135] Pierfrancesco Butti. *Tracking performance and prospects in ATLAS and CMS*. 2019. URL: `https://indico.cern.ch/event/687651/contributions/3427658/attachments/1850717/3038436/LHCP_TrackingTalk_v6.pdf`.

[136] Morad Aaboud et al. "Electron reconstruction and identification in the ATLAS experiment using the 2015 and 2016 LHC proton-proton collision data at $\sqrt{s} = 13$ TeV". In: *Eur. Phys. J. C* 79.8 (2019), p. 639. arXiv: `1902.04655 [physics.ins-det]`.

[137] Georges Aad et al. "Electron and photon performance measurements with the ATLAS detector using the 2015–2017 LHC proton-proton collision data". In: *JINST* 14.12 (2019), P12006. arXiv: 1908.00005 [hep-ex].

[138] Georges Aad et al. "Muon reconstruction and identification efficiency in ATLAS using the full Run 2 pp collision data set at $\sqrt{s} = 13$ TeV". In: *Eur. Phys. J. C* 81.7 (2021), p. 578. arXiv: 2012.00578 [hep-ex].

[139] Morad Aaboud et al. "Jet reconstruction and performance using particle flow with the ATLAS Detector". In: *Eur. Phys. J. C* 77.7 (2017), p. 466. arXiv: 1703.10485 [hep-ex].

[140] Georges Aad et al. "Jet energy scale and resolution measured in proton–proton collisions at $\sqrt{s} = 13$ TeV with the ATLAS detector". In: *Eur. Phys. J. C* 81.8 (2021), p. 689. arXiv: 2007.02645 [hep-ex].

[141] Georges Aad et al. "Topological cell clustering in the ATLAS calorimeters and its performance in LHC Run 1". In: *Eur. Phys. J. C* 77 (2017), p. 490. arXiv: 1603.02934 [hep-ex].

[142] Georges Aad et al. "Improving topological cluster reconstruction using calorimeter cell timing in ATLAS". In: *Eur. Phys. J. C* 84.5 (2024), p. 455. arXiv: 2310.16497 [physics.ins-det].

[143] Matteo Cacciari, Gavin P. Salam, and Gregory Soyez. "The anti-kt jet clustering algorithm". In: *Journal of High Energy Physics* 2008.04 (Apr. 2008), p. 063. URL: https://dx.doi.org/10.1088/1126-6708/2008/04/063.

[144] Stephen D. Ellis and Davison E. Soper. "Successive combination jet algorithm for hadron collisions". In: *Phys. Rev. D* 48 (7 Oct. 1993), pp. 3160–3166. URL: https://link.aps.org/doi/10.1103/PhysRevD.48.3160.

[145] "Tagging and suppression of pileup jets". In: (May 2014).

[146] "Pile-up subtraction and suppression for jets in ATLAS". In: (Aug. 2013).

[147] Morad Aaboud et al. "Identification and rejection of pile-up jets at high pseudorapidity with the ATLAS detector". In: *Eur. Phys. J. C* 77.9 (2017). [Erratum: Eur.Phys.J.C 77, 712 (2017)], p. 580. arXiv: 1705.02211 [hep-ex].

[148] Georges Aad et al. "ATLAS flavour-tagging algorithms for the LHC Run 2 pp collision dataset". In: *Eur. Phys. J. C* 83.7 (2023), p. 681. arXiv: 2211.16345 [physics.data-an].

[149] "Optimisation and performance studies of the ATLAS b-tagging algorithms for the 2017-18 LHC run". In: (July 2017).

[150] "Identification of Jets Containing b-Hadrons with Recurrent Neural Networks at the ATLAS Experiment". In: (Mar. 2017).

[151] "Secondary vertex finding for jet flavour identification with the ATLAS detector". In: (June 2017).

[152] "Topological b-hadron decay reconstruction and identification of b-jets with the JetFitter package in the ATLAS experiment at the LHC". In: (2018).

[153] Georges Aad et al. "ATLAS b-jet identification performance and efficiency measurement with $t\bar{t}$ events in pp collisions at $\sqrt{s} = 13$ TeV". In: *Eur. Phys. J. C* 79.11 (2019), p. 970. arXiv: 1907.05120 [hep-ex].

[154] Georges Aad et al. "Fast b-tagging at the high-level trigger of the ATLAS experiment in LHC Run 3". In: *JINST* 18.11 (2023), P11006. arXiv: 2306.09738 [hep-ex].

[155] Morad Aaboud et al. "Performance of missing transverse momentum reconstruction with the ATLAS detector using proton-proton collisions at $\sqrt{s} = 13$ TeV". In: *Eur. Phys. J. C* 78.11 (2018), p. 903. arXiv: 1802.08168 [hep-ex].

[156] "$E_{\mathrm{T}}^{\mathrm{miss}}$ performance in the ATLAS detector using 2015-2016 LHC *pp* collisions". In: (June 2018).

[157] Christopher G. Lester and Benjamin Nachman. "Bisection-based asymmetric M_{T2} computation: a higher precision calculator than existing symmetric methods". In: *JHEP* 03 (2015), p. 100. arXiv: 1411.4312 [hep-ph].

[158] M. Baak et al. "HistFitter software framework for statistical data analysis". In: *Eur. Phys. J. C* 75 (2015), p. 153. arXiv: 1410.1280 [hep-ex].

[159] Stefan Schmitt. "Data Unfolding Methods in High Energy Physics". In: *EPJ Web Conf.* 137 (2017). Ed. by Y. Foka, N. Brambilla, and V. Kovalenko, p. 11008. arXiv: 1611.01927 [physics.data-an].

[160] A. N. Tikhonov et al. "Regularization methods". In: *Numerical Methods for the Solution of Ill-Posed Problems.* Dordrecht: Springer Netherlands, 1995, pp. 7–63. URL: https://doi.org/10.1007/978-94-015-8480-7_2.

[161] G. D'Agostini. "A Multidimensional unfolding method based on Bayes' theorem". In: *Nucl. Instrum. Meth. A* 362 (1995), pp. 487–498.

[162] Bogdan Malaescu. "An Iterative, dynamically stabilized method of data unfolding". In: (July 2009). arXiv: 0907.3791 [physics.data-an].

[163] Adam Bozson, Glen Cowan, and Francesco Spanò. "Unfolding with Gaussian Processes". In: (Nov. 2018). arXiv: 1811.01242 [physics.data-an].

[164] ATLAS Jet/ETmiss. *Small-R (R=0.4) jet energy scale and jet energy resolution uncertainties for full run 2 analyses (release 21).* 2023. URL: https://twiki.cern.ch/twiki/bin/view/AtlasProtected/JetUncertaintiesRel21Summer2018SmallR (visited on 08/07/2023).

[165] ATLAS Collaboration. "Jet energy scale and resolution measured in proton–proton collisions at $\sqrt{s} = 13$ TeV with the ATLAS detector". In: *Eur. Phys. J. C* 81 (2020), p. 689. arXiv: 2007.02645 [hep-ex].

[166] ATLAS Flavour Tagging. *Tagger Calibration Recommendations for Release 21.* 2023. URL: https://twiki.cern.ch/twiki/bin/view/AtlasProtected/BTagCalibrationRecommendationsRelease21 (visited on 08/07/2023).

[167] ATLAS Collaboration. *E_T^{miss} performance in the ATLAS detector using 2015–2016 LHC pp collisions.* ATLAS-CONF-2018-023. 2018. URL: https://cds.cern.ch/record/2625233.

[168] ATLAS Collaboration. "Luminosity determination in pp collisions at $\sqrt{s} = 13$ TeV using the ATLAS detector at the LHC". In: (2022). arXiv: `2212.09379 [hep-ex]`.

[169] G. Avoni et al. "The new LUCID-2 detector for luminosity measurement and monitoring in ATLAS". In: *JINST* 13.07 (2018), P07017.

[170] ATLAS Collaboration. *Studies on top-quark Monte Carlo modelling with Sherpa and MG5_ aMC@NLO*. ATL-PHYS-PUB-2017-007. 2017. URL: `https://cds.cern.ch/record/2261938`.

[171] "Studies on top-quark Monte Carlo modelling for Top2016". In: (Oct. 2016).

[172] "Studies on the improvement of the matching uncertainty definition in top-quark processes simulated with Powheg+Pythia 8". In: (2023).

[173] ATLAS Collaboration. "Measurement of the top quark mass in the $t\bar{t} \rightarrow$ lepton+jets channel from $\sqrt{s} = 8$ TeV ATLAS data and combination with previous results". In: *Eur. Phys. J. C* 79 (2019), p. 290. arXiv: `1810.01772 [hep-ex]`.

[174] Jon Butterworth et al. "PDF4LHC recommendations for LHC Run II". In: *J. Phys. G* 43 (2016), p. 023001. arXiv: `1510.03865 [hep-ph]`.

[175] Andy Buckley et al. "LHAPDF6: parton density access in the LHC precision era". In: *Eur. Phys. J. C* 75 (2015), p. 132. arXiv: `1412.7420 [hep-ph]`.

[176] Georges Aad et al. "Measurement of the $t\bar{t}$ production cross-section and lepton differential distributions in $e\mu$ dilepton events from pp collisions at $\sqrt{s} = 13$ TeV with the ATLAS detector". In: *Eur. Phys. J. C* 80.6 (2020), p. 528. arXiv: `1910.08819 [hep-ex]`.

[177] Georges Aad et al. "Measurements of top-quark pair differential and double-differential cross-sections in the ℓ+jets channel with pp collisions at $\sqrt{s} = 13$ TeV using the ATLAS detector". In: *Eur. Phys. J. C* 79.12 (2019). [Erratum: Eur.Phys.J.C 80, 1092 (2020)], p. 1028. arXiv: `1908.07305 [hep-ex]`.